DEVELOPMENT OF OLEOPHOBIC POLYMERIC SURFACE INDUCED BY ION BEAMS

By

RISHI DEWAN

Under the Guidance of

DR. PARAG DIWAN

(Vice Chancellor, University of Petroleum & Energy Studies)

&

DR. RAJEEV GUPTA

(Assistant Professor, Department of Physics)

COLLEGE OF ENGINEERING STUDIES

Submitted

IN PARTIAL FULFILLMENT OF THE REQUIREMENT OF DEGREE

OF

DOCTOR OF PHILOSPHY

In

PHYSICS

To

UNIVERSITY OF PETROLEUM AND ENERGY STUDIES,

DEHRADUN

December, 2011

Dedicated

To

My Parents

ACKNOWLEDGEMENT

I would like to gratefully acknowledge to my guide **Dr. Parag Diwan**, Vice-Chancellor, University of Petroleum & Energy Studies, Dehradun for his encouragement, guidance, support, courage and motivation throughout my research work. His appreciation at the stage of my experimental work gave me boost and patience to carry out my research tirelessly.

I express my deep sense of gratitude to the **Dr. S.J. Chopra**, Chancellor, University of Petroleum & energy studies, Dehradun. I shall always remain indebted to him for his excellent guidance in this study.

My special thanks to **Ms. Deepa Verma**, Director-HR & IR, University of Petroleum and Energy Studies for her tremendous support, courage and help at each and every step of my work

I wish to take this opportunity to express my sincere thanks and regards to my co-guide **Dr. Rajeev Gupta,** Assistant Professor, College of Engineering, University of Petroleum & Energy Studies, Dehradun. His wide knowledge and logical way of thinking is extremely valuable for me. His constant encouragement and personal guidance provides an excellent support to me in completion my work.

My Special thanks to **Professor (Dr.) D. N. Saraf**, University of Petroleum and Energy Studies and **Dr. Ambuj Tripathi**, Scientist 'F' at Inter University Accelerator Centre (IUAC), New Delhi for their valuable suggestions, comments and guidelines to increase the gravity of my work.

I am highly grateful to my Dean, **Dr Shrihari**, Associate Dean **Dr S. K Banerjee** and H.O.D **Dr. Piyush Kuchhal** for their constructive comments and suggestions throughout this work.

I wish to thank **Dr.Vikram Sahay**, H.O.D., Deptt. of Communication and his entire team for going through the literatures and guiding me in report writing.

My Special gratitude to **Dr. Kamal Bansal, Dr. Mukesh Sexana, Dr. R K Badoni, Dr. Rajnesh Garg** for giving his guidance in final stage of my preparation. I wish to thank **Dr. K. K. Pandey**, **Dr. Bhawna Lamba,**

Dr. Amit Chawla Dr. R. K. Tripathi, Dr. K. S. R. Murthi for helping me in recording the observations at the time of experiments. My special thanks to **Ms. Snigdha Bora** & **Mr Shishir Varshney** for their support for making my thesis grammatically sound.

During this work i have collaborated with many colleagues for whom I have great regard. I wish to extend my warmest thanks to all those who have helped me directly or indirectly.

I am grateful to my parents for their continuous encouragement. They are the source of inspiration for me not only at the stage of my Ph.D. work but throughout my academic career.

In the last but not the least my thanks to my wife and my kids for their support without which i am unable to complete my work

Rishi Dewan

DECLARATION

I hereby declare that this submission is my own work and that, to the best of my knowledge and belief, it contains no material previously published or written by another person nor material which has been accepted for the award of any other degree or diploma of the university or other institute of higher learning, except where due acknowledgment has been made in the text.

Date: Dec., 2011 **(Rishi Dewan)**

CERTIFICATE

This is to certify that the thesis entitled "**Development of Oleophobic Polymeric Surface Induced by Ion Beams**" submitted by **Rishi Dewan** to University of Petroleum & Energy Studies, Dehradun for the award of the Degree of Doctor of Philosophy is a bonafide record of the research work carried out by him under my supervision and guidance. The content of the thesis, in full or parts have not been submitted to any other Institute or University for the award of any other degree or diploma.

(Dr. Parag Diwan)

Date: Dec. '11 **(Dr Rajeev Gupta)**

Place: UPES, Dehradun

EXECUTIVE SUMMARY

Numerous engineering applications require surfaces with low adhesion and stiction. Adhesion and stiction of oil on the solid surface is consider to be one of the critical problem in many engineering and industrial application. These problems can be minimized by oleo-phobic polymeric surface which requires high contact angle, low surface energy, low contact area and high surface roughness. It has been suggested that extremely oil repellent surfaces produced by creating micro/nano ordered roughness may satisfy the need for the non-adhesive surfaces. Highly ordered roughness is inversely proportional to the wettability of liquid on solid surfaces.

In this regard limited work has been done and it has been reported that the coated surface shows oleophobic property. Heish *et al.* developed a oil repellent silica coated polymeric surface developed and investigate the roll off behavior. Lee *et al.* studied the motion of the oil drop on fluorosilane grafted nylon film which is oleophobic surfaces. He also designed superoleophobic Nylon cotton fabric lyophobic surfaces with alteration of chemical composition and Hsieh *et al.* improved oil repellency on wood substrates by using fluorinated silica nanocoating. Narayan Prabhu studied the effect of surface roughness on wetting behavior of oils. The surface roughness degrades with the time in chemically generated polymeric surfaces which decrease the oleophobicity.

The surface modification i.e. increase in surface roughness of polymers has received much attention recently. In recent years, therefore, there has been much interest in developing surface treatment technologies to alter the chemical and physical properties of different polymeric surfaces to make these more useful. Different methods such as γ-ray, electron beam, plasma, UV and chemical initiator can be applied to modify the surfaces. Among all the methods of modifications, chemical graft copolymerization is one of the promising methods. In principle, graft copolymerization is an attractive method to impart a variety of functional groups to a polymer. Grafting

reaction involves the copolymerization of a monomer onto polymer backbone. This grafting will be more beneficial if we irradiate grafted co-polymer with low energy ion beam which will enhance the surface roughness with greater stability.

Ion beam is a unique tool to generate roughness on polymeric surfaces in a controlled manner by selection of specific ion species and energy and this makes it an attractive tool for many industrial applications. The low energy ion beam interaction with the grafted co-polymer produced chemically active sites which may play a vital role in the modification of the surface chemistry of the polymers. The interaction of grafted surface with ion beam increases the surface roughness with greater stability because of energy transfer to the surface. The degree of roughness or imperfection may also increase with increase in ion beam interaction time.

We opted two fold methodologies to increase the micro order roughness in our thesis work. First is grafting of suitable monomer on polymeric surface under different reaction conditions and second is low energy ion beam interaction with grafted co-polymer to enhance the order of surface roughness. For this purpose commercially available polytetrafluoroethylene (PTFE/Teflon) films of thickness 150μm was obtained. The PTFE film was sliced into square strips of about 2cm x 2cm in size. To remove the organic residue on the surface, the PTFE film was washed, dried and stored in clean and dry box. Benzoyl peroxide (BPO) and acetone have been used in this work to create active site for grafting Methyl Methacrylate (MMA).

The temperature of grafting medium is one of the most important reaction parameters that have a strong effect on the grafting yield. This experiment was performed at different temperatures 40, 50, 60 and 70 °C with an accuracy of ± 2°C for two hours with monomer concentration 10% and initiator 0.03M (optimized time as per reported in literature). After the grafting reaction, the samples were taken out from the monomer solution and washed with acetone to remove the remaining co-polymer. The washed samples were again weighed to know about any changes in weight due to grafting process.

The increase in temperature of grafting mixture up to 50°C initially increases the degree of grafting. This may be due to the increase of the initiation and propagation rates of graft copolymerization. Increase in the degree of grafting with increasing temperature is also due to increase in the decomposition of the initiator leading to the formation of more free radicals and generation of active sites on the polymeric backbone. But beyond 50°C, grafting rate decreased and the film became brittle. This is because at higher temperature, higher combination rates of monomer are obtained increasing homo polymerization reactions, which results in a decreased grafting rate. Maximum grafting was obtained at 50^{o}C, with very little grafting at 40^{o}C and also at 60^{o}C and 70^{o}C.

The change in morphology of PTFE surface after modification by grafting with MMA was studied by FE-SEM.

The result suggested that the surface initiated free radical polymerization has given rise to non-uniform molecular weight distribution and dense coverage of MMA on PTFE surface. The bumps in the form of white patches appear in FE-SEM image of grafted PTFE at 50°C. The height at this section of image is not similar to ungrafted surface. This white spot section in grafted image is nearly one third of the total surface area clearly indicates the increase in roughness of the surface. In similar fashion, deep dugs in the form of dark black spots also appear in images. Points represent duggy spots which are little dark in colour showing non-uniform structure of surface and hence depict increase in surface roughness. The non-uniformity in image is reduced at higher temperatures showing reduction in percentage of white patches. This was because of grafting rate reduction at higher temperature change in morphology of surface. At 50°C maximum % of grafting i.e 9.77% was achieved resulting in maximum change in surface morphology of PTFE polymer. The XRD analysis of grafted polymer at various temperatures indicate maximum crystallographic changes at 50°C grafted temperature. Contact angle goniometry concludes that contact angle is a function of percentage grafting. The value of the contact angle increased from 40°C to 50°C and its maximum value i.e 95.5°C exists when PTFE is grafted at 50°C.

After and before of this grafted temperature50°C the value of contact angle decreases and minimum value exist at the 70°C.

Pristine PTFE and grafted polymer samples were exposed to Ar^+ ion beam for 10 and 100 seconds respectively. The irradiated samples were stored in air tight box for safety purpose. In order to know the effect of ion beam on polymer surface and changes in surface chemistry, we characterized the irradiated polymer using FESE, EDS, XRD and contact angle goniometer.

To make comparative analysis and to study optimum roughness condition, two sets of irradiated samples of PTFE were studied. (i) irradiated with beam time of 10 sec (ii)irradiated with beam time of 100 sec. For each category three sets when grafted at 50, 60, 70°C were examined.

The contrast in an SEM image reveals information about the surface morphology and composition of the material. SEM observation showed that the surface of pristine PTFE has low but uniform roughness without sharp edges. The surface is more or less uniform and smooth. Few dark spots at some portions of surface indicate little irregularity in the height of sample surface.

FE-SEM observation of PTFE samples irradiated for 10 sec and grafted at 50°C showed mild bumps with shallow irregularities on the surface. The peak to valley height did not exceed approximately 0.5mm. Approximately equal portion of dark and light spots are present, indicating in surface roughness due to irradiation. Slight crack was also seen at one portion of the image

Approximately similar observations were made in second set of samples irradiated for 100s. Dark and mild spots were almost equal indicating of maximum roughness for sampled grafted at 50°C. Samples grafted at 60°C and 70°C showed cracks which were also present when irradiated for 10 sec.

There was no change in the composition of the elements as found via EDS analysis. This clearly shows that the ion beam which we have used to increase the oleophobicity of the grafted Teflon has only imparted the energy to

decrease the smoothness of the sample. The ions did not got embedded in the sample.

The contact angle is a direct measure of wettability whereas surface roughness is only indicative of change in wettability. Contact angles of pristine, grafted and irradiated samples were measured using CH_3I as oil phase liquid with contact angle goniometer. Grafted polymer treatment was performed with ISE 10 Ion Gun using 3 KeV Ar+ ions and a defocused ion beam.

Monomer grafted PTFE samples showed slight increase in contact angle. However, after irradiated further increase of 8 to 10^o was observed. This definite change in contact angle corroborated well with increase in surface roughness as seen in FE-SEM images.

Ion beam irradiation enhances surface roughness at micro-scale leading to change in surface wetting has been established in this work. Further extensive studies are needed to increase this change to produce truly super oleophobic surfaces for engineering applications.

CONTENTS

LIST OF SYMBOLS

%	Percent
Υ	Free Surface Energy
W	The Work of Cohesion
R_r	Non-Dimensional Surface Roughness Factor
θ_H	Contact Angle Hysteresis
H	Polymer
M	Monomer
$\sigma(E)$	Differential Scattering Cross-section
E	Energy
$\phi(r/a)$	Screening Function
V_0	Bohr Velocity of An Electron
a_o	Bohr's Radius
R_P^P	Mean Projected Range
KeV	Kilo Electron Volt
ω_p	Plasma Frequency
β	Bond Number or Shape Factor

LIST OF ABBREVIATIONS

EURATOM	The European Atomic Energy Community
LET	Linear Energy Transfer
PTFE	Polytetrafluoroethylene
FE-SEM	Field Emission- Scanning Electron Microscopy
XRD	X-Ray Diffraction
EDS	Energy-Dispersive X-Ray Spectroscopy
CAG	Contact Angle Goniometry
BPO	Benzoylperoxide
MMA	Methyl methacrylate
T-Flask	Three Neck Flask
ECR	Electron Cyclotron Resonance
FET	Field Effect Transistor
IBAD	Ion Beam Assisted Deposition

LIST OF FIGURES

LIST OF TABLES

Chapter 1

INTRODUCTION

1.1 INTRODUCTION

The polymeric surfaces with non-adhesiveness and less stiction are required for proper functioning in most of the industrial application. It was suggested that extremely repellent surfaces produced by applying a micro/nano patterned roughness may satisfy the need for non-adhesive surfaces. The term oleo-phobic is applied if we consider in context of oil repelling surfaces. Roughness induced olephobicity has been suggested as a way to reduce the wettability of oil on surfaces. The surface energy has been found a useful concept for interpreting adhesion, spreading and wetting behavior of oil on surfaces. The primary parameter that characterizes poor wetting is the high static contact angle, high surface roughness, low surface energy and low contact angle hysteresis.

Fluorocarbon polymers are suitable polymers for these applications due to their unique properties, such as high thermal stability, excellent chemical resistance, low friction coefficient, superior weatherability, oil repellence, low flammability, low dielectric constant, chemical inertness and a low coefficient of friction and stiction etc.[1-4]. In this context, poly-tetrafluoroethylene (PTFE) is considered to be the "benchmark" low surface energy material in fluoro carbon polymer group.

1.2 PREVIOUS LITERATURE

Oleophobic surfaces have not been studied as extensively as hydrophobic surfaces. Heish *et al.* [5] developed an oil repellent, silica coated, polymeric

surface and investigated the roll-off behavior of oil droplet. Lee *et al* [6] studied the motion of the oil drops on fluorosilane grafted nylon film which is an oleophobic surface. These workers also designed superoleophobic nylon - cotton fabric with alteration of chemical composition [7] and Hsieh et al [8] improved oil repellency on wood substrates by using fluorinated silica nanocoating. Prabhu *et al* [9] studied the effect of surface roughness on wetting behavior of oils. However, the work was limited on to the degradation of stability of oleophobic surface with time.

Tuteja *et al.* [10] develop design parameters that enable the evaluation of the robustness of the composite interface on a oleophobic surface. Based on these design parameters, they also rank various superoleophobic substrates discussed in the literature, with particular emphasis on surfaces developed from inherently oleophilic materials. Hoefnagels *et al.* (2007) [11] explains when a perfluoroalkyl chain is introduced to the silica particle surface, the textile becomes highly oleophobic, as demonstrated by a static contact angle greater than 110° and a roll-off angle of 24° for a 15 µl sunflower oil droplet.

Bigelow *et al.* [12] **explain the development of** oleophobic monolayers. His observations were made to determine the smallest concentrations of various types of oleophobic compounds which would permit the formation of oleophobic monolayers on platinum.

Jung *et al.* (2009) [13] studied the oleophobic surfaces that have the potential for self-cleaning and antifouling from biological and organic contaminants in both air and water. The surface tension of oil and organic liquids is lower than that of water, so to create a oleophobic surface, the surface energy of the solid surface in air should be lower than that of oil. The wetting behavior of oil droplets for oleophobic/philic surfaces in three-phase interfaces was studied. In order to make the surface oleophobic at a solid−air−oil interface, a material with a surface energy lower than that of oil was used. In underwater applications, the oleophobicity/philicity of an oil droplet in water was studied on the surfaces with different surface energies of various interfaces and contact angles of water and oil droplets in air. A model for predicting the contact angles of water and oil droplets was proposed. To validate the model,

the wetting behavior of flat and micropatterned surfaces with varying pitch values were studied.

Liu *et al.* [14] design oleophobic surfaces which requires an understanding of the effect of the geometrical shape of etched silicon surfaces on the contact angle and hysteresis observed when different liquids are brought into contact with oleophobic surfaces. This study used liquid-based metal-assisted etching and various silane treatments to create superoleophobic surfaces on a Si surface. Etch conditions such as the etch time and etch solution concentration played critical roles in establishing the oleophobicity of Si When compared to Young's contact angle, the apparent contact angle showed a transition from a Cassie to a Wenzel state for low-surface-energy liquids as different silane treatments were applied to the silicon surface. These results demonstrated the relationship between the re-entrant angle of etched surface structures and the contact angle transition between Cassie and Wenzel behavior on etched Si(111) surfaces.

Segal *et al.* [15] shows the application of some fluorochemicals to cotton textiles to impart oleophobic surface characteristics to the materials has been investigated further. The chromium complexes of perfluoromonocarboxylic acids were used in conjunction with acrylic emulsion. These were employed in separate operations as well as combined with the complexes into one emulsion.

Torchinsky *et al.* [16] explain the wettability modification of materials by low-energy electron flux. In this work, they define the method that they developed for electron-induced surface energy and modification. The applied technique has afforded gradual tuning of the surface free energy, resulting in a wide range of wettability modulation.

Cao *et al.* [17] report a facile process for fabrication of highly oleophobic surfaces through assemble of silica nanoparticle. The layer by layer assembly techniques is used in this process. Lee *et al.* [18] Develop a oleophobic material by two criteria: low surface energy and properly designed surface morphology. The relationships among surface tensions, contact angles, contact angle hysteresis, roll-off angles, and surface morphologies of such materials

are studied. Numerical formulae related to the surface energy of liquids and solids are used to predict the wetting behavior of oleophobic materials. Using chemical and geometrical modifications, a oleophobic surface was prepared. Good agreement between the predicted and measured contact angles and roll-off angles were obtained. The effect of the contact angle hysteresis on the roll-off angle is described to understand the motion of a droplet when the droplet begins to roll off.

Ohkubo *et al.* [19] develop a novel method for preparing and characterizing oleophobic surface. Aluminum (Al) substrate was roughened by sandblasting and electrolytic etching to obtain micro- and nano-sized complex morphologies. Then, its substrate was covered by a chemically adsorbed monolayer containing a fluorocarbon group. The surface of the wettability was characterized by contact angle measurements and its surface indicated the oil contact angle (OCA) of hexadecane was nearly 110°. The wettability was also characterized by solid surface energy. The solid surface energy of solvent was obtained and the values were extremely low, ranging from 0.31 to 1.29 mN/m. Their values indicated that the oleophobicity of their sample reached the highest level possible.

1.3 SPECIFIC OBJECTIVES

a) Grafting of Poly-methylmethaacrylate (PMMA) on poly-tetra fluoroethylene (PTFE) at different temperatures.
b) Low energy ion beam interaction with grafted polymer.
c) Comparative study on effect of ion beam on pristine and grafted polymer.
d) Characterization of samples with Field Emission Scanning Electron Microscope(FE-SEM), Energy Dispersive Spectrum Analysis (EDSA), Contact Angle Goniometer (CAG) and X-Ray Diffraction (XRD).

1.4 RESEARCH METHODOLOGY

The surface modification of polymers has received much attention recently. In recent years, there has been much interest in developing surface treatment technologies to alter the chemical and physical properties of different polymeric surfaces to make them more useful. Different methods such as γ-

ray, electron beam, plasma, UV and chemical initiator can be applied to modify the surfaces. Among all the methods of modifications, chemical graft copolymerization is one of the promising methods. In principle, graft copolymerization is an attractive method to impart a variety of functional groups to a polymer. Grafting reaction involves the copolymerization of a monomer onto a polymer backbone.

Fig. 1.1 shows the flow diagram of the steps followed in this research work. PTFE film was characterized with respect to its surface property and was then grafted with MMA copolymer.

The grafted PTFE film was irradiated with low energy (3 KeV) Ar+ ion beam which was once again characterized. The data were than analyzed and conclusion drawn.

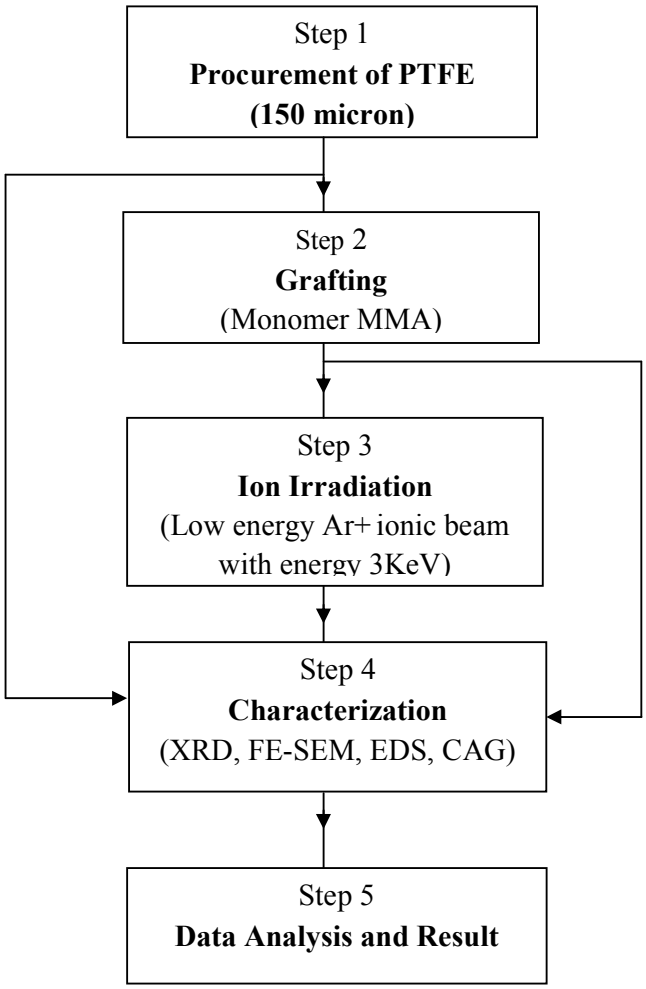

Fig. 1.1 : Research methodology

The thesis is organized in eight chapters which comprises the following:

Chapter 1 deals with the introduction of the problem, brief literature review and research methodology related to the work. The details of the others chapters is also given at the end.

Chapter 2 deals with the mathematical formulation required to characterize the wettability of solid surfaces to static contact angle and contact angle hysteresis.

In this chapter the effect of gravity, de-stabilization due to gravitation waves and limitations of Wenzel and Cassie equation are discussed. Naturally existing oleophobic surfaces and roughness induced oleophobic behavior have been analyzed.

Chapter 3 presents the detailed methodology to increase the surface roughness through chemical grafting process. Apart from that the effect of various parameters on grafting like monomer concentration, temperature and reaction time are discussed.

Chapter 4 gives an idea of source of energetic ions and ion beam irradiation. The idea of energy loss in polymer with range and damage distribution is discussed. The detailed mechanism of sputtering with impact of irradiation on on polymer is also discussed in this chapter.

In **Chapter 5**, details of the methodologies used for characterizing the polymer samples are presented. Characterization of polymer as well as treated polymer film by Field Emission-Scanning Electron Microscopy (FE-SEM), X-ray Diffraction (XRD), Energy-Dispersive X-ray Spectroscopy (EDS) and Contact Angle Goniometry (CAG) are described in details.

In **Chapter 6**, the detail of monomer grafting on polymer backbone are presented. The surface morphology of PTFE polymer was modified through grafting of MMA by chemical reaction. The effect of monomer, initiator, temperature and reaction time were studied and analysed. Surface modification before and after grafting as analysed through FE-SEM and

discussed. Crystallographic changes and elemental composition after grafting as measured through EDS and XRD are also included and contact angle goniometry is applied to measure the contact angle before and after grafting and/or irradiation.

In **Chapter 7**, the analysis about the change in surface morphology after the irradiation is presented. The comparative analysis of the images by FE-SEM before and after irradiation is discussed. The data pertaining to the contact angle measurement and their comparison with grafted PTFE surface is also a part of this chapter. The EDS analysis for elemental composition after the irradiation and XRD analysis for surface orientation and crystallinity are also discussed in this chapter.

In **Chapter 8**, the final conclusions drawn from the study are presented. Recommendations has been made for further research work in this area keeping in view, the potential practical application of this result in engineering and industry.

Chapter 2

FUNDAMENTAL AND BASIC PRINCIPLE OF OLEOPHOBICITY

2.1 INTRODUCTION

Numerous applications in various fields require surfaces with low adhesion and stiction. As the size decreases, surface forces tend to dominate over volume forces, and adhesion and stiction constitute a challenging problem for proper operation [20, 21]. This makes the development of non-adhesive surfaces crucial for many of emerging applications. It has been suggested that extremely oil-repellent (superoleophobic) surfaces produced by applying micro-patterned roughness may satisfy the need for the non adhesive surfaces.

The non-adhesiveness of any surface can be characterize by the contact angle. The value of contact angle is different for different surfaces i.e. homogeneous surfaces and heterogeneous surfaces. Young's successfully explained the wettability of liquid on homogeneous surface while Wenzel [22] and Cassie Baxter [23] explains heterogeneous surface.

2.2 CONTACT ANGLE ANALYSIS

The dependence of the contact angle on the surface tension is considered for a liquid in contact with smooth and a rough solid surface, forming a homogeneities interface. The surface atoms or molecules of liquids or solids have energy above that of similar atoms and molecules in the interior, which results in surface tension or free surface energy being an important surface property. This property is characterized quantitatively by the surface tension or free surface energy Υ, which is equal to work that is required to create a unit area of the surface at constant volume and temperature. The unit of Υ are J m^{-2} or N m^{-1} and can be interpreted either as energy per unit surface area or as tension force per unit length of a line at the surface. When a solid is in

contact with liquid, the molecular attraction will reduce the energy of the system below that for the two separated surfaces. This may be expressed by the Dupre equation:

- Eq. (2.1)

where W_{SL} is the work of cohesion per unit area between two surface, Υ_{SA} and Υ_{SL} are the surface energies (surface tensions) of the solid against air and liquid and $\Upsilon_{LA}$is the surface energy of liquid against air [24] .

The contact angle depends on several factors, such as roughness and the manner of surface preparation and its cleanliness. The term 'oleophobic/ philic' is used with regard to the wetting by oil. Surface with high energy, formed by polar molecules, tend to be oleophobic, whereas those with low energy and built of non-polar molecules tend to be oleophilic. If the oil wets the surface (referred to as a wetting liquid or a oleophilic surfaces), the liquid value of the static contact angle is $0^o \leq \theta \leq 90^o$, whereas if the liquid does not wet the surface (referred to as a non-wetting liquid or a oleophobic surface), the value of the contact angle is $90^o \leq \theta \leq 180^o$. The term oleophobic/philic, which was originally applied only oil (oleo means oil in Greek), is often used to describe the contact of a solid surface with any liquid.

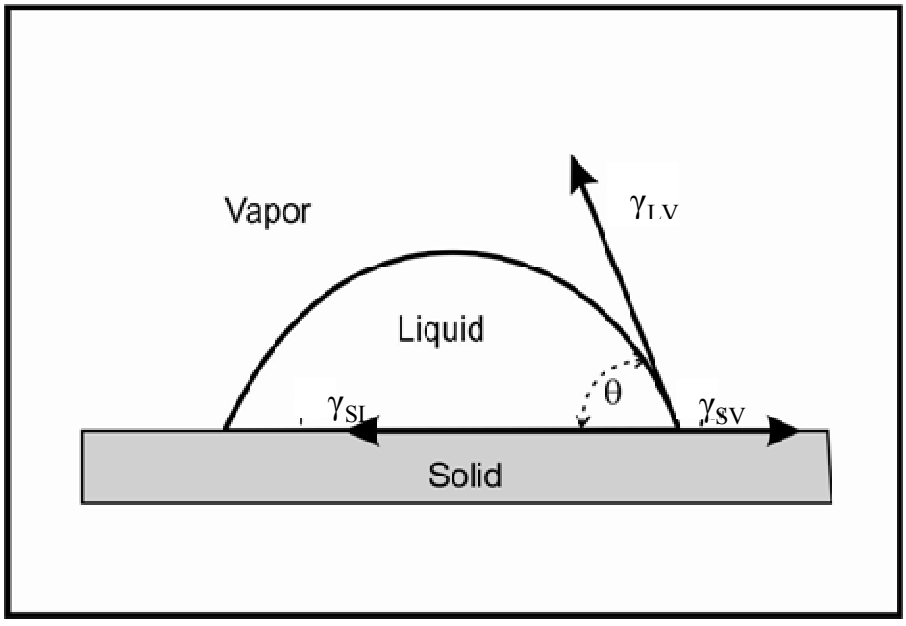

Fig. 2.1 Liquid drop on solid surface

Spreading constant $S = \gamma_{SV} - (\gamma_{SL} + \gamma_{LV}\cos\theta)$ decides that the surfaces are oleophobic or oleophilic. If S is positive i.e. $\gamma_{SV} > (\gamma_{SL} + \gamma_{LV}\cos\theta)$, then surface contact area will be greater and will show the low contact angle or greater wettability. On the other hand if S is negative i.e. $\gamma_{SV} < (\gamma_{SL} + \gamma_{LV}\cos\theta)$, then the contact angle should be high and show the poor wettability.

2.3 ROUGH SURFACES

Wetting in reality is more complex than described above. This is mainly due to the non-ideality of the surface, which can be both rough and chemically heterogeneous. While the latter can be accounted for by considering a locally different compound with different properties (and thus a different surface tension), the former cannot be corrected this easily. The earliest work on the effect of surface roughness on contact angles can be attributed to Wenzel and Cassie and Baxter . They provided different expressions for apparent contact angles, based on different average characteristics of a rough surface.

Wenzel state assumed the liquid completely fills up the grooves in on a rough surface (Fig. 2.2) and state that on a rough surface for an identically same increase in the free liquid area at the upper surface of the drop (i.e. the liquid-vapor-surface), a greater amount of actual surface is wetted under it than compared to a smooth area. Thus, the net energy decrease on wetting a water-repelling surface will be greater for the rougher surface than a smooth surface and thereby enhances its water-repellency. The same analogy goes for water attracting surfaces, thus making them more water attracting. Therefore, according to Wenzel, a distinction must be made between the total (or actual) surface and the superficial (or geometric) surface. This results in a "roughness factor" designated by r, the ratio between the actual surface and the geometric surface, by which the contact angle derived from Young's equation must be corrected.

We first consider a water droplet on a rough surface with a homogeneous interface. The interface area increases with respect to that for a smooth surface. Using the surface force balance and empirical considerations, relates the contact angle of a oil droplet upon a rough solid surface, θ, with that upon

a smooth surface, θ_0, Fig. 2.2, through the non-dimensional surface roughness factor, R_r, equal to the ratio of the surface area, A_{SL}, to its flat projected area, A_F i.e.

$$R_f = \frac{A_{SL}}{A_F}$$

$$\cos\theta_W = \frac{dA_{SL}}{dA_F}\frac{dA_{LA}}{dA_{SL}} = R_f \cos\theta y \qquad \text{Eqn. (2.2)}$$

The value of the R_f is equal to unity if the surface is perfectly smooth, while its value is >1 if the surface is rough. This is called Wenzel equation and the dependence of the contact angle on the roughness factor is presented in Fig. 2.2 for different values of θ_y.

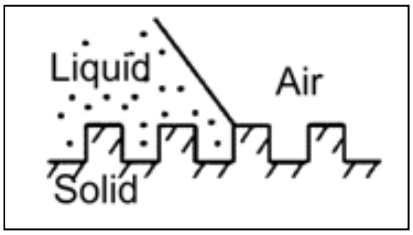

Fig. 2.2 : Wenzel's interface

The Wenzel equation predicts that wetting is enhanced by roughness, when θ is < 90°, and the wetting is lessened by roughness as shown in Fig. 2.3.

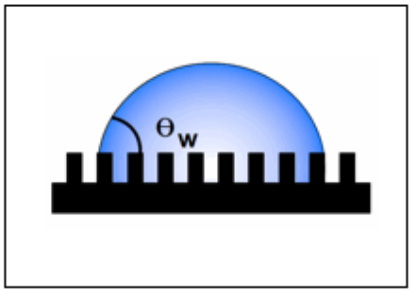

Fig. 2.3 : A drop of liquid in the Wenzel's state

Since $R_f > 1$, then Wenzel's angle is 180°, when $\cos\theta_y$ is $< -\frac{1}{R_f}$. Hence, according to Wenzel, the contact angle is 180° for all cases in which $\theta_y > \cos^{-1}\left(\frac{1}{R_f}\right)$. However, when θ > 90°, under some roughness condition, air

bubbles may be trapped in the rough grooves. In this case, the drop is actually situated on a composite surface, and the wetting behavior is described by Cassie and Baxter.

The Cassie-Baxter [23] state, also known as the composite or heterogeneous state, is a wetting state where, different from the Wenzel's state, it is considered that the grooves under the droplet are filled with vapor instead of liquid, as schematically shown in Fig. 2.4.

This state is first described by Cassie and Baxter. In this case, the liquid-surface interface is actually an interface consisting of two phases, namely a liquid-solid interface and a liquid-vapor interface. And the apparent contact angle is the sum of all the contributions of the different phases as described below:

$$\cos \theta_c = f_1 \cos \theta_1 + f_2 \cos \theta_2 \qquad \text{Eqn. (2.3)}$$

where θ_c is the apparent contact angle, f_1 and $2f$ are the surface fractions of phase 1 and phase 2, respectively; 01 and 02 are the contact angles on phase 1 and phase 2, respectively. This equation applies when there is no roughness. When one of these surfaces is the air-liquid interface, f is the solid fraction, defined as the fraction of the solid surface that is wetted by the liquid. Then the air fraction is $(1–f)$. With $\theta = 180^o$ for air, the resulting angle can be calculated by the following equation :

$$\cos \theta_c = R_f \cos \theta_y + (1 - R_f \cos 180^o) = f \cos \theta_y + f - 1 \qquad \text{Eqn.(2.4)}$$

The parameter f ranges from 0 to 1, where at $f = 0$ the droplet does not touch the surface at all and at $f = 1$ the surface is completely wetted, the same as the behavior of a flat surface. According to Cassie's formula, the apparent contact angle changes shrply at $\theta_y = 90^o$ ($\cos \theta_y = 0$). Furthermore, the apparent angle can only be 180^o if Young's angle is 180^o.

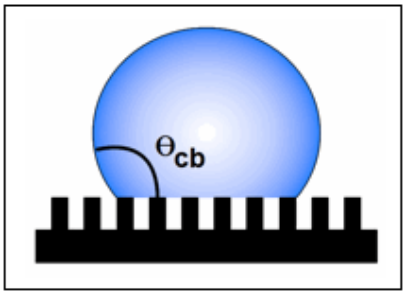

Fig. 2.4. : A drop of liquid in Cassie Baxter state.

When a droplet is in the Cassie state, the small contact area between the droplet and solid surface allows the droplet to roll easily over the surface. The Wenzel's and Cassie and Baxter states highly depends on surface roughness. If the order of roughness is low, then oil may completely penetrate into the roughness grooves and Wenzel's equation hold good. If the order of surface us very high then liquid does not fill the grooves on the rough surface and in this condition, Cassie state holds good.

2.4 CONTACT ANGLE HYSTERESIS

The contact angle we mentioned above is the static contact angle, which delines the energetically most favorable state of a droplet on a solid surface. However, different contact angles can coexist along the contact line due to either chemical heterogeneity, surface roughness. A small droplet of water can remain immobile on a tilted surface; the water contact angle at the back of the droplet is smaller than that at the front of the droplet, as shown in Fig. 2.5(a). The two different contact angles can also be observed when more water is added to and withdrawn from the droplet. When water is added into a water droplet, the contact angle will increase until the contact line starts to move forward; this contact angle is called advancing contact angle. On the other hand, when water is withdrawn from a water droplet, the contact angle will decrease until the contact line starts to recede; this contact angle is called receding contact angle (Fig. 2.5). The difference between advancing and receding contact angles is defined as the contact angle hysteresis. It is represented by θ_H.

$$\theta_H = \theta_A - \theta_R \qquad \text{Eqn.(2.5)}$$

The contact angle hysteresis is a measure for how well a drop of liquid sticks to the surface. It is therefore important that a oil repellent surface has a low contact angle hysteresis i.e. advancing and receding angle should be nearly equal.

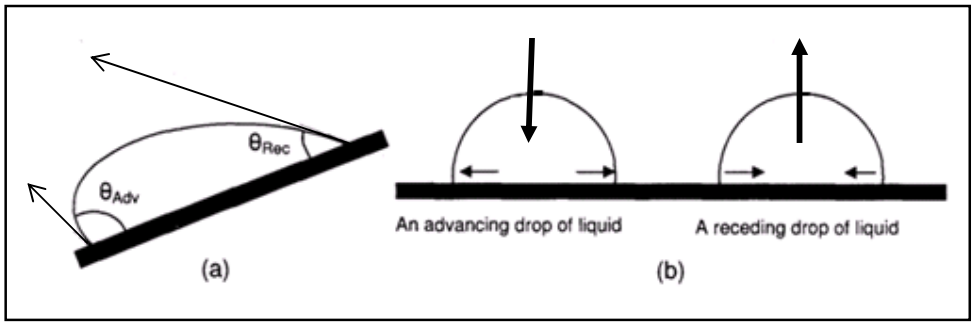

Fig.2.5 (a) Contact angle hysteresis on a titled surface, and (b) schematic illustration of advancing and receding contact angles on a flat surface via increasing and decreasing the volume of droplet, respectively.

Measurements on the hysteresis of the contact angle have been done by Johnson and Dettre [25]. Data reported on the advancing θ_a and the receding contact angle θ_r on surfaces of wax with variable roughness is shown in Fig. 2.6.

Of interest is the effect of the surface roughness on the hysteresis. As the roughness (here defined only qualitatively), increases, we first notice a large increase in hysteresis, although the variations of the angles themselves are relatively small. Then, as the roughness increases further the hysteresis newly vanishes due to the large increases in the contact angles. Thus, increasing surface roughness not only enhances the hydrophobicity of a hydrophobic surface, as predicted by the Wenzel-model and the Cassie-Baxter-model, but also has a large effect on the contact angle hysteresis.

It is very difficult to calculate the Vander Wall's forces in materials. A simpler approach is to calculate the value of free surface energy for the same. Free surface energy can be defined as the energy required to create a new surface express over an area consisting of many number of atoms in the surface lattice. Surface free energy is the function of material and it depends upon orientation of the surface.

The atoms at the surface have unused energy, so they can interact with each other, with other atoms from the bulk, and with species from the environment.

Free surface energy influences adhesive bonds for solids in contact and, hence, friction and wear.

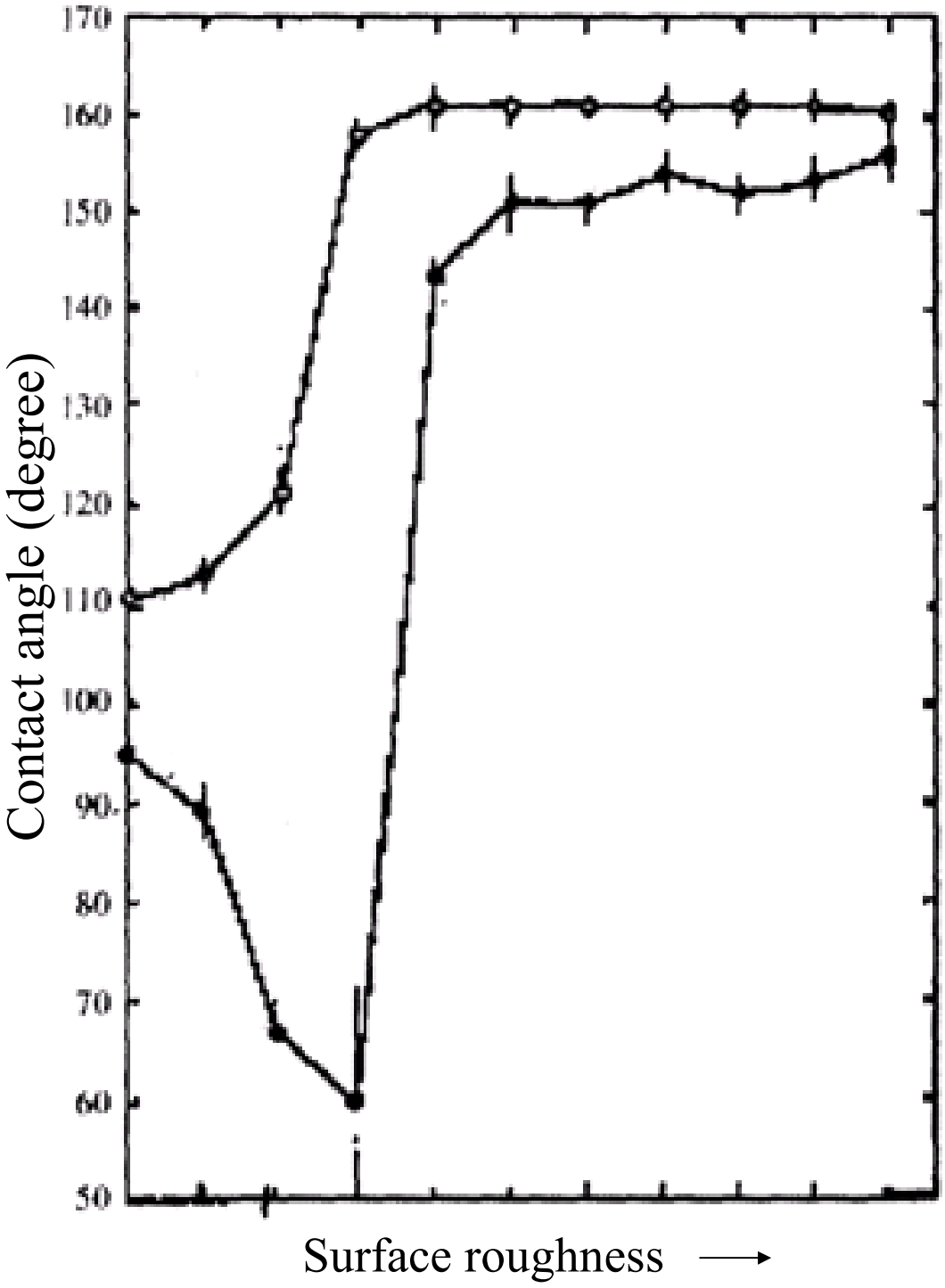

Fig.2.6 : Advancing (open symbols) and receding (closed symbols) contact angles of water on a wax surface as a function of the surface roughness.

In addition, it determines the nature of the interaction of lubricants with solids. When a bond is formed between two materials [having free surface energies per unit area in air $(\gamma_{SA})_1$ and $(\gamma_{SA})_2$ or simply γ_1 and γ_2] in contact, the surface energy of the interface per unit area changes to γ_{12}. Then the work of adhesion or the energy of adhesion per unit area is defined by Bardley [26] and Bailey [27] and given as:

$$W_{ad} = \Delta\gamma = \gamma_1 + \gamma_2 - \gamma_{12} \qquad \text{Eqn. (2.6)}$$

where $\Delta\gamma$ is equal to a reduction in the surface energy of the system per unit area (always negative), in mJ/m^2. Thus, $\Delta\gamma$ represents the energy that must be applied to separate a unit area of the interface or to create new surfaces. For two similar materials, $\Delta\gamma$ becomes the work of cohesion, and is equal to 2γ (γ_{12}=0). This important thermodynamic relation is valid for both solid and liquid interfaces. γ is generally called free surface energy for solids and surface tension for liquids [28].

The higher the surface energy of a solid surface, the stronger the bonds it will form with a mating material. One obvious suggestion from the surface energy theory of adhesion is to select materials that have a low surface energy and low $\Delta\gamma$. Use of lubricants at the interface reduces the surface energy. The surface energy of solid surfaces typically ranges from a few hundred to a few thousand mJ/m^2, whereas for most liquids it is few tens of mJ/m^2. Nonpolar lubricants have a lower surface energy than polar lubricants. Organic contaminants can also reduce the surface energy considerably.

2.5 STABILITY OF THE COMPOSITE INTERFACE

A homogeneous interface may be unstable, so that stability of the homogeneous interface should by determined. Mathematically, it means that in addition to satisfying the equilibrium condition for the net energy

$$dE = 0 \qquad \text{Eqn. (2.7)}$$

the stable configuration should satisfy the minimum net energy condition

$$d^2E > 0 \qquad \text{Eqn. (2.8)}$$

The interface may be destabilized due to small perturbations caused by various external influences and effects. Furthermore, the configuration may have many stable equilibrium condition (metastability and may be transformed from one stable position to another due to the external effects, with a certain probability of finding the system at a given state.

2.6 EFFECT OF GRAVITY

We ignored the effect of gravity by assuming that the gravity force is small compared to the surface tension forces. However, for big droplets this assumption may not be correct. If the weight of a droplet exceeds the vertical component of the total surface tension force at the triple line, a droplet, suspended at the tops of the asperities, will collapse [29]. Thus a maximum critical size of the droplet R_{max} exists, above which the droplet cannot remain suspended on the tops of the asperities. Let us investigate how this maximum size depends on the period of asperities/ consider a rough surface with roughness period l and amplitude z, which corresponds to maximum to its volume and to the third of R_{max}.

$$W \propto R_{max} \qquad \text{Eqn. (2.9)}$$

For the maximum value of droplet radius, the weight is equal to the total vertical component of the surface tension, proportional to the surface tension times the cosine of the contact angle times the total perimeter of the triple lines:

$$W \propto \gamma_{SL}\, t\, N \cos\theta \qquad \text{Eqn.(2.10)}$$

where N is the number of asperties under the droplet [30]. Consider another rough surface with period αl and amplitude $\alpha\hat{z}$, which has the same roughness factor and the same contact angle. The length of the triple line for each asperity will be αt. The number of asperities under the droplet is proportional to the second power of R_{max} divided by the second power of α

$$N \propto \left(\frac{R_{max}}{\alpha}\right) \qquad \text{Eqn.(2.11)}$$

Combining Eqns. (2.17) and (2.19) yields.

$$R_{max} \propto \frac{1}{\alpha} \qquad \text{Eqn. (2.12)}$$

This result suggested that with increasing asperity size the ability of a rough surface to form the composite interface decreases and larger droplets collapse. Therefore, smaller asperities makes composite interface more likely due to gravity. Increase the droplet size has a same effect as increasing the period of roughness.

2.7 LIMITATION OF THE WENZEL AND CASSIE EQUATIONS

Cassie equation is based on the assumption that the heterogeneous surface is composed of well-separated distinct patches of different material, so that the free surface energy can be averaged. It has been argued also that when the size of the chemical heterogeneities is very small (of atomic or molecular dimension), the quantity that should be averaged is not the energy but the dipole moment of a macromolecule [31] and is given as:

$$(1 + \cos\theta)^2 = f_1 (1 + \cos\theta_1)^2 + f_2 (1 + \cos\theta_2)^2 \qquad \text{Eqn.(2.13)}$$

Experimental studies of polymers with different functional groups showed a good agreement with Eqn.(2.13)

2.8 RANGE OF APPLICABILITY OF THE WENZEL AND CASSIE EQUATION

For a liquid front propagating along a rough tow-dimensional profile, the derivative of the free surface energy (per liquid front length), W. by the profile length, t, yield the surface tension force $\sigma = dW/dt = \Upsilon_{SL} - \Upsilon_{SV}$. The quantity of practical interest is the component of the tension force that corresponds to the advancing of the liquid from in the horizontal direction for dx. This component is given by $dW/dx = (dW/dt)(dt/dx) = (\Upsilon_{SL} - \Upsilon_{SV})\, dt/dx$. It is noted that the derivative $R_f = dt/dx$ is equal to Wenzel's roughness factor in the case when the roughness factor is constant throughout factor in the case when the roughness factor is constant throughout the surface. Therefore, the Young Eqn., which relates the contact angle with solid, liquid, and vapor interface tensions. $\Upsilon_{LV} \cos\theta = \Upsilon_{SV} - \Upsilon_{SL}$ is modified as

$$\Upsilon_{LV}\cos\theta = R_F (\Upsilon_{SV} - \Upsilon_{SL}) \qquad \text{Eqn. (2.14)}$$

The empirical Wenzel Eqn. is a consequence of Eqn. (2.14) combined with the young Eqn.

Nosonovsky [30] showed that for a more complicated case of a non-uniform roughness, given by the profile z(x), the local value of $r(x) = dt/dx = (1 + (dz/dx)^2)^{½}$ matters. In the general case of a 3D rough surface z(x,y), the roughness factor can be defined as a function of the coordinates $r(x, y) = (1 + (dz/dx)^2 + (dz/dy)^2)^{½}$.

2.9 NATURAL OLEOPHOBIC, SELF-CLEANING, AND DRAG REDUCTION SURFACES

A model surface for oleophobicity and self-cleaning is provided by fish which are known to be well protected from contamination by oil pollution although they are wetted by water [32]. Fish scales have a hierarchical structure consisting of sector-like scales with diameters of 4-5 mm covered by papillae 100-300 μm in length and 30-40 μm in width [33]. These grooved scales reduce vortices formation present on a smooth surface, resulting in water moving efficiently over their surface [34]. The water surrounding these complex structures can lead to protection from marine fouling and play a role in the defense against adhesion and growth of marine organisms, e.g., bacteria and algae [35]. If oil is present on the surfaces in air or water, surfaces are known to be oleophobic and may provide self-cleaning and anti-fouling. The many sea animals including fish and shark are known to be oleophobic under water. Superoleophobic surfaces cart also reduce significant losses of residual fuel in fuel tanks and pipes.

2.10 ROUGHNESS INDUCED OLEOPHOBICITY

The surface-tension of oil and organic liquids is lower than that of water, so to create a superoleophobic surface, the surface energy of the solid surface in air should be lower than that of oil. For underwater applications, if an oil droplet is placed on a solid surface in water, the solid-water-oil interface exists. The nature of oleophobicity/philicity of an oil droplet in water can be determined

from the values of surface energies of various interfaces and contact angles of water and oil in air.

Many superoleophobic surfaces have been developed by modifying the surface chemistry with a coating of extreme low surface energy materials [36, 37]. The surface curvature, in conjunction with chemical composition and roughened texture, can be used for liquid with low surface tension, including alkanes such as decane and octane. Liu *et al*. [33] performed experiments in a solid-water-oil interface. They found that hydrophilic and oleophilic surfaces (solid-air-water interface and solid-air-oil interface) can switch to an oleophobic surface in water (solid-water-oil interface). As a result, oil contaminants are washed away when immersed in water. This effect can be employed for underwater oleophobicity and self-cleaning that can be used against marine ship fouling for predicting the oleophobic/philc nature of surfaces and showed how the water and oil droplets in three phase interfaces influence the wetting behavior on micro-patterned surfaces with varying pitch values as well as the shark skin replica as an example of aquatic animal.

CHAPTER 3

POLYMER AND ITS GRAFTING

3.1 INTRODUCTION

Polymer is widely accepted in many industrial applications and its utility may be increased by modifying the requisite properties. Several methods are in practice to modify the properties of the polymer by changing its surface chemistry. One trend in modern civilization is to effect gradual replacement of natural materials with either all synthetic materials or modified natural materials. In the polymeric age, it is essential to modify the properties of a polymer according to tailor-made specifications designed for target applications. There are several means to modify properties of polymer, *viz*. blending, grafting, and curing. 'Blending' is the physical mixture of two (or more) polymers to obtain the requisite properties. 'Grafting' is a method wherein monomers are covalently bonded (modified) onto the polymer chain. Actually there is no time scale for the process of grafting, which can take minutes, hours or even days. Grafting may be considered: (i) grafting with a single monomer and (ii) grafting with a mixture of two (or more) monomers. The first type usually occurs in a single step, but the second may occur with either the simultaneous or sequential use of the two monomers.

This chapter deals with the change in surface morphology and surface chemistry of polymer material due to grafting of monomer on polymer backbone. Effect of temperature, monomer concentration and initiator on grafting rate is also discussed in also the part of this chapter

3.2 STRUCTURE AND MORPHOLOGY OF POLYMER

A detailed study of polymer structure has been carried out by many scientists [38-46]. The structural details of polymers are closely related with their

chemical and physical properties. The micro structural studies have revealed that the basic structural elements of high polymer are the linear chain molecules. The Russian Scientist Lebedev [47] deserves credit for having conceived the idea of a long chain structure. He polymerized butadiene and assigned to the product a cyclo-octadine structure. Soon afterwards, Lebedev [48] proposed chain structure for the polybutadine are rubber. Staudinger [49] differentiated linear and non-linear of network polymer. A lot of X-ray diffraction analysis of polymers was analysed by Dore, Mayer, Mark and Fredenberg etc. provided additional evidences for the higher molecular weight theory and long-chain structure. The description of the morphology and the interpretation of properties of semi-crystalline polymers remained a subject of a very deep and divisive debate for more than two decades. The basic structural elements of high polymer solids, are the chain molecules. The variety of their structure and flexibility permit different modes of organization. X-ray structure analysis is one of the most potential and direct techniques to study the structure of the material. When this method was applied to polymers, some interesting phenomena were observed revealing their internal structure. It was observed that a good majority of polymers diffracts X-rays like any other crystalline substances and many behave like amorphous materials giving very broad and diffuse X-ray diffraction pattern. On the basis of these results one can classify polymers into two broad groups-one which can be produced in crystalline state and the other in amorphous state

3.2.1 Crystalline Nature

The basis for cyrstallinity in polymer is quite complex. The simplest element of the structure of crystalline polymer is its crystalline unit cell formed by several atoms (parts of chains). In a unit cell each atom in the long chain molecules, is covalently bonded to its neighbour and the atom cannot move independently from one location to another, its neighbour must move in a highly prescribed manner since the nearest neighbor along the chain direction must always be the same atom.

This restricted mobility of bulky long chain of polymer molecules prevents 100% crystallinity, even if it shows similar results as that observed in metals i.e. increase of crystalline with annealing. The basic requirement for (crystal) crystallinity is chemical regularity along the polymer chain (tactic) that is why higher crystallnity is not possible in atactic. The X-ray crystallographic analysis of the unit cell of polyethylene by Bunn [50], marked an important point in the understanding of polymer science. Upto 1957, it was believed that the crystalline structure is of fringe miscelle type [46] and the chains are frozen into non-equilibrium position due to lack of mobility. A typical miscelle was supposed to be bundle of several tens of hundreds of different molecules which after leaving the miscelle and passing through amorphous regions, would randomly form other miscelles. It provided a basis for understanding most of the experimental data such as IR spectroscopy and X-ray diffraction patterns. On account of these two phases, fringed miscelle model enjoyed widespread recognition and popularity. Simple experiments independently performed by Fisher, Keller and Till [51, 52, 53] changed and entire course of study of the structure of polymers. The experiments led subsequently to the conclusion that mechanical properties are much more related to morphology as compared to cyrstallinity in single crystal of polyethylene. The spiral growth of the polymer crystal of poly oxymethlene is one of the most interesting complexities [54]. Multilayer structure with a small fraction of molecules interconnecting overlapping lamellas was observed when polymer was crystallized from more concentrated solutions. In bulk crystallization, lamellas were observed when polymer was crystallized from more concentrated solutions. In-built crystallization, lamella thickness upto an order of 100 A or even greater could be observed [55]. The lamella thickness depends on the molecular weight and crystallization conditions under atmospheric pressure. Inspite of the observation of larger crystalline dimensions, it was very strongly argued through the 1960s and much of the 1970s that the chains were regularly folded in bulk-crystallized polymers [38, 56, 57]. The major principles that were widely enunciated to support regularly folded chain in bulk crystallized polymers were that

1. The chain units in crystalline homopolymers should be assigned to either the interior of the crystallites or to the smooth interface.
2. Chain units connecting crystallities were rare events and, if they existed at all, adopted ordered confrontations.

3.3 CLASSIFICATION OF POLYMER

Polymer is the generic name given to the vast number of materials of high molecular weight. These materials exist in countless forms/numbers because of very large number and types of atoms present in their molecule. Polymers can have different chemical structure, physical properties, mechanical behavior, thermal and tensile characteristics etc., and can be classified in different ways.

3.3.1 Oleophobic and Oleophilic Polymers

Oleophobic and Oleophilic are frequently used descriptors of polymer surfaces. A polymeric surface is Oleophobic if it does not tends to absorb oil or be wetted by oil. A surface is Oleophilic if it tends to absorb oil or be wetted by oil. More particularly, the terms describe the interaction of the boundary layer of solid phase with liquid or vapor water.

Many surfaces in nature are highly oleophobic and self cleaning. For examples Electron Microscopy of the surface of Lotus leaves show protruding nubs about 20-40 micrometer apart each covered with smaller scale rough surface of epic-cuticular wax crystalloids. This is called, in general, the Lotus Effect shown in Fig. 3.1.

Lotus leaves have a mechanism for keeping the surface clean. The surface is covered with microscopic-size epidermal cells and covered with nano-order natural wax. The heterogeneity enhances the hydrophobic effect enormously.

The studies confirm that this combination of micrometer-scale and nanometer-scale roughness, along with a low surface energy material leads to apparent 150^0, a low sliding angle and self cleaning effect. Polymer surfaces with these properties are called “Superoleophobic–Polymer”

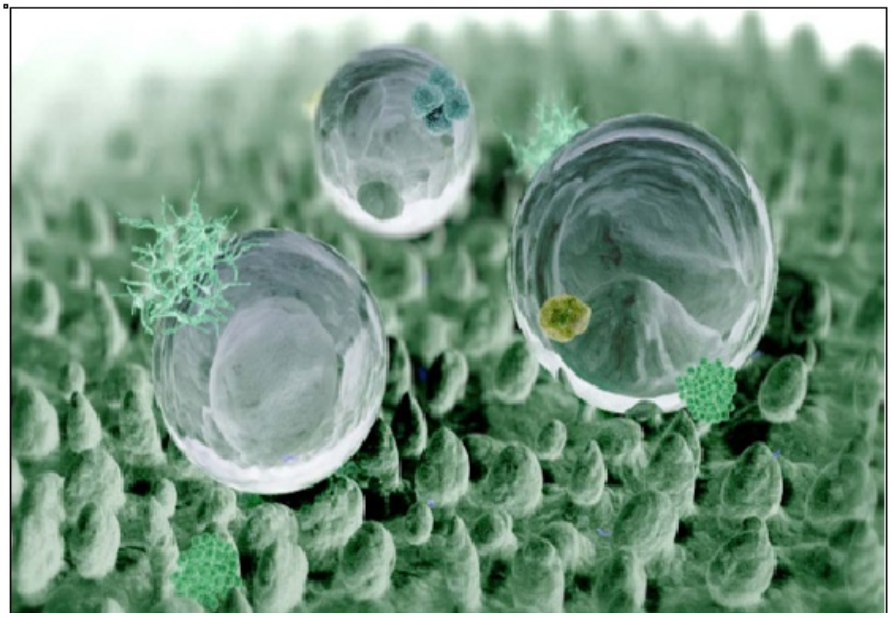

Fig. 3.1 : The Lotus effect

Superoleophobic polymer surfaces should have high contact angle and low contact angle hysteresis (the contact angle hysteresis is the difference between advancing and receding` angle). A composite solid-liquid-gas interface is important for analysis of these polymeric surfaces. The contact angle depends on several factors including surface energy, roughness, preparation and cleanliness of polymer surface. A polymer surface is superoleophobic if it has oil contact angle above 150°. The shape of drop of oil on the surface of polymer is the function of surface roughness. Superoleophobic surfaces have considerable technological potential for various applications due to their extreme water/oil-repellent properties. When two oleophilic bodies are brought into contact, any liquid present at the interface forms menisci, which increases adhesion/friction and the magnitude is dependent upon the contact angle. The next logical step in realizing super hydrophobic surfaces that can be produced is to design surfaces based on understanding of leaves. The effect of micro-patterning and nano-patterning on the hydrophobicity was investigated for two different polymers with micro-patterns and nano-patterns. Scale dependence on adhesion was also studied using atomic force microscope

tips of various radii. Studies on silicon surfaces patterned with pillars of varying diameter, height and pitch values and deposited with a hydrophobic coating were performed to demonstrate how the contact angle vary with the pitch. The effect of droplet size on contact angle was studied by droplet evaporation and a transition criterion was developed to predict when air pockets cease to exist. The dependence of the contact angle on the surface tension is considered for a liquid in contact with a smooth and rough solid surface, forming a homogeneous interface. The surface atom or molecule of liquid or solid has energy above that of similar atom and molecule in the interior, which result in surface tension or free surface energy being an important surface property.

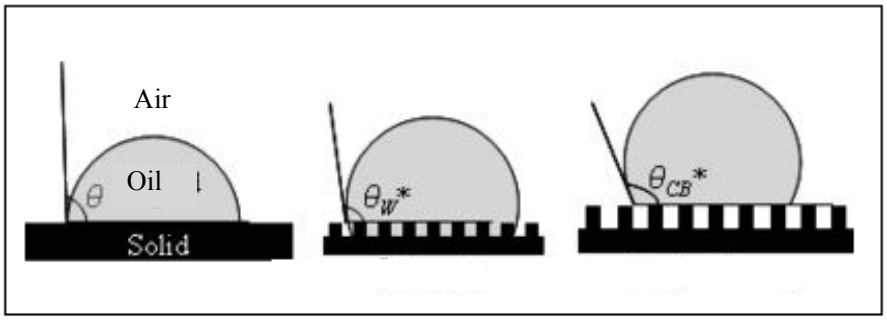

Fig. 3.2 : Variation of contact angle (θ) with surface roughness

This property is characterized quantitatively by surface tension γ, which is equal to work that is required to create unit area of the surface at constant volume and temperature.

The unit of γ is Jm^{-2} or Nm^{-1} and it can be interpreted either as energy per unit surface area or tension force per unit length of line at the surface. Young's equation is the equation responsible to describe the relation between contact angle θ and γ. The equation that governs the contact angle for heterogeneous polymer surface is called Cassie equation.

3.4 POLYMER SURFACE PROPERTIES: RELEVANCE TO ADHESION

Adhesion is the surface property relevant in many applications of polymeric materials. For instance, it might be necessary to have permanent ink on

polymer bags, or stable adhesion of a thin metal film on a polymer substrate. The necessary condition for the adhesion is the tight contact between the two parts. To achieve such interfacial contact, it is important to form strong and stable adhesive joints. The next stage is the generation of adhesion forces across the interface, and the nature as well as the magnitude of such forces is important. Another very important condition is how efficiently an adhesive layer wets the substrate. Before discussing adhesion theories, a short overview of surface forces and surface energies is given.

3.4.1 Surface forces

When a material interacts with another material or with the surrounding environment, it is the nature of the surface forces that determines the kind of interaction. There are long range forces (Vander Waal's and electrostatic) and short-range forces (hydrogen, acid-base, covalent). Vander Waal's forces are always present during the interaction. However, in some cases other kinds of forces such as electrostatic ones occur at the same time. These forces arise from the interaction between charged bodies, described by the charge and the potential. The combination of Vander Waal's and electrostatic effects in water (or a high dielectric constant solvent) is described by the so-called DLVO (Derjaguin, Landau, Vervey and Overbeek) theory of colloid stability. A more detailed review of all surface force theories is given by Garbassi [58].

Vander Waal's forces are a set of forces characterized by the same power dependence on distance. The important parameters in such a kind of interaction are the dipole moment, which arises from an uneven charge distribution in molecule, and the atomic polarizability, which indicates the tendency to redistribute the charge when the molecule is subjected to an electrical field. Owing to the process of charge redistribution, a molecule becomes a dipole and gives rise to an electrical field. An important contribution to the Vander Waal's forces is the interaction between the instantaneous dipole moment arising from the instantaneous position of electrons with respect to the nucleus. The Vander Waal's forces are always involved in the interaction between bodies, unlike other kinds of forces that require a particular feature [58].

The Vander Waal's contribution to the free energy of interaction between two molecules, w, is inversely proportional to the sixth power of the distance.

The free energy of interaction between macroscopic bodies, W, of different geometries can be described by a relationship of the kind:

where U is a factor which contains numerical constants and the relevant dimensions of bodies involved, D is the distance between the bodies, and $A = \pi^2 C \rho_1 \rho_2$ is the Hamaker constant (ρ is the number density of molecules in the solid).

The equations above show some important features of Vander Waal's interactions: the free energy of interaction between macroscopic bodies depends on the dimensions of the bodies (factor U). Vander Waal's forces between large bodies are more long-ranged than between molecules. Finally, the effect of the chemical and physical nature of the materials involved in the interaction on the interaction itself, is described by the Hamaker constant, which contains the relevant atomic or molecular parameters in the constant C. Even if Vander Waal's bonds are always present, the energy of such bonds is the lowest compared to other bond types. Therefore, they are only of significance in cases where other kind of bonding is not possible.

In addition to the long-range forces, short-range forces are also present in the interactions. These are usually strong covalent, hydrogen, or acid-base forces [58]. The structural feature required to form hydrogen bonds is a hydrogen atom covalently bonded to a highly electronegative element, such as O, N, F, etc. It is expected that hydrogen bonding plays an important role in the interaction between polymer surfaces bearing hydroxyl, carboxyl, amino or similar groups. When surface atoms and molecules come very close together, very strong forces arise from the overlap of electronic clouds and sharing of valence electrons. The process when intervening atoms lose their identity and create a new species is known as covalent bonding. The details of covalent bonding depend on the chemistry and the electronic and geometrical configuration of the species involved. Most synthetic polymers do not bear surface functional groups suited for covalent bonding, as chemical inertness is a desired property for many applications. When it is necessary to join the polymer covalently with another molecule, surface activation is applied by

means of surface modification introducing special functional groups suitable for covalent bonding.

In our work, our aim is to increase the oleophobicity of polymeric surface which need low surface energy. The surface energy of floropolymer are very less compared to other available polymers. Among all floropolymers, Teflon is the best choice for industrial application. It is obtained by free radical polymerization of tetrafluroethylene (PTFE) and was discovered by Roy J. Plunket and Jack Rebok at DuPoint in 1938.

Teflon is tough for a solvent or other agent to degrade the molecule if the carbon is 'out of reach'. With a ratio of four fluorine atoms to every two carbon atoms, the carbon-based heart of the molecule is essentially shielded from contact with any other molecule. The material is biologically inert and does not support biological growth i.e. it is non-pyrogenic.

Lubricant based on PTFE offer an extremely low static coefficient of friction, which stems from the extremely low intermolecular forces (Vander Waal's forces) in the PTFE molecule itself. PTFE materials are extremely stable and nonflammable; clean, dry, non-oily and non-staining. It could be cooled to –240°C without becoming brittle and it could be heated to 260°C without impairing its performance.

3.5 GRAFTING PROCEDURE

Considerable work has been done on techniques of graft co-polymerization of different monomers on polymeric backbones.

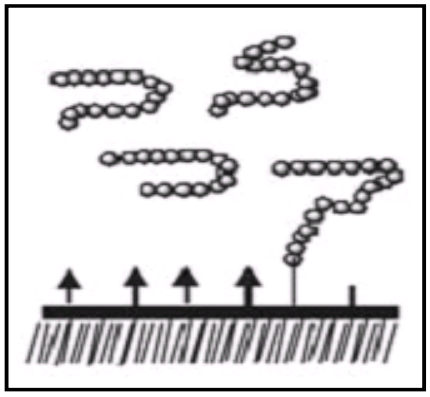

Fig. 3.3 : Schematic diagram of grafting of monomer on polymer backbone

The redox reaction is the conventional one to produce the free radicals. There are different redox reagents in which radicals can be generated and relayed to the polymer so that the grafting reaction occurs. The features of the chemical reactions are as follows:

Features:

a) Simple to carry out and no constraints in location point of view.

b) Feasibility exists at room temperature and also in the aqueous solution.

c) Extent of grafting can be controlled by tuning the reaction variables [*viz*. mixture composition (monomer/initiator), reaction time, and temperature].

The monomer molecules that are in the vicinity of the polymeric substrate become the acceptor of the radicals, resulting in chain initiation. Thereafter, they become the free-radical donors to the neighboring molecules. In this way, the grafted chains usually grow. These grafted chains terminate by coupling to yield the grafted copolymer.

Initiation : $| \bullet + M \rightarrow | - M_1 \bullet$

Propagation : $| - M_1 \bullet + M \rightarrow | - M_2 \bullet$

$| - M_2 \bullet + M \rightarrow | - M_3 \bullet$

. . . .

$| - M_{n-1} \bullet + M \rightarrow | - M_n \bullet$

Termination: $| - M_n \bullet + | - M_m \bullet \rightarrow$ Graft copolymer

3.6 EFFECT OF VARIOUS PARAMETERS ON POLYMER GRAFTING

The backbone polymer will affect the kinetics of grafting and crosslinking from two directions: (1) How readily can reactive centers be generated on the backbone by reactions with the initiator? (2) How readily can the reactive centers that were generated react with the monomer (to give grafting) or with other reactive centers (to give crosslinking)? If the radicals formed are highly reactive towards the monomer, they will readily give grafting, but if they are unreactive they are more likely to give crosslinking.

3.6.1 Effect of the Monomer

The relative reactivity of a monomer toward its own polymer and other radicals generated in the system will be most critical for grafting and crosslinking reactions. Monomers that readily homopolymerize will encourage grafting over crosslinking, and are more likely to generate significant amounts of homopolymer (e.g., butyl acrylate); monomers that are reluctant to homo-propagate will give short grafts and may enhance crosslinking (e.g., ethyl maleate) .

3.6.2 Effect of Temperature

The temperature of grafting medium is one of the most important reaction parameters that has a strong effect on the grafting yield during PTFE preparation. Generally, the increase in temperature of the grafting mixture upto certain level increases the degree of grafting. This may be due to the increase of the initiation and propagation rates of graft copolymerization. Increased in the degree of grafting with increasing temperature is also due to increase in the decomposition of the initiator leading to the formation of more free radicals and the generation of active sites on the polymeric backbone. But beyond that level the grafting rate decreases and the film brittled. Probably this is because at higher temperature, higher combination rates of monomer are obtained increasing homopolymerization reactions, which result in a decreased grafting rate [59, 60]. Decrease in percentage of grafting beyond optimum temperature is attributed to premature termination of the growing polymeric chains and to the occurrence of chain transfer reactions. Similar observations have been noted by Somanathan *et al.* with grafting methacrylic acid onto PET using Benzoyl peroxide as initiator [61].

3.6.3 Effect of Reaction Time

It has been observed that the grafting level increases initially with reaction time. The graft copolymerization rate increases to a maximum value at certain level of time. With an increase in reaction time, the free radicals have more time for reaction and therefore result in higher level of grafting. After some

time, all the initiator and monomer are used up. Thus no further change in grafting level was observed with increasing reaction time. The decrease in grafting may be due to the induced decomposition of the initiator leading to decrease in the concentration of the initiator and hence decrease in active radicals required to generate active sites on polymeric back bone. Similar observations were reported with grafting acrylic monomer such as acrylamide and glycidyl methacrylate on polyamide fibres using other initiators [62, 63].

CHAPTER 4

ION- POLYMER INTERACTION

4.1 INTRODUCTION

Ionization involves the transfer of sufficient energy to abound electron located in an atomic or molecular orbital of their radiated material so that the electron becomes free. Such ejected electrons eventually loose their excess kinetic energy via electronic, vibration and rotational excitation of the molecules in the medium. Radiation chemistry is concerned with the interaction of energetic charged particles (electrons, protons, alpha and other heavy particles) and high-energy photons (X-rays and γ-rays) with matter [64]. These interactions result in ionization (along with some of this energy being utilized in absorption and excitation) of the medium; hence charged particles, X-rays and γ-rays are frequently called “ionizing radiations". In contrast, visible and ultraviolet photons interact with matter leading predominantly to the excited state; though some ionization does take place when photons possess enough high energy. Thus, UV-visible radiations are called “non-ionizing radiations". When the ionizing radiations interact with matter, energy is transferred to the medium and this energy absorption leads to chemical changes in material [65]. According to the 1996 European Guideline of the European Atomic Energy Community (EURATOM), electromagnetic radiations with a wavelength of 100 nm or less is considered ionizing in character .This corresponds to photon energy of 12.4eV or more. The earlier applications such as X-rays for structure determination and medical purposes could only use the low doses available at that time and were best considered as limited to research and examination

purposes only. It is only with the advent of far more powerful sources, either nuclear or high voltage electrical pulses that one could seriously consider the practical applications of high energy radiation to the large-scale production or modification of materials by exposure to radiation [66].

The last four decades have witnessed the emergence of nuclear radiation as a powerful source of energy for chemical processing applications. Nuclear radiation is ionizing, which on passage through matter, gives positive ions, free electrons, free radicals and excited molecules. The capture of excited electrons by molecules becomes available for the chemist to play with. The fact that radiation can initiate chemical reactions or destroy micro-organisms has led to the large-scale use of radiation for various industrial purposes.

4.2 SOURCES OF ENERGETIC IONS

The basic requirement for performing any study in this field is, of course, energetic ions. They can be obtained in many ways e.g. by making use of radioactive sources such as α-particle or fission product emitters, or by exploiting nuclear reactions e.g. with neutrons from a reactor, that result in the emission of protons ,tritons, α -particles or fission products, depending on the type of irradiated material. Other particle ions become available by bombardment of ions on to appropriate target materials, via various types of nuclear reaction such as fusion reaction, spallation reaction etc.

The easiest way now-a-days, however, to obtain particles with sufficient fluence in a "convenient" energy range of, let us say some KeV to some GeV is to produce them in an appropriate particle accelerator There are hundreds of accelerators available in the KeV to lower MeV energy range and nearly a dozen accelerators which provide ionic particles with higher energies of several hundred MeV to a few GeV.

4.3 ION IRRADIATION

Sputtering is the removal of material from objects by energy transfer in collisions of energetic atomic projectiles. The first documented sputtering in the laboratory was done by Grove in 1852. He indicated the formation of a

deposit at the anode of a gaseous discharge tube and its removal when the polarity of the electrodes was reversed. After Grove's discovery, most observations on sputtering were made using gas discharges for almost a century. Isolation and characterization of the process using controlled ion beams in vacuum and characterization of materials started only in the second half of the twentieth century.

In this chapter, we presented the basic physical processes of the sputter phenomenon. Particle/polymer interactions including the mechanisms of energy deposition, penetration depth and damage distribution, theoretical ejection models of organic molecules, as well as ion induced effects in polymers are also discussed in this chapter.

4.4 ION POLYMER INTERACTION

When an energetic ionic particle penetrates through polymeric matter, it loses its energy in colliding with atoms of the matter [67, 68]. Materials consist of atoms, which further consist of nucleus and electrons with fixed energy electron rotating surrounding the nuclei in certain selected circular orbits defined by Bohr orbitals. Hence, the phenomenon of interaction of ion with matter can be microscopically understood in terms of its interaction with electron and nuclei. The collisions of ions with nuclei are elastic collisions, which results in the transfer of its energy to the target nuclei. However, the collisions between charged ions and electrons of the target materials are inelastic collisions resulting in excitation and ionization of target atoms. Both type of interaction processes i.e. interaction of ion with nuclei and electrons results in a loss of energy ion and they are termed as nuclear energy loss (Sn) and electronic energy loss (Se). Both, the electronic and nuclear energy losses of the ion depend on the energy and Coulombic nature of ion. In the case of electronic interaction, the nature of interaction is pure Coulombic while in case of nuclear interaction the nature of interaction is screened Coulombic. Let ΔE is energy that ion loses when moving a given path Δx in a polymer. Different ions will lose different amount of energy. The mean value of the

energy loss $\Delta E/\Delta x$ ($\Delta x \rightarrow 0$) for a large number of ions is termed the stopping power, S, which is the sum of both the energy losses and is given by:

$$S = -\frac{1}{\rho}\frac{dE}{dX} = Sn + Se \qquad Eq(4.1)$$

where Se and Sn are the electronic and the nuclear stopping powers respectively and ρ is the density of material,. The variation of energy loss of ions with the energy of the ion is shown in Fig. 4.1. The stopping power consists of two components, (i) nuclear (region I) and (ii) electronic stopping power (region II + III). At low energies (1 KeV/nucleon), the nuclear energy loss predominates. The ion collides with the target nuclei and transfer energy and momentum to the recoil atom [66]. As a result of which, atoms are displaced and the direction of the ion changes (elastic collision). At high energies (1 MeV/nucleon), where the velocity of ion is comparable with the Bohr velocity of orbital electrons, the ion interacts with the electrons of the target atoms as a result of which the target atoms are ionized and/or electrons are transferred to higher states (inelastic collision). Since the mass of the ion is much higher than the mass of the electron, the initial direction of the ion in the solid remains almost unchanged.

4.5 NUCLEAR ENERGY LOSS

The projectile ion moving with energy of the order of few KeV/nucleon interacts with screened or unscreened nuclei of the target atoms. The energy loss dE of an ion by elastic nuclear interaction, in a layer dx, is proportional to the atomic density N as well as the total energy transferred in all-individual collisions Tn [69]. Considering the interaction occurring between particles (ions) with energy E and target nuclei, the probability P(E) that a particle with energy E will transfer an amount of energy between T and T + dT to a target atom is given by [66, 67],

$$\frac{dP(E)}{dT}dT = NdX\frac{d\sigma(E)}{dT}dT \qquad Eqn.\ (4.2)$$

where E is the energy of the projectile particle (ion), T is the amount of energy transferred in colliding with target nuclei and $\sigma(E)$ represents the differential scattering cross-section. The average energy loss by the moving particle in the distance dx is obtained [66]:

For infinitesimal dx, the nuclear stopping power is:

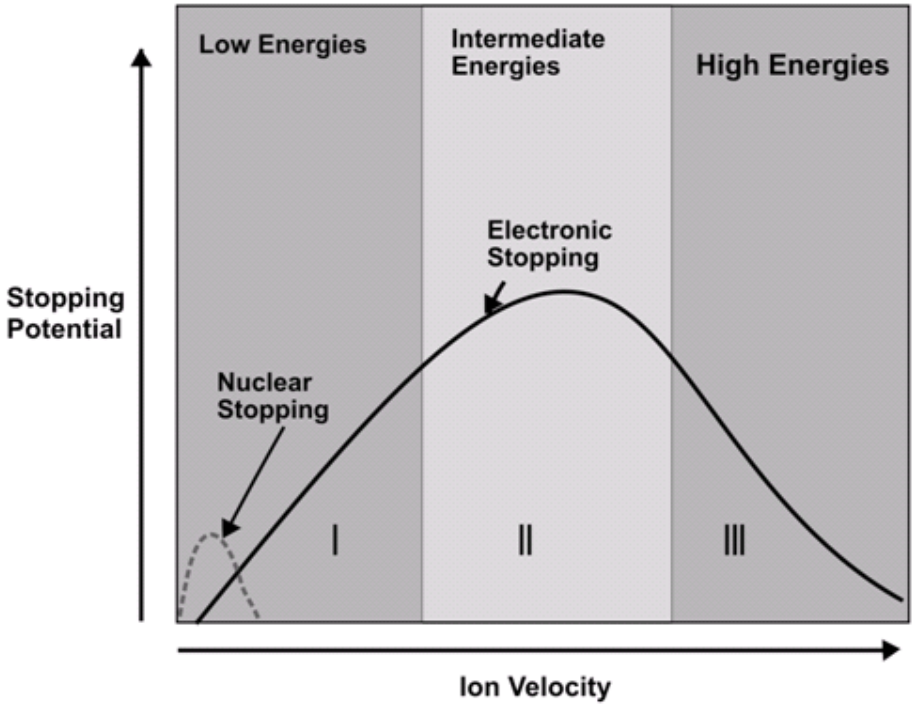

Fig. 4.1 : Nuclear / Electronic stopping Power w.r.t. incident ion energy

where dE/dX is the nuclear stopping power. The power limit in the integration T_{min} is the minimum energy transferred, and need to be zero. T_{max} is maximum transferable energy and is given by:

$$T_{max}=4\frac{M_iM_t}{M_i+M_t}\ E \qquad \text{Eqn.(4.5)}$$

where M_i and M_t are the masses of the projectile ion and the target atom respectively. The differential scattering cross section, $\sigma(E)$, depends on the inter-atomic potentials. For heavy particles of low velocity, and in the case of relatively distant collisions, the screening effect of the electrons cannot be ignored and resulting screening potential, which is called as screened coulomb potential is given by [69],

$$V(r)=\frac{Z_TZ_I}{r}\phi\left(\frac{r}{a}\right) \qquad \text{Eqn.(4.6)}$$

where $\phi(r/a)$ is the screening function, a is the screening parameter which is of the order of Bohr radius and r is the distance between the centre of mass systems. In the higher energy regime the contribution of Sn is insignificant. (Fig. 4.1)

4.6 ELECTRONIC ENERGY LOSS

Projectile ions moving with very high energy, having velocity comparable to Bohr velocity of orbital electrons, are called high energy loss. As they pass though the matter, they lose their energy mainly via interaction with electrons. The interaction of heavy ion results in knocking of electrons from electronic orbit leaving atom in excited/ionized state. Regions II and III illustrated in Fig. 4.1 are dominated by electronic energy loss. The difference between region II and III depends on the difference in velocities of ions passing through solid.

Bohr and others suggested that a criterion would be to assume that ion lose only those electrons whose orbital velocity (V_o) will be less than the velocity of projectile ion (V_I). This leads to ion charge fraction [67] on the projectile, which is given by:

$$\frac{Z^*}{Z}=\frac{V_1}{V_oZ_I^{\frac{2}{3}}} \qquad \text{Eqn. (4.7)}$$

where Z* is the effective charge on the ion, Z_I the total number of electrons surrounding the ion in its ground state, V_I is the ion velocity and V_0 is the Bohr velocity of an electron in the inner most shell of a hydrogen atom (V_0 = 2.2×10^8 cm/s). Furthermore it has been experimentally found that the ion charge fraction for a heavy ion is

$$\frac{Z^*}{Z} = 1 - \exp\ \frac{0.92 V_I}{Z^{2/3} V_0} \qquad \text{Eqn.(4.8)}$$

From equation (4.8) we have two limiting cases depending on the velocity of ion:

Case 1: When velocity of ion is less than the orbital velocity of electrons ($V_I < V_0$) i. e. in region II of Fig. 4.1. In this case the ion is not fully stripped ($\frac{Z^*}{Z} \leq 1$). Fermi and Teller have assumed that the electron gas in a solid behaves like a viscous medium and the projectile (ion) encounters on its path through electron clouds surrounding each target atom [68] . Later according to Lindhard-Scharff , the electronic stopping cross-section is proportional to the velocity of the ions, which is shown in Fig. 4.1 in the region II. The Lindhard-Scharff electronic stopping cross-section is given by

$$S_{LS}(E) = \varepsilon_L\, 8 \prod e^2 a_o\, N \frac{Z_I Z_T}{\left(Z_L^{\frac{2}{3}} + Z_T^{\frac{2}{3}}\right)^{\frac{2}{3}}} \left(\frac{V}{V_0}\right) = K_L\, E^{\frac{1}{2}} \qquad \text{Eqn. (4.9)}$$

where Z_L & Z_T are charges corresponding to the projectile ion and target atom, ε_L is the correction factor, a_o is the average Bohrs radius. It is clear that electronic energy loss is approximately proportional to the velocity or $E^{1/2}$ of the projectile ion.

Case 2: When velocity of ion is equal or greater than the orbital velocity electrons ($V_I \geq V_o$) i. e. beyond the Bragg peak (region III) (Fig. 4.1). [Fully stripped case ($\frac{Z^*}{Z} > 1$)] In region III, where the velocity of ion is greater than that of orbital velocity of electrons (beyond the Bragg peak), the charge state of the ion increases and finally becomes fully stripped of all its electrons and

moves with a velocity greater than the average velocity of the atomic electrons in the shells of the target atoms. In the fast collision case (region III), the influence of the incident particle on an atom may be considered as small external perturbation. The stopping cross-section decreases with increasing velocity because the projectile/ion spends less time in the vicinity of the atom. For non-relativistic ions, the dependence of electronic energy loss can be described by Bethe- Bloch formula [70] ,

$$S_{BB}(E) = \frac{8\pi Z_L^2\ e^4}{I_o \varepsilon_B} \ln \varepsilon_B \qquad \text{Eqn. (4.10)}$$

where

$$\varepsilon_B = \frac{2m_e V^2}{I_0 \varepsilon_{BB}} \qquad \text{Eqn. (4.11)}$$

and I_0 is the mean excitation energy of the target. "m_e" is the mass of electron and V is the velocity of ion. As a first approximation Eq(4.10) can be expressed as

$$S_{BB}(E) \propto \frac{1}{E} \propto \frac{1}{V^2} \qquad \text{Eqn. (4.12)}$$

Thus, the electronic stopping cross-section decreases with increasing the velocity of projectile ions as a first approximation of Bethe-Bloch formulation presented by Eqn.(4.12). In general, electronic stopping power can be divided into two regions: the low velocity, where the projectile is only to some extent ionized and the topping is proportional to V_I, the other is where the velocity is high and the projectile is fully stripped, leading to the inverse square relation of velocity with stopping power.

4.7 RANGE AND DAMAGE DISTRIBUTION

Due to interactions with nuclei and electrons of the target (polymer), an incident ion will be slowed down along a randomly shaped path. The projectile ion comes to rest at some depth in the target (Fig. 4.2). The depth of ion in material depends upon ion beam species, energy, the target material and on the energy deposition mechanism. The range is the total path length of the

projectile within the target. The mean projected range, , along the initial direction of the projectile is equal to the average depth of penetration for normal incidence only. The expression for the total range is given by:

—

where E_0 and E_f are the starting and the final energy of the incoming projectile, respectively. The final energy corresponds to the energy at which the projectile ion cannot overcome the potential barrier between the target atoms and hence comes to rest.

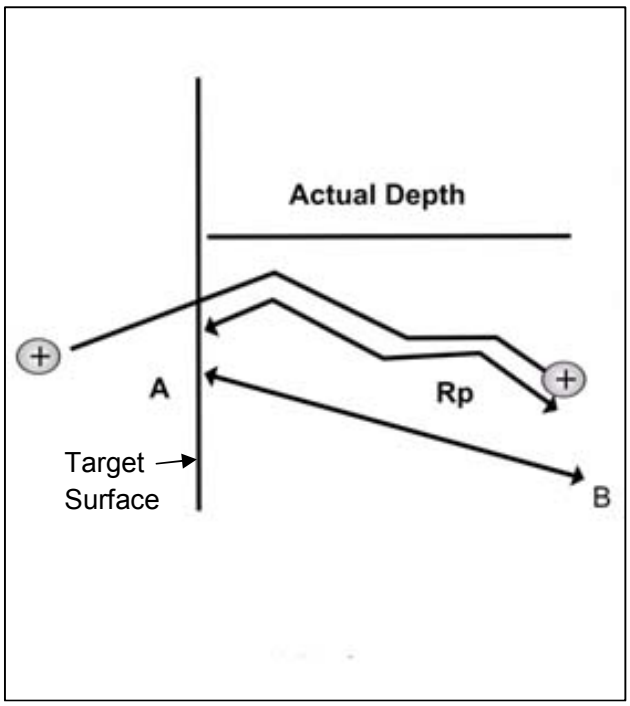

Fig. 4.2 : The comparison between actual depth, total length R_p and projected length AB =

For very small electronic stopping and low energy heavy ions in matter, the relationship between total range and projected range is a function of the mass ratio [71].

where M_1 is the mass of projectile and M_2 is the mass of target polymer.

The ion total range and projected range highly depend upon the energy of the primary projectiles and on the energy deposition mechanism. For low ion energies (0.1 – 100 KeV), direct momentum and energy transfer from incident particles to target atoms occurs. A number of large angle scattering processes leads to a broad, nearly spherical range distribution. The penetration range of such ions is up to several hundreds of nanometres. On the other hand, fast particles (ion energy > 100 KeV) transfer their energy via electronic excitation of molecules with the ion range exceeding several micrometers. High energy projectiles usually have straight particle trajectories nearly up to the end of their flight path, leading to sharp range distributions. We are interested in the surface modification which can achieved using ion energies up to 10 KeV. In our work we selected ion beam of 3 KeV The damage range for low ion energies is determined by molecular dynamics simulations, and up to date was not proved experimentally.

4.8 MECHANISM OF SPUTTERING

When ions with energies exceeding a few tens of eV impinge on the surface processes are initiated (Fig. 4.3):

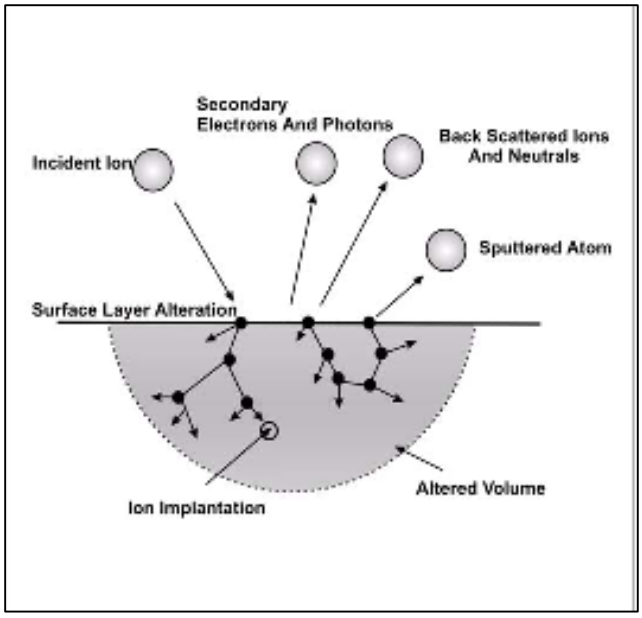

Fig. 4.3 : Interaction of ions with a surface.

A small fraction of the incident ions is backscattered by the collision with the surface and near surface atoms. These backscattered particles are mostly neutral atoms with a broad energy distribution. Ion impact at the surface of a solid may also give rise to the emission of electrons known as secondary electrons and photons. The electrons may be affected by potential emission, kinetic emission, or Auger emission from excited sputtered particles, while photons originate from backscattered or sputtered particles, excited in collisions with a surface atom before emission in the near-surface region of the solid. Near the end of their range, the injected projectiles are trapped and accumulate in the solid. This phenomenon is called ion implantation, and is extensively used in integrated circuit technology.

The major fraction of the incident ions is slowed down in collisions with atoms and electrons of the target. The energy transferred to the target atoms may initiate a collision cascade, possibly leading to the ejection of surface atoms or clusters of target atoms, i.e. sputtering. The ion impact may cause for the change in surface topography i.e. in the surface of a target material like the formation of vacancies and interstitial, changes in the stoichiometry [72].

If the ion beam energy is greater than the atom displacement energy the atom may be knock out from their original site. If the ion beam energy is less than the displacement energy then thermal vibration and phonon couple should be generated.

Incident ions slow down during the collision with atoms and electrons of the solid. During collisions, energy excess to lattice binding energy may be transferred to an atom of the solid. The energy transfer mostly occurs in direct collisions with target atoms. However, energy may be also transferred by local electronic excitation and ionization. In any case, atoms are removed from their original sites. Knock-on atoms may also remove other atoms from their lattice sites, creating a collision cascade. Surface or near-surface atoms will be emitted if they receive a momentum in the direction of vacuum with an energy enough to overcome the surface binding energy. It is a matter of chance whether the cascade leads to the sputter ejection of an atom from the surface, or whether the cascade propagates into the interior of the target, gradually

dissipating the energy of the primary ion impact. Usually more than 60 % of the ejected atoms originated from the first atomic layer, while the rest comes from the layers underneath [73].

There are two type of sputtering – (i) Chemical sputtering takes place if incident ions and the atoms of the solid interact chemically and volatile molecules are formed. The erosion rate may increase beyond the value corresponding to knock-on sputtering. (ii) Physical sputtering invokes a transfer of kinetic energy from the incident particle to target atoms and subsequent ejection of those atoms which have enough kinetic energy to overcome the surface binding forces. Based on the energy and mass of the incident ions, different collision cascade regimes can be distinguished [74] as discussed below:

Single-knock-on regime occurs with ion energies up to 1 KeV. The collision cascades are dilute and involve only a few atoms. Recoil atoms from ion-target collision receive sufficient energy to leave the surface, but it is not enough to generate cascades.

4.9 ION TRACKS IN POLYMER MATERIALS

Bombardment of solids with ions leads to the formation of damage zones in the material. Due to large amount of electronic energy deposition within a confined volume, the materials go into the molten state transiently in a narrow cylindrical region. The materials transformed into disordered state along the ion trajectory called latent track (damage zone created along the ion path). The formation of track is the result of high local electronic energy deposition along the ion path and hence conditions for track formation in different materials are different because of their different properties. Although a term short track is often used to designate a continous coloum of energy deposit (500-5000 eV) for a high energy particle, here its simply means a passage of an ion. When a positively charged ion passes through a medium, orbital electrons in the stopping medium are pulled off by an electromagnetic force. These charge seperation produce strong restoing forces. Consequently oscillation of

electrostatic nature are set up and the electron density, velocity and electric field all oscillate with the plasma frequency ω_p [75] ,

$$\omega_p = \left[\frac{14\pi ne^2}{4\pi\varepsilon_o m_e}\right]^{\frac{1}{2}} \qquad \text{Eqn. (4.15)}$$

where e(C) & m_e (Kg) are the charge and mass of the electron n(m^{-3}) is the electron number density of the medium and ε_o is the permitivity in free space. An expression for the radial extent of energy deposition proposed by Chatterjee and Schafer [76] is given below in terms of this plasma oscillation frequency of the stopping medium as

$$r_c = \frac{\beta C}{\omega_p} \qquad \text{Eqn. (4.16a)}$$

Where $\beta = V_{ion}/C$, r_c called the physical core, is the range of the fluctuation of electron density or energy for a period of plasma frequency pulse or is the range of uncertainity in a energy deposition at the epoch of intial energy deposition and can be derived from uncertainty principle $\Delta t\Delta E \approx \hbar$ with ΔE is the energy width over which an absorption can take place, later we define this energy as 'spur' r_c varies with ion velocity and defines the range of energy deposition which occurs at a period of 10-16s, which is the earliest significant time and can be estimated from $\Delta t.\Delta E \approx \hbar$ with $\Delta E \approx 20$eV for a relativistic particle (0.99C or ≈ 1000 MeV/Nucleon). In this time scale only electronic processes are possible since the time is too short for molecular motion. Molecular motion become importany at around 10-14s, molecular motion and a local temperature rise occur at ≈ 10 -13s, the diffusion process start at 10-12s [77].

The δ-rays also cause electronic excitation and ionization along the track,mostly outside the r_c. The maximum range of δ-rays can be calculated by the following relationship [78, 79]

$$r_{max} = KW_{max}^{\alpha} \qquad \text{Eqn. (4.16b)}$$

where

$$T_{max} = 4\frac{M_i M_t}{M_i + M_t} E \qquad \text{Eqn. (4.17)}$$

where $\alpha = 1.097$ for $T_{max} < 1$ KeV and $\alpha = 1.67$ for $T_{max} \geq 1$ KeV. It is the maximum energy of δ-rays [80] , where radial range of δ-rays is indicated by the radius r_{max}, which is called penumbra radius. Since a higher knock-on electron energy yields a smaller angle of ejection, r_p is always smaller than r_{max}. The value of r_p can be calculated by considering that the velocity and the energy of δ-rays in a radial direction are $V_\delta = V_{max}\cos\theta$ and $W = W_{max}\cos^2\theta$ and that the maximum momentum transferable to electron in a radial direction occure at the scattering angle of 45^0. Hence for $\alpha = 1$, $r_p = r_{max}/2\sqrt{2}$ can be derived using $r_\delta = KW$ and $W \approx W_{max}\cos^2\frac{2\pi}{4}$ and considering.

$$r_p = r_\delta \sin\pi/4 \approx KW_{max}\cos^2(\pi/4)\sin(\pi/4) = r_{max}\cos^2(\pi/4)\sin(\pi/4) \qquad \text{Eqn.(4.18)}$$

The initial average energy density with in core r_c and between r_c and r_p are given by Mageee and Chaterjee [81, 82] below. The energy density with the core is mostly from glancing collision and a small fraction of low energy knok-on electron which are trapped inside the core (IInd term in the equation below) r is the radial distance from the particle trajectory

$$\rho_{core} = \left[\frac{\left\{\frac{LET}{2}\right\}}{\pi r_c^2}\right]_{gl} + \frac{\left\{\frac{LET}{2}\right\}}{\left[2\pi r_c^2 \log\frac{e^{1/2}}{r_c}\right]_\delta}, r \leq r_c \qquad \text{Eqn. (4.19)}$$

$$\rho_{pen} = \frac{\left\{\frac{LET}{2}\right\}}{\left[2\pi r_c^2 \log\frac{r_p\sqrt{e}}{r_c}\right]_\delta}, r_c < r \leq r_p \qquad \text{Eqn. (4.20)}$$

$$\left[\frac{LET}{2}\right]_{gl} = [\pi r_c^2]\frac{\left[\frac{LET}{2}\right]}{[\pi r_c^2]_{gl}} \qquad \text{Eqn. (4.21)}$$

$$\left[\frac{\mathrm{LET}}{2}\right]_{\delta} = [\pi r_c^2]\frac{\left\{\frac{\mathrm{LET}}{2}\right\}}{\left[2\pi r_c^2 \log\frac{r_p\sqrt{e}}{r_c}\right]_{\delta}} + \int \rho_{pen}\,(r)\mathrm{d}(\pi r^2) \qquad \text{Eqn. (4.22)}$$

The energy density between r_c and r_p is transferred from δ-rays. The partitioning of linear energy transfer (LET) to glancing and knock on collison can be confirmed by converting the energy density to LET as shown in Eqn. (4.22). Values of the specific energy of the particle (Energy per Nucleon) is mentioned earlier. The ion path is thus describe by a cylinderical trajectory by the physical core with radius r_c approximately limiting distance from the particle trajectory at which an electronic excitation occur intially, and the penumbra with radius r_p (the outermost cylindrical boundary of the δ-rays or secoundary electrons). Another radius used in this model is the radius of chemical core (r_{ch}) which lies between physical core radius (r_c) and penumbra radius (r_p). The chemical radius defines a range where chemical reactions occure. The chemical radius (r_{ch}) is thus determined by the diffusion and reaction rates of active chemical species such as radical cations, anions, electrons and other activated chemical species. Shapes and sizes of track entites are first defined and then followed by the formation of active chemical species, diffusion and their interaction via. chemical and coloumbic forces.Some chemical species recombine and neutralize in the dense chemical sea, some diffuse out to the penumbra and mingle together with chemical species induced by δ-rays establishing a fairly large effective radius. Since the chemical radius is difficult to measure are calculate in reality, here, we use a term ‘effective’ radius instead, which defines the extent to which the energy density or radical concentration is significant for a given process. Crosslinking, scissioning and other chemical reaction occur on the effective radius. Most cross linking and other chemical reaction occurs near r_c, where concentration of radical and ion pairs are high because of slow migration of radicals in the viscous medium. In paticular for low LET tracks, δ-rays

develop independently and have very little on cross linking with increasing LET, which increases the effective radius.

4.10 ION IRRADIATION EFFECTS IN POLYMERS

Ion irradiation leads to irreversible changes in organic materials. Many polymers, when exposed to radiation, suffer main-chain scission leading to the formation of low molecular weight molecules and loss of their mechanical properties If there is no external supply of some reactive elements, and in the case of a higher concentration of primary radicals, the open polymeric bonds occurring during the scission have time to react with each other, thus initiating cross-linking, branching, or creation of double bonds. In such cases, the molecular weight increases. Both ion-induced chain scissions and cross-linking lead to irreversible changes in the polymer and its elastic properties. Scission ultimately degrades the polymer itself and the irradiated layer fails; if cross-linking dominates, adhesion failure occurs between the strongly cross-linked polymer regions and the underlying unirradiated polymer.

Some of the excited states may survive for larger period. These states are known as radicals. The lifetimes of such radicals are long enough to undergo chemical reactions. If a polymer is positioned in some reactive environment after irradiation, like treatment with reactive gases such as O_2, N_2, or placed in ambient atmosphere, long lived radicals may also react with reactive species forming special functional groups. For example, polymers treated with oxygen plasmas have oxygen-containing functional groups which lead to an increase in the polymer surface energy. Nitrogen-containing plasmas introduce carbon nitrogen functionalities required mostly for the improvement of wettability, printability, and bondability.

In fact, chemical changes caused by the irradiation of polymers are relatively small, but these changes produce major physical modifications. Interest in ion-induced polymer modification has grown significantly due to reports of large improvements in metal/polymer adhesion. These have been obtained using ion stitching with MeV ions, ion beam mixing and ion beam assisted deposition (IBAD). In the case of ion mixing, a thin metal film is placed on a substrate

and ~ 100 KeV ions are implanted into the specimen such that the resulting collisional mixing occurs in the interfacial region. According to the ideal surface modification idea, low energy ions are most suitable for surface modification. In the case of IBAD, the polymer surface is bombarded with low energy (100 – 1000 eV) ions during metal film deposition. Adhesion enhancement in this case has been attributed to a variety of mechanisms, such as chemical bond formation, contamination removal and interfacial mixing. An increase in the peel strength was also observed for polymer surface modification before metal deposition.

The morphology of polymer surfaces may also be changed during the irradiation forming cones or spike-like features. Especially great effect was observed on the surface of fluoropolymers.

CHAPTER 5

EXPERIMENTAL DETAILS

5.1 INTRODUCTION

This chapter deals with the details of the facilities used for experimenting and characterizing of polymer samples. The detailed methodology of experimental techniques and characterization of thin polymeric film of Teflon (PTFE 150 μm) by Field Emission- Scanning Electron Microscopy (FE-SEM), X-ray Diffraction (XRD), Energy-Dispersive X-ray Spectroscopy (EDS) and Contact Angle Goniometry (CAG) are discussed in detail.

This chapter provides the details of the facility used for exposing the surface of polymeric material by ion beam. The chemical grafting process detail is also given in this chapter. The surface morphology of pure PTFE sample and their comparative analysis after grafting and irradiate ions is studied through FE-SEM. Changes in elemental composition of polymeric thin film before and after the experimental work is examined through Energy Dispersive X-ray Spectroscopy. For any change in orientation of planes and crystallographic nature of PTFE (Teflon) sample after experimental work is explained and verified through XRD analysis. The oleophobic nature of sample PTFE is measured and explained by contact angle. The Contact angle goniometry is applied to measure the impact of grafting and ion-irradiation on oleiophobic nature of PTFE surface.

5.2 EXPERIMENTAL TECHNIQUES

The two step experimental techniques in opted for changing the surface morphology of PTFE thin film. First one being grafting of monomer on PTFE

surface to increase the roughness of film and the second step, for further enhancing the roughness of surface, consists of irradiating the grafted polymer with low energy ion beam.

5.2.1 Chemical Grafting

Commercially available polytetrafluoroethylene (Teflon) (Poly-1,1-difluoroethelene) films of thickness 150 μm obtained from Good Fellow, Cambridge Limited of Hontingen, U.K, is used for experimental work. The PTFE films were sliced into square strip of about 2cm x 2cm in size. To remove the organic residue on the surface, the PTFE film was washed with acetone, methanol and double distilled water respectively. The films were dried in air at room temperature and stored in a clean and dry box.

Benzoyl peroxide (BPO) [S D Fine-Chem. Limited, India] and acetone (Merck Specialties Private Limited, India) have been used in this work to create active site for grafting Methyl methacrylate (MMA), without further purification.

Fig. 5.1 : Laboratory image of grafting setup

Fig. 5.1 shows chemical grafting set -up designed at chemistry laboratory, University of Petroleum and Energy studies, Dehradun. The Three Neck Flask (T-Flask) apparatus was carefully rinsed with acetone in order to get high degree clean surface. The acetone cleaned Teflon of $2\,\text{cm} \times 2$ cm were weighed through an electronic digital balance (least count 0.001 grams) in dust and dirt free atmosphere. 50 ml of solution was prepared with different concentration of monomer Methyl Methacrylate (MMA) (X %) and was added to (100-X) % of distilled water. The initiator concentration being constant, 0.03gm benzoyl peroxide was dissolved in 10 ml of ethyl alcohol (ethanol). The Teflon film was put in the T-Neck containing monomer MMA, ethanol and BPO solution. One neck of the T-Neck flask was fit with thermometer, second neck was used to keep inserting/taking out PTFE film while the other neck was fit with water cooled condenser which condensed the solution vapour.

5.2.2 Irradiation facility at IUAC

The Low Energy Ion Beam Facility (LEIBF) at the Inter-University Accelerator Centre, New Delhi, provides Ar+ ion beam of energy 3KeV for irradiating grafted PTFE teflon surface of 150 μm thickness. The LEIBF consists of an Electron Cyclotron Resonance (ECR) ion source (Nanogan from Panteknik) installed on a high voltage deck. This is based on permanent magnet (NdFeB) design for radial and axial confinement of plasma. All the electronic control devices of the ECR source including high power UHF transmitter (10 GHz), are placed on a high voltage deck. These are controlled through optical fiber communication in multiplexed mode. Design and development of the high voltage platform, accelerating system and the beam lines with components thereof like electrostatic quadruple triplet lens, all metal double slit, beam steerers, Faraday cups, all metal pneumatic straight through valve, UHV scattering chamber have been indigenously made.

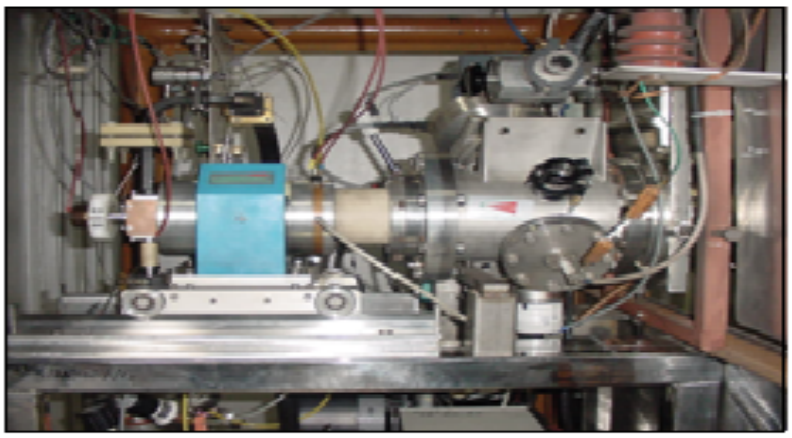

Fig. 5.2 : Image of ECR ion source at IUAC New Delhi

A standard Sputtering method is utilized to generate ion beam. A mechanised arrangement to insert a long thin wire (≈ 0.5mm thick) of Ar element to be introduced into the source plasma volume. The high energy electrons can sputter out the elements present in the wire, ionize them and produce the required beam.

5.3 CHARACTERIZATION TECHNIQUES

5.3.1 Contact Angle Goniometer

Contact Angle Goniometer is used to check wettability of liquid on solid surface. Lower the contact angle greater the wettability. It is used as a relative measure of surface energy. The primary parameter that characterize wetting is the static contact angle, which is defined as the measurable angle at which the liquid makes with solid. The contact angle depends on several factors, such as roughness, the manner of surface preparation and its cleanliness [83]. A drop of water for its surface tension "γ" properties, is applied to the surface and the contact angle is shown in the Fig. 5.3(a). It is measured with the contact angle goniometer. The real picture of drop of water on solid surface is shown in Fig. 5.3(b). For the contact angle and surface free energy measurements, the contact angle system called *Easy Drop-standard* from *KRUSS, Germany* with pre-installed Drop Shape Analysis Software *DSA-1* was used at Institute Instrumentation Centre, Indian Institute of Technology (IIT), Roorkee. The Pre-Installed DSA-1 Software is to determine the static and dynamic contact

angles using sessile drop and captive bubble method, to control camera, illumination, temperature, dosing modules, table movements, to measure, store and report measured contact angle values. The manual sample table moves the sample to the right position. Single or double dosing system deposits the drop onto the treated polymer surface by microsyring. The regular illumination and image sharpness together with 6-fold Zoom ensure optimal drop presentation. At equilibrium, the camera records the digital image and allows the perfect drop shape analysis [84]. This camera is equipped with goniometric eyepiece as shown in Fig. 5.4.

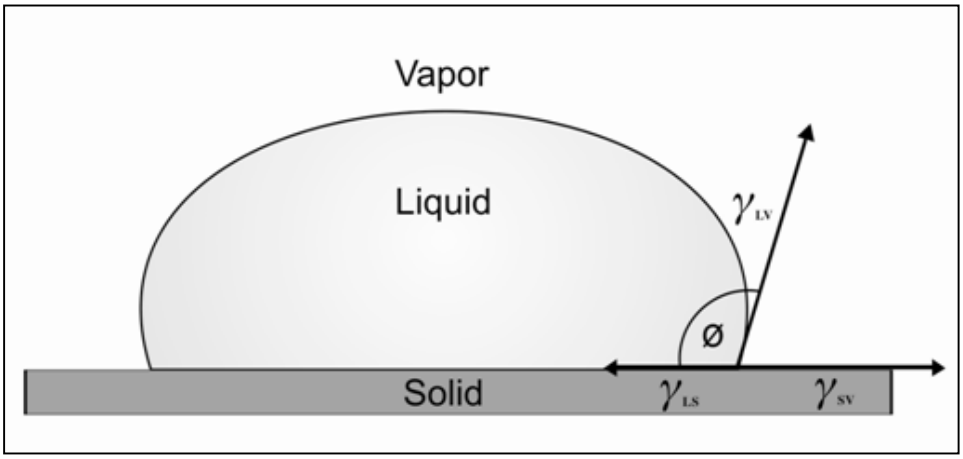

Fig. 5.3(a) : Droplet on solid surface

ϕ - represent Contact Angle

γ - Surface Tension between two interface

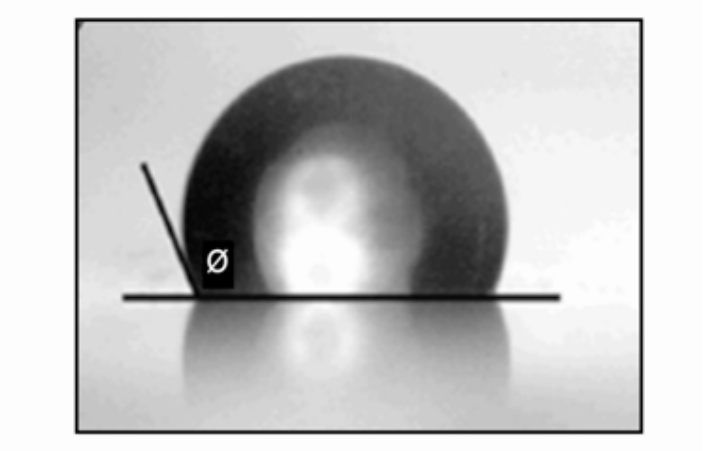

Fig. 5.3(b) : Real picture of contact angle - ϕ

The contact angle can be calculated and protocolled by Drop Shape Analysis Software (DSA-1) Software. There are two different methods of measuring contact angle from the drop, in first method contact angle can be measured on static drop. In this method the drop produced has a constant volume during the measurement while in second method the contact angle is measured on dynamic drop. The contact angle is measured while the drop is being enlarged or reduced, the boundary surface is being constantly newly formed during the measurement. Contact angles measured on increasing drops are known as advancing angles, those measured on reducing drops as receding angles. The difference between advancing angle and receding angle is known as contact angle hysteresis. The advantage of static contact angle measurement is that the needle does not remain in the drop during the measurement where as the case of dynamic contact angle measurement needle remains in the drop. In addition, when determining the contact angle from the image of the drop, it is possible to use methods which evaluate the whole drop shape and not just the contact area [85]. The static sessile drop was used for the determination of the contact angle on the deposited films by DSA-1 software. The basis for the determination of the contact angle is the image of the drop on the surface. In the DSA-1 software, the actual drop shape and the contact line (baseline) with the solid is first determined by the analysis of the grey level values of the image pixels. To describe this more accurately, the software calculates the root of the secondary derivative of the brightness level. A mathematical model which is used to calculate the contact angle is adapted to analyze the drop shape. The drop shape analysis is done by Young-Laplace (sessile drop fitting) method which is theoretically the most suitable method for calculating the contact angle. In this method, the complete drop contour is evaluated, the contour fitting includes a correction which takes into account the fact that it is not just interfacial effects that produce the drop shape, but that the drop is also distorted by the weight of the liquid it contains. After the successful fitting of the Young-Laplace equation, the contact angle is determined at the slope of the contour line at the 3-phase contact point. Moreover, this model assumes a symmetric drop shape, therefore it cannot be used for dynamic contact angles where the needle remains in the drop.

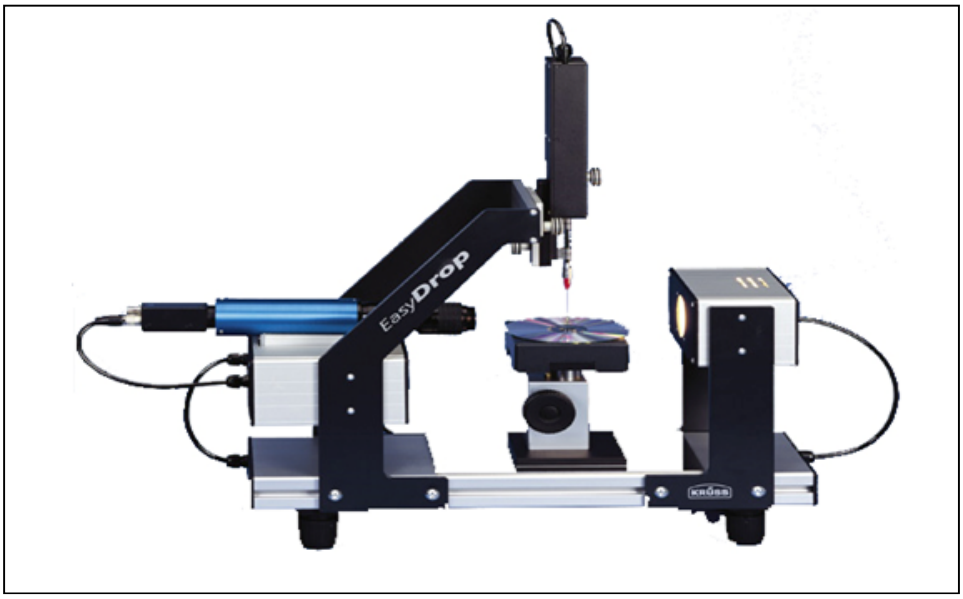

Fig. 5.4 : Easy Drop-Standard from *Kruss*, Germany with pre-installed software DSA-1

The drop in Fig. 5.5(a) has a neck at the top, which means that the two principal radii of curvature have opposite signs and cancel to some extent. At the bottom of the drop, the radii of curvature have the same sign, thus making the mean curvature larger [86]. The Young-Laplace equation can be written as coupled first-order differential equations in terms of the coordinates of the interface for an axis-symmetric surface in a gravitational field is given in Eqn.(5.1), where x and z are the horizontal and vertical coordinates, respectively, with the origin at the drop apex, s is the arc-length along the drop surface measured from the drop apex, and ϕ is the angle between the surface tangent and the horizontal Fig. 5.5(a).

$$\frac{dx}{ds} = \cos\phi$$

$$\frac{dz}{ds} = \sin\phi$$

$$\frac{d\phi}{ds} = \frac{2}{b} + \left\{\frac{\Delta\rho g}{\gamma}\right\} z - \frac{\sin\phi}{x}$$

$$x(0) = z(0) = \phi(0) = 0 \qquad \text{Eqn. (5.1)}$$

The parameter b is the radius of curvature at the apex of the drop or bubble, $\Delta\rho$ is the density difference between the two phases, and g is the acceleration of gravity. Numerical integration of Eqn.5.1 allows one to compute the shape of an axisymmetric fluid interface. Comparison of computed shapes with experimentally measured shapes of drops or bubbles is a useful method of measuring surface tension. If all lengths in Eqn.(5.1) are made dimensionless by dividing them by b, the resulting equation contains only one parameter,

$$\beta = \frac{\Delta\rho g b^2}{\gamma} \qquad \text{Eqn. (5.1a)}$$

which is called the Bond number (or shape factor). The shape of an axisymmetric drop bubble or meniscus depends only on one dimensionless parameter. The Bond number can also be written as

$$\beta = 2\frac{b^2}{a^2} \qquad \text{Eqn. (5.1b)}$$

where "a" is known as the capillary constant and has units of length [5] .The shape of an axisymmetric sessile drop Fig. 5.5(b) depends on only a single parameter the Bond number. The Bond number is a measure of the relative importance of gravity to surface tension in determining the shape of the drop. For bond numbers near zero, surface tension dominates and the drop is nearly spherical. For larger bond numbers, the drop becomes significantly deformed by gravity. In principle, the method involves obtaining an image of the drop and comparing its shape and size to theoretical profiles obtained by integrating Eqn.(5.1) for various values of β and b. Once β and b have been determined from shape and size comparison, the surface tension is calculated by using the formula:

$$\gamma = \frac{\Delta\rho g b^2}{\beta} \qquad \text{Eqn. (5.2)}$$

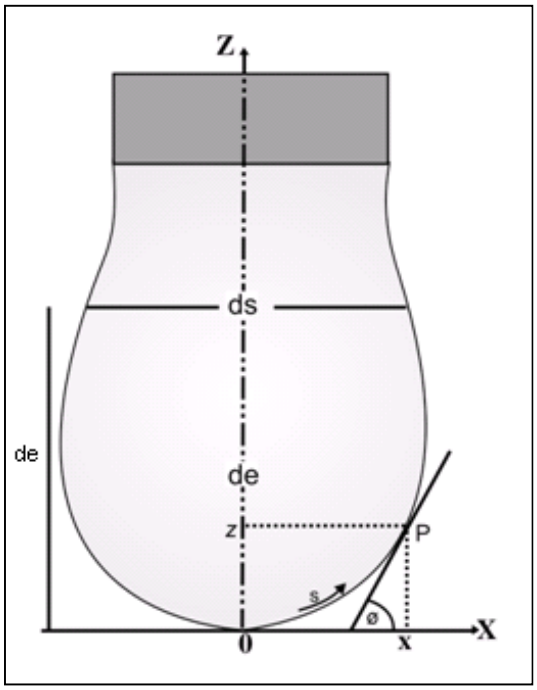

Fig. 5.5(a) : Pendant Drop showing the characteristic dimensions d_e and d_s and the coordinates used in The Young-Laplace equation

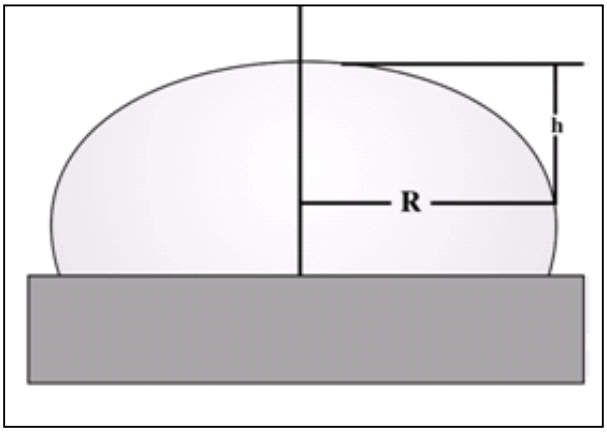

Fig. 5.5(b) : Sessile drop showing the characteristic dimensions R and h

For pendant drops, the ratio d_s/d_e is co-related to a shape factor H (d_s/d_e is the function of shape factor) from which surface tension is calculated according to

$$\gamma = \frac{\Delta\rho g {d_e}^2}{H} \qquad \text{Eqn. (5.3)}$$

From the sessile drop, the contact angle for the deposited films are determined by DSA-1software**.** A digital image of a sessile drop can be analyzed on a desktop computer in 1 or 2 seconds. Typically, several hundred coordinates on the edge of the drop are located with subpixel resolution by computer analysis of the digital image. The size, shape, horizontal and vertical offsets of the theoretical profile given by Eqn.(5.1) are varied by varying four parameters: β, *b* and the pixel coordinates of the drop apex, X_o and Z_o. A best fit of the theoretical profile to the measured edge coordinates is obtained by minimizing an objective function. The algorithms can simultaneously track the surface area and volume of the drop or bubble.

The contact angles θ were calculated by the program using the Young-Laplace function DSA-1 Software. The software allows to take photographic images of the drop which will be shown in the results part. Contact angle measurements depend strongly on the environmental conditions [87,88]. The surface preparation, environmental temperature, drop size were kept constant, and the whole experiment was performed in one day in order to be able to compare results [89]. The most widely used method is to measure the angle of a sessile drop resting on a flat solid surface using a goniometer-microscope equipped with an angle-measuring eyepiece or, more recently, a video camera equipped with a suitable magnifying lens, interfaced to a computer with image-analysis software to determine the tangent value precisely on the captured image. The contact angle measuring system is shown in Fig. 5.4 and the experimental setup of the system (DSA-1 Easy Drop) procured from Kruss, Germany is shown in Fig. 5.6. Before the measurements are taken, the measurement stage is leveled by adjusting the stage supporting table. A substrate or sample whose contact angle is to be determined is then placed on the stage.

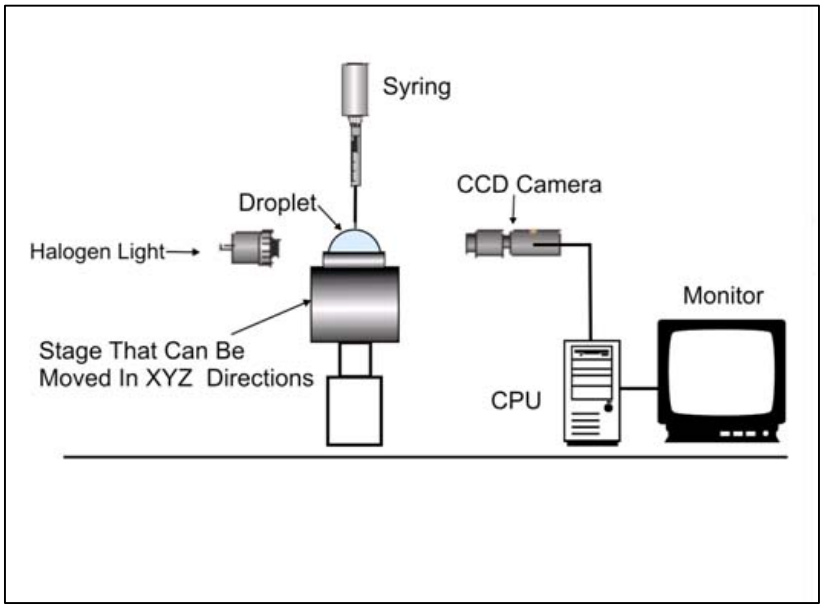

Fig. 5.6 : Experimental setup of the DSA Easy Drop

The instrument uses a micro-syringe mounted in an arm that can be moved in vertical and horizontal direction to dispense a liquid drop over the measurement location on the sample.

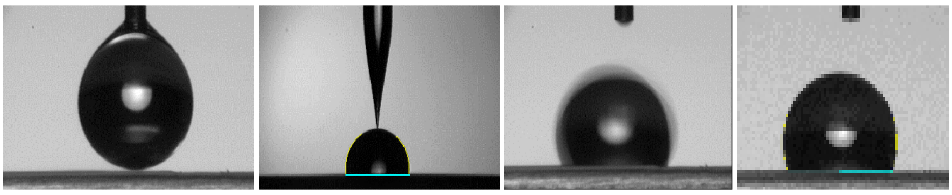

(A) (B) (C) (D)

Fig. 5.7 : Screen display of DSA1

(A)-Drop just above surface, (B)-Just before detachment (C)-Drop at touch-off. (Motion is Present) (D)-Drop is motionless

The syringe will handle drop volumes from 3 to 10 µl with 0.1 µl resolution. Once the position of the syringe is adjusted according to the sample, the drop formed at the tip of the needle is lowered slowly and forms the contact angle when it strikes the surface of the sample [90]. Drop images are acquired using a camera and in line incident illuminator software controlled optical halogen

lamp. The action appears live on the computer screen and the salient images are captured to the computer's memory for later image analysis. The camera can capture images at very fast rate of around 25-60 frames per second. The measurement location on the platform can be shifted to facilitate formation of another drop on the same surface. So the drop profile is photographed, the evaluation of the drop image takes place in the window of the software: the baseline is determined automatically for measuring the contact angle and the tangent of the sessile drop profile at the three-phase contact point drawn onto the image is used to determine the value of the contact angle and surface energy by the DSA-1 software. Fig. 5.7 shows the photograph captured by camera at various stages [91].

The contact angle of liquid Methyle iodide (CH_3I) on PTFE surface provide quantifiable measure of oleiophobic nature of surface. The contact angle of CH_3I for pure, grafted and irradiated (after grafting) samples at various grafting temperature is measured and analysed. The data pertaining to this is described in future chapters (6 and 7).

5.3.2 X-ray DIFFRACTION (XRD)

X-ray diffraction is the most powerful tool for determining the structure of solid matter and finds wide range of applications in material characterization. X-ray diffraction is a non-destructive technique. X-ray diffraction (XRD) was direct evidence for the periodic atomic structure of crystals.

Applying trigonometry (Fig.5.8), the lower beam must travel the extra distance A B'+ B'C to continue traveling parallel and adjacent to the top beam. Recognizing d as the hypotenuse of the right triangle, we can use trigonometry to relate d and ϕ to the distance A B'+ B'C. The distance A B' = d sinϕ because A B' = B'C hence $n\lambda = 2$ A B' The angle between the diffracted beam and the incident beam is always 2θ Fig. 5.8, and it is this angle, rather than θ, which is usually measured experimentally

$$n\lambda = 2d\sin\theta \qquad \text{Eqn. (5.4)}$$

where n is the order of plane, λ is the wavelength of incident radiation and d is the interplanar distance between the lattice planes which is given by

$$d = \left[\frac{h^2}{a^2} + \frac{k^2}{b^2} + \frac{l^2}{c^2}\right]^{-\frac{1}{2}} \qquad \text{Eqn. (5.5)}$$

where *h, k* and *l* are the indices of the lattice planes and *a, b, c* are the dimensions of the unit cell. From the above relations one can easily evaluate the lattice parameters when the values of d and corresponding values of θ (for fixed value of λ) are known [20]. The schematic diagram of XRD is shown in Fig. 5.9(a). The radiation (Cu K_α) emanating from the X-ray tube is diffracted at the specimen and recorded by a detector [92].We have used X-ray diffractometer (Bruker D8 Advance diffractometer) Fig. 5.9(b). The specimen is rotated at constant angular speed in such a way so that angle of incidence of primary beam changes, while detector moves about the specimen at twice the angular speed. The diffraction angle (2θ) is thus always equal to double the glancing angle (θ).

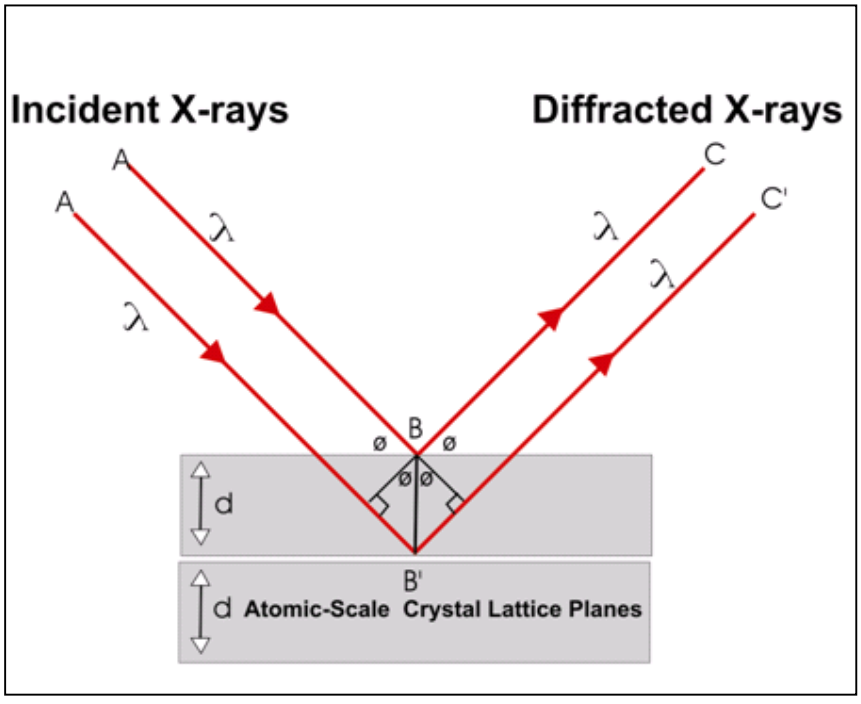

Fig. 5.8 : Bragg's Law Reflection

The diffracted X-ray exhibit constructive interference when the distance between paths ABC and A′B′C′ differs by an integer number of wavelengths (λ)

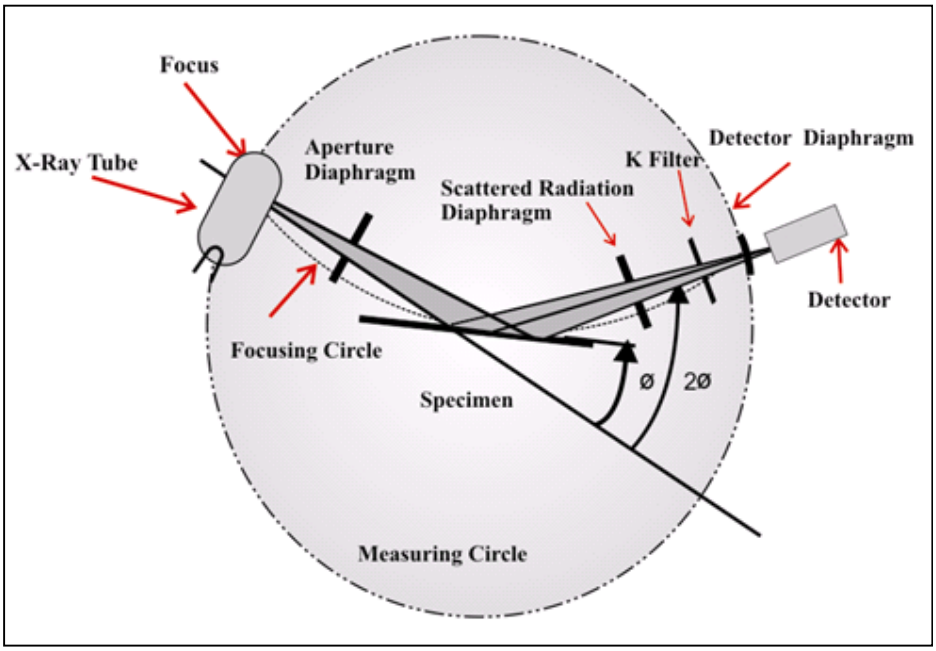

Fig. 5.9 (a): Aperture Diaphragm is arranged between the tube and specimen

Whenever the Bragg condition, $2d\sin\theta = n\lambda$, is satisfied, the incident X-ray beam is diffracted at the specimen and reaches the detector. The detector converts the X-ray quanta into electron pulses, which are recorded by recorder. Bruker D8 Advance diffractometer uses NaI scintillation counter as a detector Fig. 5.9(a) and Fig. 5.9(b) are used for this purpose. It can detect the diffracted radiations in the wavelength ranging from 0.5 to 3 Å. Monochromators are used to suppress the undesired portions of radiation. To restrict the irradiated specimen area, aperture diaphragm is arranged between the tube and the specimen as shown in Fig.5.9(b). The second aperture diaphragm shields the strong scattered radiation of the first aperture diaphragm. The resolution depends upon the detector diaphragm. The scattered radiation diaphragm is used to suppress undesired scattered radiation. The crystallographic information is obtained by evaluating 'd' values and indexing of reflections. The characteristics diffraction pattern of a given substance can always be obtained whether the substance is present in pure

state or as one constituent in a mixture of several substances. This fact is the basis of the diffraction method of chemical analysis.

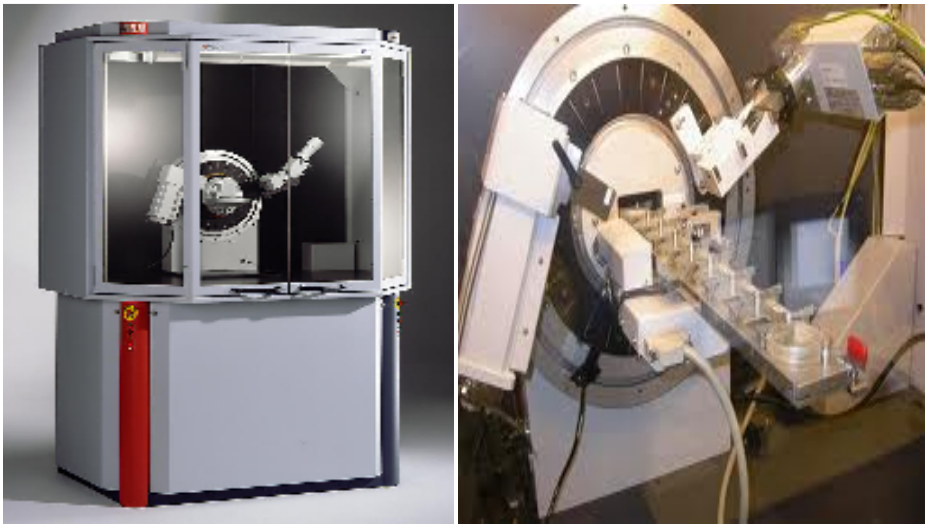

Fig.5.9(b) : Bruker D8 Advance diffractometer uses NaI scintillation counter as a detector (IIT R)

X-ray diffraction pattern is characterized by a set of line positions (2θ) and a set of relative intensities (I). The angular position of lines depends on the wavelength of the incident ray and spacing (d) of the lattice planes. The technique can be used for quantitative analysis in which the concentration of phases are calculated by determining the area of the peak, since the intensity of diffraction lines due to one constituent of a sample depend upon the concentration of that constituent in the sample specimen [93] . The qualitative analysis for a particular substance is accomplished by identification of the pattern of that substance. Any change in the orientation of the planes of the PTFE due to irradiation of ion beam (after grafting) is provide the direct evidence that the surface morphology of PTFE is changed. The data pertaining to XRD is analyzed and discussed in chapter 7.

5.3.2.1 Specimen beam interactions

When an incident beam electron strikes the surface of a sample, it undergoes a series of complex interactions with the nuclei and electrons of the atoms of the sample. The interactions produce a variety of secondary products, such as electrons of different energy, X-rays, heat, and light as shown in Fig. 5.10.

Many of these secondary products are used to produce the images of the sample and to collect additional data from the sample. The interaction is usually described as teardrop or pear-shaped. In whole samples, the volume (both depth and width) of the interaction varies directly with the accelerating voltages and inversely with the average atomic number of the sample. The interactions between incident electrons and the atoms of the sample may be elastic or inelastic Fig. 5.10 [94]. Elastic interactions occur between incident electrons and the nucleus of atoms of the sample and are characterized by a large angle deflection of the incident electron, as well as little energy loss by the incident electron. In elastic interaction occur between the incident electrons and the orbital shell electrons of the atoms of the sample and are characterized by a small angle deflection of incident electron, as well as much energy loss by incident electron [95] .

5.3.3 FIELD EMISSION SCANNING ELECTRON MICROSCOPY (FE-SEM)

Scanning electron microscopy (SEM) is a technique that uses electrons rather than light to form an image. There are many advantages to using the SEM instead of a light microscope. The SEM has a large depth of field, which allows a large amount of the sample to be in focus at one time. The SEM also produces images of high resolution, which means that closely spaced features can be examined at a high magnification. Preparation of the samples is relative easy since most SEMs only require the sample to be conductive. The combination of higher magnification, larger depth of focus, greater resolution, and ease of sample observation makes the SEM one of the most heavily used instruments in research areas. It detects the secondary and back-scattered electrons from a sample surface bombarded by an electron beam scanning its surface. The contrast in an SEM image reveals information about the surface morphology and composition of the material. The comparative analysis of FE SEM output of PTFE sample, grafted PTFE and ion irradiated PTFE is considered in chapter 6 and chapter 7. Fig.5.11 shows a schematic diagram of the field emission scanning electron microscope. The source of the electrons is electron gun. The beam is emitted with in a small specials volume with a small angular spread and selectable energy. The electrons are accelerated to high kinetic energies by using an anode at high positive potential. The first

condenser lens that works in conjunction with the condenser aperture helps to narrow the beam and also limit its current. The second condenser lens then forms the electrons into a very thin, coherent beam. The beam is scanned point by point over the sample (like in a television) by using a set of scanning coils.

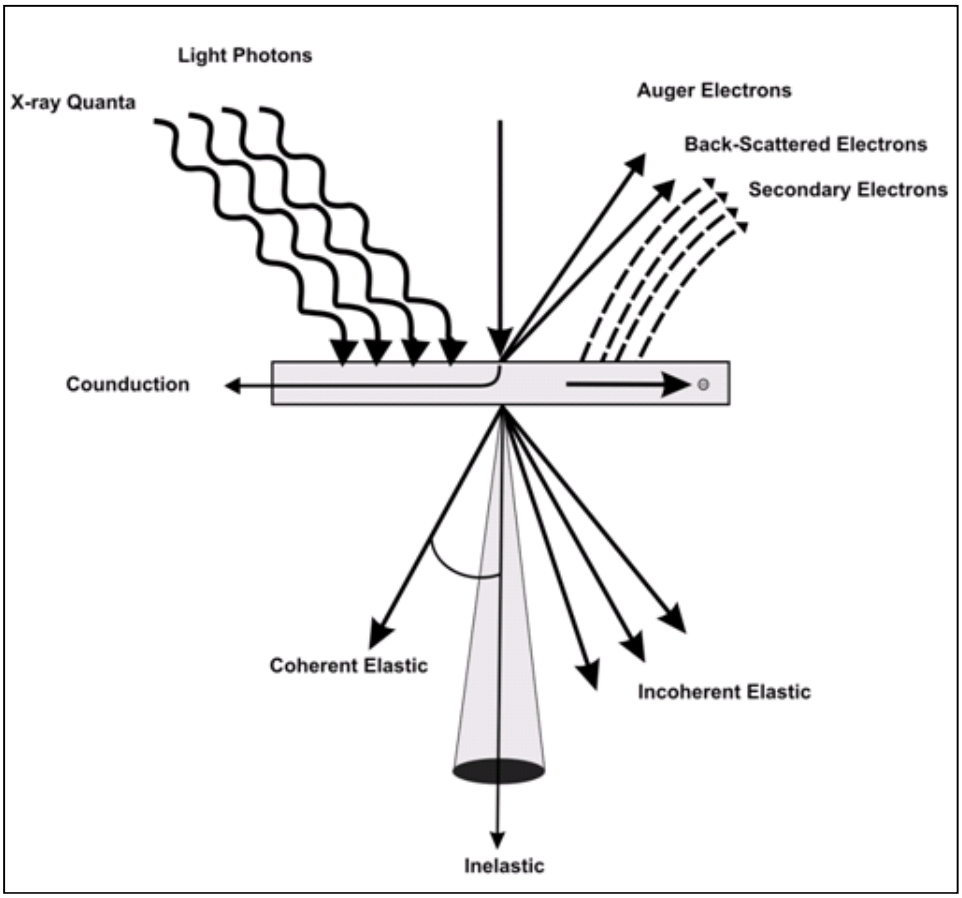

Fig. 5.10 : Schematic Diagram of the beam interaction of specimen

The objective lens does the final focusing of the beam on the sample. At each point the number of secondary and back-scattered electrons reaching the detector are counted to be used for determining the relative intensity of the pixel representing that point in the final image. The higher the atomic number of the specimen material, the greater is the number of secondary electrons that reach the detector, giving rise to a higher intensity in the image. Since all metals are conductive so no special sample preparation is required for them but all non-metals need to be made conducting by covering the sample with a thin layer of conductive material like gold [96]. SEM is a destructive

technique in the case of non-metals since during coating the gold atoms fall and settle onto the surface of the sample producing a thin gold coating. We have used the Field Emission Electron Microscope (FEI Quanta 200F model) with resolution of 2nm and possible magnification 500000 diameters to study the surface morphology of the nanocrystalline thin films and nanopowder and is shown in Fig. 5.12. FE-SEM uses field emission electron gun which provides improved special resolution down to 1.5 nm that is 3 to 6 times better than conventional SEM and minimizes sample charging and damage. In conventional SEM electrons are thermionically emitted from a tungsten or lanthanum hexaboride (LaB_6) cathode and are accelerated towards an anode, alternatively electrons can be emitted via field emission (FE). Tungsten is used because it has the highest melting point and lowest vapour pressure of all metals, thereby allowing it to be heated for electron emission. The electron beam, which typically has an energy ranging from a few hundred eV to 50 keV, is focused by one or two condenser lenses into a beam with a very fine focal spot size (1 to 5 nm).

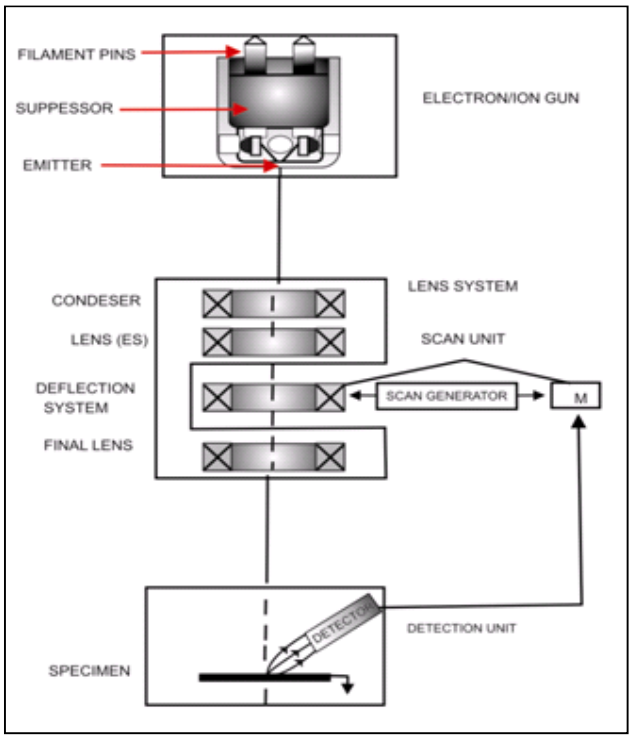

Fig. 5.11 : Schematic Diagram of FE-SEM

Fig. 5.12 : Photograph of FE-SEM (FEI Quanta 200F)

The basic mechanism of field emission is that a high voltage applied between a pointed cathode and a plate anode causing the current to flow [97]. The field emission tip is generally made of a single crystal tungsten wire sharpened by electrolytic etching. A tip diameter of 100 to 1000 Å is used, with the apparent source size much less than that. The field emission process itself depends on the work function of the metal, which can be affected by adsorbed gases. This is the reason a very high vacuum is required [98].

5.3.4 ENERGY DISPERSIVE X-ray SPECTROSCOPY (EDS)

Using the energy dispersive x-ray analysis (EDS) attachment with the SEM, elemental composition analysis can be done. An EDS spectrum normally displays peaks corresponding to the energy levels for which the most X-rays had been received. Each of these peaks is unique to an atom, and therefore corresponds to a single element. The higher a peak in a spectrum, the more concentrated the element is in the specimen. Fig. 5.13 represent the schematic diagram of the EDS system. Interaction of an electron beam with a sample target produces a variety of emissions, including X-rays. An Energy-Dispersive X-Ray Spectroscopy (EDS) detector is used to separate the characteristic X-rays of different elements into an energy spectrum. EDS system software is used to analyze the energy spectrum in order to determine

the abundance of specific elements. EDS can be used to find the chemical composition of materials down to a spot size of a few microns, and to create elemental composition maps over a much broader area. These capabilities provide fundamental compositional information for a wide variety of materials. EDS systems are typically integrated into a SEM. It includes a sensitive X-ray detector, a liquid nitrogen for cooling, and software to collect and analyze energy spectra. The detector is mounted in the sample chamber of the main instrument at the end of a long arm, which is itself cooled by liquid nitrogen. With modern detectors and electronics, most Energy-Dispersive X-Ray Spectroscopy (EDS) systems can detect X rays from all the elements in the periodic table above beryllium (Z = 4) if present in sufficient quantity. Most applications of EDS are in electron column instruments like the scanning electron microscope (SEM). X-ray spectrometers with X-ray tube generators as sources and Si(Li) detectors have been used for both X-Ray Fluorescence Spectroscopy (XRF) and X-ray diffraction (XRD).With a radioactive source, an EDS system is easily portable and can be used in the field more easily than most other spectroscopy techniques. With a minimum detection limit (MDL) of 100-200 ppm for most elements, an EDS system is capable of detecting less than a monolayer of metal film on a substrate using Kα lines at moderate accelerating voltages of 5-15KeV [99].

EDS detector normally consists of a small piece of semiconducting silicon or germanium which is held in such a position that as many as possible of the X-rays emitted from the specimen fall upon it. Since X-rays cannot be deflected, the detector must be in line of sight of the specimen. This means that in a scanning electron microscope (SEM), it normally occupies a similar position to the secondary electron detector. In order to collect as many X-rays as possible, the silicon should be as near to the specimen as is practicable. In SEM, it may be possible to place the detector 20mm or less from the specimen.

If a voltage is applied across the semiconductor, a current will flow as each X-ray is absorbed in the detector and the magnitude of the current will be exactly proportional to the energy of the X-ray. In practice, if pure silicon is used, the

current generated is minute compared with the current which flows normally when a voltage is applied; in other words the resistivity is too low. This is overcome by three stratagems which combine to make the final detector seem rather more complicated than it really is. The resistivity of the silicon is increased by (i) making the whole detector a semiconductor p-i-n junction which is reverse biased, (ii) doping the silicon with a small concentration of lithium and (iii) cooling the whole detector to liquid nitrogen temperature (77K) (Goodhew *et al.* 2001). Fig. 5.13 shows the Si(Li) detector which is the most commonly used energy-dispersive detector. The lithium atoms are used to compensate the relatively low concentration of grown-in impurity atoms by neutralizing them. In the diffusion process, the central core of the silicon will become intrinsic, but the end away from the lithium will remain p-type and the lithium end will be n-type, this results in a p-i-n diode. A reverse bias electrical field in a range of 100-1000 volts is applied to thin layers of gold evaporated onto the front and back surface of the diode. The detector shown schematically in Fig. 5.13 consists of Si(Li) semiconductor junction in which the ‘i' region occupies most of the 6mm thickness. Thin layers of gold are necessary on both surfaces of the detector so that the bias potential can be applied. The film of gold on the outer face of the detector must be as thin as possible so that very few X-rays are absorbed in it; a layer only 20nm thick provides adequate conductivity. When an X-ray enters the intrinsic region of the detector through the p-type end, each incoming X-ray excites a number of electrons into the conduction band of the silicon leaving an identical number of positively charged holes in the outer electron shells which in turn produces a number of electron-hole pairs in the detector. It required 3.8eV of energy for one such pair, so for example a 5.4KeV X-ray absorbed by the silicon atoms will produce about 1684 electron-hole pairs or a charge of about 2.7×10^{-13} Coulombs. The current which normally passes between the gold electrodes is very small indeed until an X-ray enters the detector, then the resultant current can be amplified and measured fairly easily.

Both charge carriers move freely through the lattice and are drawn to the detector contacts under the action of the applied bias field to produce a signal

at the gate of a specially designed field effect transistor (FET) mounted directly behind the detector crystal. The transistor forms the input stage of a low-noise charge-sensitive preamplifier located on the detector housing. The output from the preamplifier is fed to the main amplifier, where the signal is finally amplified to a level that can be processed by the analog-to-digital converter (ADC) of the multichannel analyzer (MCA). The schematic diagram of the EDS system is shown in Fig. 5.13 and the experimental set up of EDS attached to FE-SEM (Model: FEI Quanta 200F) procured from FEI Company Oregon USA is shown in Fig. 5.12. The height of the amplifier output pulse is proportional to the input preamplifier pulse, and hence is proportional to the X-ray energy. For the amplifier pulse to be recognized in the ADC, it must exceed the lower level set by a discriminator, which is used to prevent noise pulses from jamming the converter. Once the pulse is accepted, it is used to charge a capacitor that is discharged through a constant current source attached to an address clock typically operating at 50 MHz. The time to discharge the capacitor to 0V is proportional to the pulse amplitude and hence to the X-ray energy. The 50-MHz clock produces a binary number in one of the 1024 channels typically used by the MCA in accordance with the time of the discharge and increments the previously collected number in that channel by 1. By an energy calibration of the channels in the MCA, the collection of X-ray pulses may be displayed on a CRT as an energy histogram.

Detectors are maintained under vacuum at liquid nitrogen temperature to reduce electronic noise and to inhibit diffusion of the lithium when the bias voltage is applied. The gold-coated outer surface is usually further protected by a thin window of beryllium or a polymer. This window is necessary to prevent contaminants from the specimen chamber of the microscope from condensing on the very cold surface of the detector and forming a further barrier to the entry of X-rays. Windowless detectors or detectors with ultra-thin windows of formvar or some other polymer film are now available and

these extend the analytical range down to boron. However such detectors need to be used in microscopes which have extremely good vacuum systems and

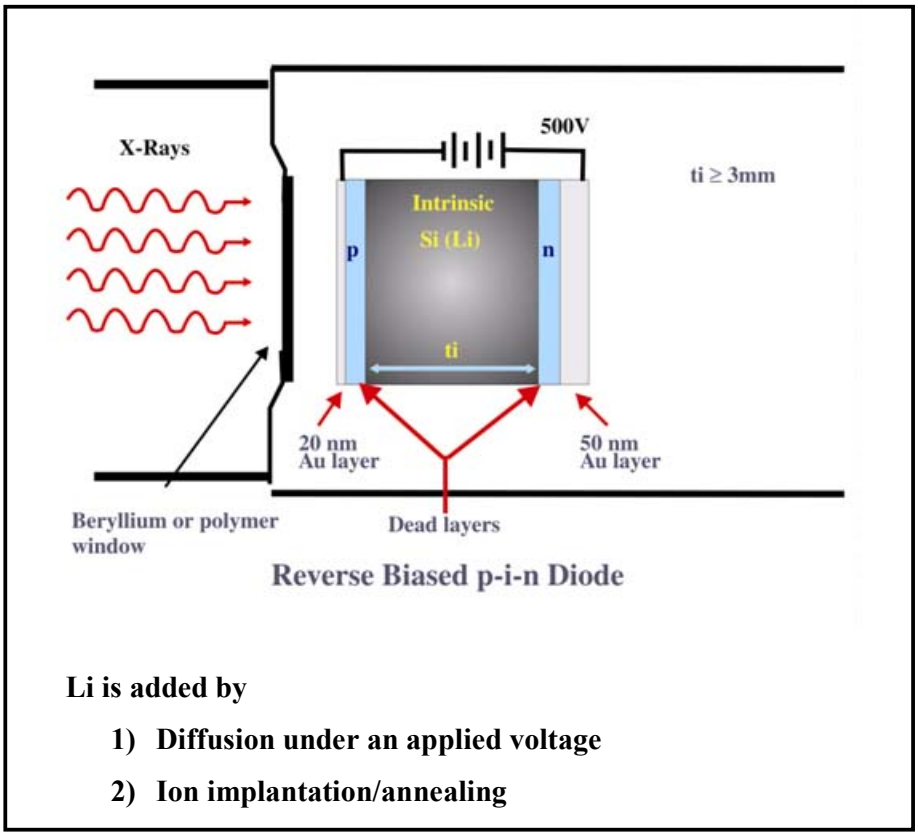

Fig. 5.13 : An energy dispersive Si (II) detector

need very careful protection from accidental air leaks such as those that occur during specimen changes. EDS has been used for quality control and test analysis in many industries including computers, thin films, semiconductors, metals, cement, paper and polymers. It has been used in medicine in the analysis of blood, tissues, bones, and organs, in pollution control, for asbestos identification, in field studies including ore prospecting, archeology, and oceanography, for identification and forgery detection in the fine arts, and for forensic analysis in law enforcement [100].

CHAPTER 6

GRAFTING DATA ANALYSIS AND RESULTS

6.1 INTRODUCTION

Grafting reaction involves the copolymerization of a monomer onto a polymer backbone. The formation of copolymers of various synthetic and natural polymers via graft copolymerization has been extensively studied [101]. Methyl acrylate (MA) and Methyl methacrylate (MMA) have been graft copolymerized with numerous polymeric backbones using various initiating systems. Though there are different number of methods are present to change the surface morphology and roughness parameter of polymer surface, but in the present work, the polymer surface is modified by chemical induced graft copolymerization.

In the present work, an attempt has been made to change the surface morphology of PTFE polymer through grafting of monomer Methyl Methacrylate (MMA) through chemical grafting method. In this work, the effect of monomer concentration, initiator concentrations, effect of temperature of the reaction and time of reaction on grafting were discussed and analyzed.

Teflon (PTFE) surface modification after grafting was studied and verified through FE-SEM. Crystallographic changes were analysed through XRD. Contact angle goniometry applied to measure and analysed the variation of contact angle.

6.2 GRAFTING DATA ANALYSIS

The degree of the grafting was determined from difference in weight of grafted and ungrafted PTFE surfaces [102, 103].

$$[G]\%=\%\ \text{Grafting}=\frac{(W)_g-(W)_o}{(W)_o}\ X\ 100 \qquad \text{Eqn. (6.1)}$$

where $(W)_g$ and $(W)_o$ are the weights of the grafted and un-grafted samples, respectively. The weight of grafter polymer was consider after the complete removal of the homopolymer/copolymer. Percentage of grafting has been determined as a function of total dose, amount of water and concentration of monomer. It is also dependent on the temperature and concentration of initiator.

6.2.1 Percentage Grafting as a Function of Various Parameters at Constant Temperature (50^{o}C)

(Initiator concentration, Monomer concentration, Time)

At constant temperature of 50^0C, to determine the optimum condition of maximum yield of grafting is determined by varying BPO concentration, Grafting Time, monomer concentration one by one keeping other parameters remains constant.

Table 6.1 gives the data of % grafting varying with initiator concentration, monomer concentration and grafting time at constant temperature of 50^{o}C. The effect of the initiator BPO concentration on grafting rate was studied. These results are shown in Fig. 6.1(a).

It was observed that the grafting increases up to a certain level and reaches a maximum value of 9.77% at a concentration of 0.03 M of the initiator, beyond which it decreases slowly. In a grafting point of view, the initial increase is due to the availability of the free radicals generated for grafting of the monomer. When the concentration of the initiator exceeds a certain value,

increased free radical concentration results in serious copolymerization and hence lowers the graft copolymerization.

Fig. 6.1 (b) represents the effect of monomer (MMA) concentration on the percentage of grafting on PTFE film. It can be seen that the grafting percentage increases initially with increasing monomer concentration and then decreases on further increasing the concentration of MMA. The initial increase in grafting may be due to the reason that most of the monomers are utilized by the available free radical sites on the PTFE backbone. However, it can be noted that the grafting rate does not exceed 8-9% at a monomer concentration of 10 (%V/V). Also at higher concentrations, the degree of copolymerization increases and the grafting percentage decreases. Moreover at the lower concentration, the extent of copolymerization of the monomer is smaller. The grafting reaches a maximum value and thereafter decreases. This is because the number of free radical sites available on the PTFE backbone becomes a limiting factor and the rate of diffusion is progressively affected by deposition on the polymer backbone

From Fig. 6.1 (c) it has been observed that grafting level increases initially with reaction time. The graft copolymerization rate increases to a maximum value of 120 minute. With an increase in reaction time, the free radicals have more time for reaction and therefore results in higher level of grafting.

After certain time, all the initiator and monomer are used up. Thus, no further change in grafting level was observed with increasing reaction time. The decrease in grafting may be due to the induced decomposition of the initiator leading to decrease in the concentration of the initiator and hence decrease in active radicals required to generate active sites on polymeric back bone.

From Fig. 6.1 it is clear that maximum yield of grafting is obtained when [BPO] = 0.03 M, [Monomer] = 10% V/V, [Time] = 120 Sec at constant temperature of 50°C.

Table 6.1 : Variation of % grafting with BPO Concentration, Time, and Monomer Concentration at constant Temperature of 50^0C

150 µm Teflon 2cm x 2cm						
Temperature	50°C		50°C		50°C	
Time	120 Min		NA		120 Min	
Monomer Concentration	10%V/V		10%V/V		NA	
Initiator Concentration	NA		0.03 M		0.03 M	
S.No	Initiator	Grafting	Time	Grafting	Monomer	Grafting
	M	%	Min.	%	%V/V	%
1	0.01	3.66	90	3.98	5	3.66
2	0.03	9.04	120	9.03	10	9.17
3	0.05	8.19	150	7.06	15	8.43
4	0.07	4.3	180	3.2	20	5.9

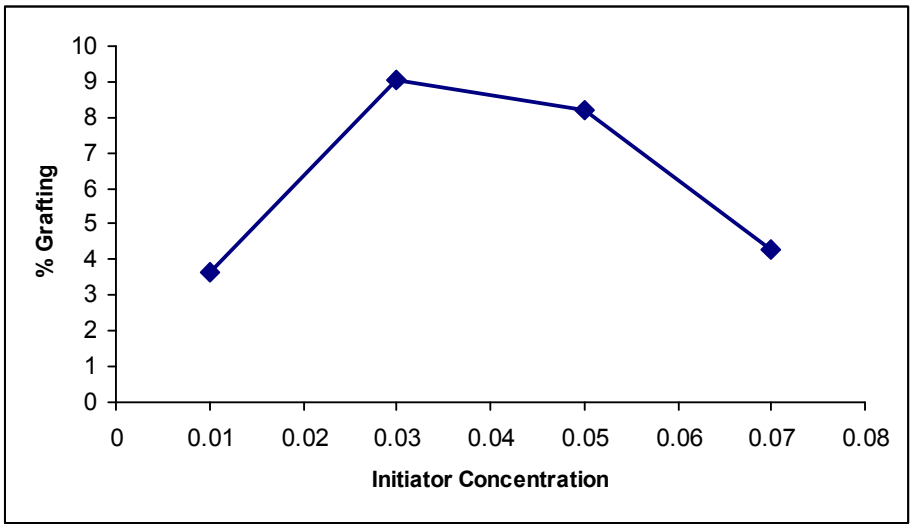

Fig. 6.1 (a) : Variation of % grafting with initiator BPO concentration

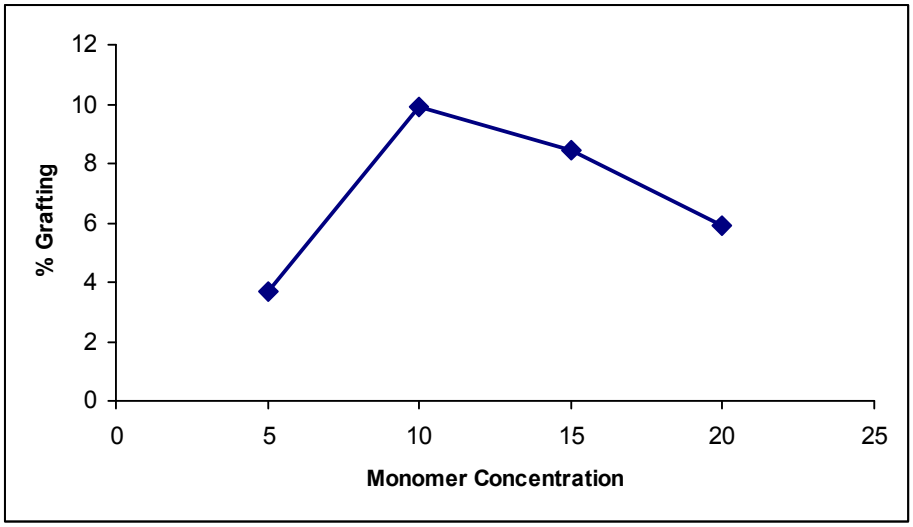

Fig. 6.1 (b) : Variation of % grafting with monomer concentration

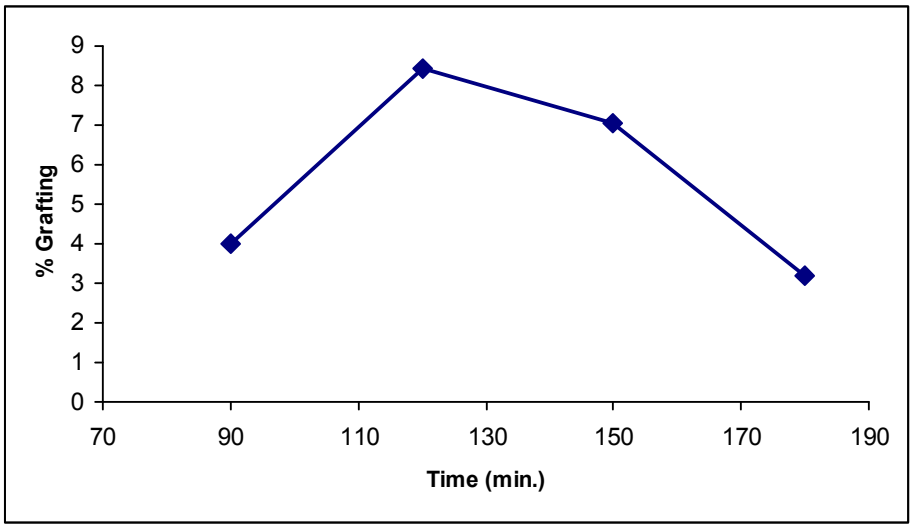

Fig. 6.1 (c) : Variation of % grafting with grafting time

6.2.2 Percentage Grafting as a Function of Temperature

The temperature of grafting medium is one of the most important reaction parameters that hase a strong effect on the grafting yield This experiment was performed at different temperature 40, 50, 60 and 70 °C with an accuracy of ± 2°C for two hours with monomer concentration of 10% and BPO 0.03M After the grafting reaction, the samples were taken out from the monomer solution and washed with acetone to remove the remaining homopolymer [104,105]. The washed samples were again weighed to know about any changes in weight due to grafting process depicted in Table 6.2.

S.No	Sample	Temperature	Weight of Pristine		% Grafting
	PTFE		Before Grafting	After Grafting	
	(150 Micro Meter)				
	(2cm X 2cm)	(Degree Celsius)	(Gram)	(Gram)	
1	PTFE	40	0.132	0.137	3.75
2	PTFE	50	0.133	0.146	9.77
3	PTFE	60	0.131	0.142	8.39
4	PTFE	70	0.132	0.139	5.3

Table 6.2 : Variation of % Grafting with Temperature

[Constant Parameter] : [Monomer] = 10% V/V, BPO] = 0.03, [Time] = 2h

The increase in temperature of the grafting mixture up to 50°C initially increases the degree of grafting as shown in Fig. 6.2(a) and Fig. 6.2(b). This may be due to the increase of the initiation and propagation rates of graft copolymerization. Increased in the degree of grafting with increasing temperature is also due to increase in the decomposition of the initiator leading to the formation of more free radicals and the generation of active sites on the polymeric backbone. But beyond 50 °C, the grafting rate decreases and the film becomes brittle. This is because at higher temperature, higher combination rates of monomer are obtained increasing homo polymerization reactions, which results in a decreased grafting rate.

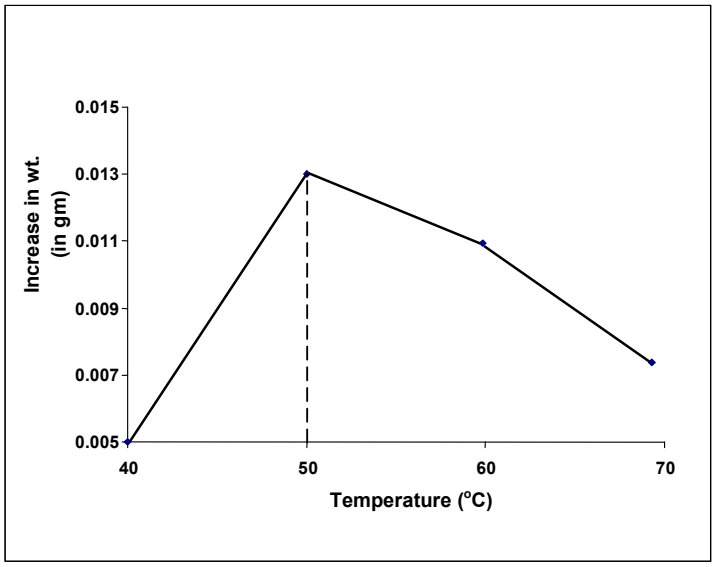

Fig. 6.2 (a) : Variation of weight of grafted polymer with temperature at monomer concentration 10% V/V

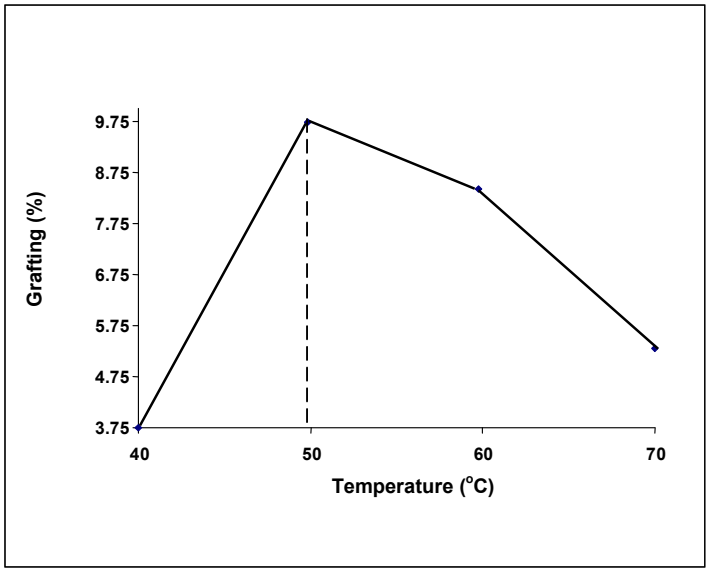

Fig. 6.2 (b) Variation of % grafting with temperature at monomer concentration 10% V/V

(c)

The increase in temperature of the grafting mixture up to 50°C initially increases the degree of grafting as shown in Fig. 6.2(a). This may be due to the increase of the initiation and propagation rates of graft copolymerization. Increased in the degree of grafting with increasing temperature is also due to increase in the decomposition of the initiator leading to the formation of more free radicals and the generation of active sites on the polymeric backbone. But beyond 50°C, the grafting rate decreases and the film became brittle. This is because at higher temperature, higher combination rates of monomer are obtained increasing homo polymerization reactions, which results in a decreased grafting rate. Fig. 6.2(b) represents the variation of weight of grafted polymer with temperature keeping other parameters remains constant.

Fig 6.3(a) represents the Variation of grafting with temperature at 15% V/V monomer concentration. Rest of the parameters remains constant through out the experiment. The data obtained is shown in Table 6.3.

Table 6.3 : Variation of % Grafting with Temperature

S.No	Sample	Temperature	Weight of Pristine		% Grafting
	PTFE		Before Grafting	After Grafting	
	(150 Micro Meter)				
	(2cm X 2cm)	(Degree Celsius)	(Gram)	(Gram)	
1	PTFE	40	0.132	0.134	1.51
2	PTFE	50	0.133	0.140	5.263
3	PTFE	60	0.132	0.138	4.54
4	PTFE	70	0.131	0.136	3.817

[Constant Parameter] : [Monomer] = 15% V/V, BPO] = 0.03, [Time] = 2h

It can be seen that the grafting percentage increases initially with an increase in temperature at higher monomer concentration and then decreases on further increase in temeperature but the value % grafting is less in comparison to 10% V/V monomer concentration Fig. 6.3(b).

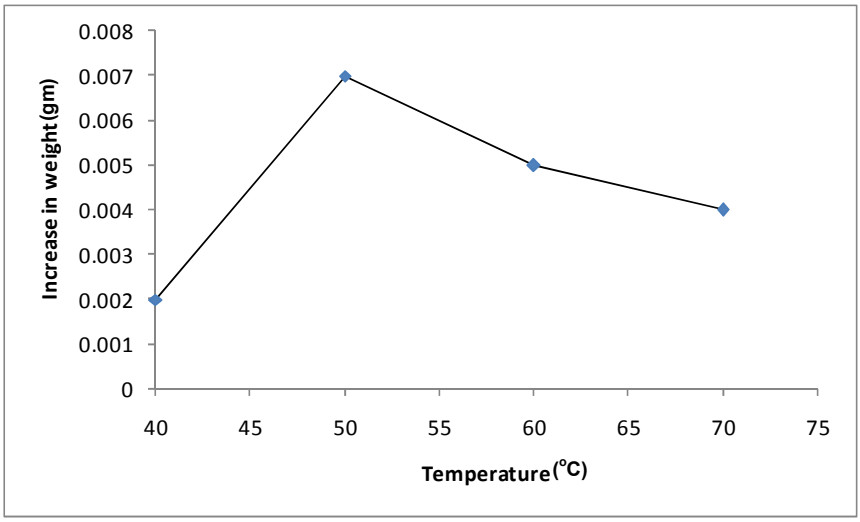

Fig. 6.3 (a) : Variation of weight of grafted polymer with temperature at monomer concentration 15% V/V

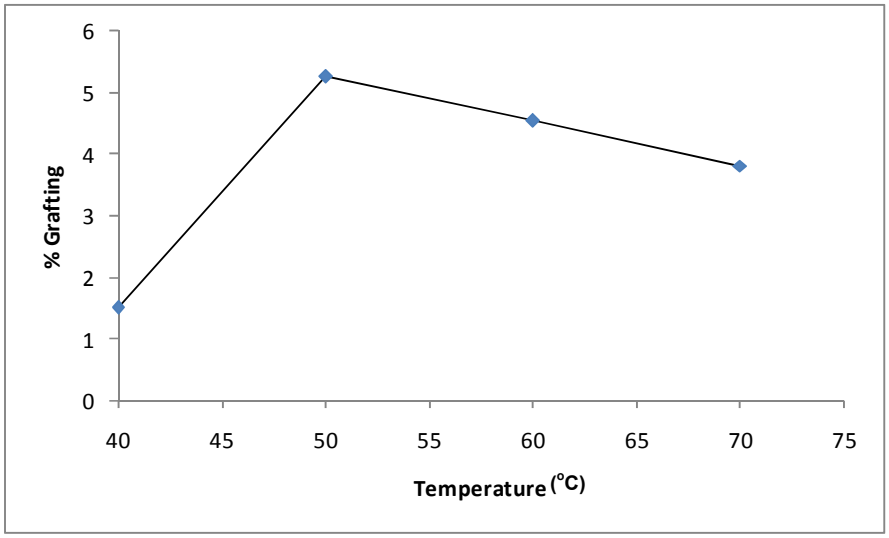

Fig. 6.3 (b) : Variation of % Grafting with temperature at monomer concentration 15% V/V

The initial increase in grafting may be due to the reason that most of the monomer is utilized by the available free radical sites on the PTFE backbone. Also at higher concentrations, the degree of homopolymerization increases and the grafting percentage decreases. Moreover at the lower concentration, the extent of homopolymerization of the monomer is smaller. The grafting reaches a maximum value and thereafter decreases.

The temperature of grafting medium is one of the most important reaction parameters that has a strong effect on the grafting. The change in weight I after grafting at temperature 40^0C is negligible which shows that at 40^0C, initiator could not create active site to graft the monomers. When the temperature was kept at 50^0C, it was found that weight of grafted polymer became very high. This shows that at this temperature, large number of active sites were created and MMA were successfully grafted. Increase in the degree of grafting with increasing temperature is also due to increase in the decomposition of the initiator leading to the formation of more free radicals and the generation of active sites on the polymeric backbone. Further increase in temperature 60^0C, 70^0C results in decrease grafting rate. The reason of this might be attributed to decrease in number of active sites and formation of oligomer of MMA.

6.3 SURFACE MORPHOLOGICAL ANALYSIS OF GRAFTED PTFE BY FE-SEM

The change in morphology of PTFE surface after modification by surface-initiated free radical polymerization studied by FE-SEM. FE-SEM images of PTFE (Pure) and PTFE-g-MMA at magnification (X 50000) and resolution of 1.5 nm have been taken by FEI QUANTA 200F instrument at Institute instrumentation Centre, IITR. Fig. 6.4 and Fig. 6.5 are the images of grafted and ungrafted PTFE.

The electron beam, which typically has an energy 10 KeV, is focused by one or two condenser lenses into a beam with a very fine focal spot size (≈ 5 nm). The basic mechanism of field emission is that a high voltage applied between a pointed cathode and a plate anode causing the current to flow [106]. The field emission tip is generally made of a single crystal tungsten wire sharpened by electrolytic etching. A tip diameter of ≈100 Å is used, with the apparent source size much less than that. The field emission process itself depends on the work function of the metal, which can be affected by adsorbed of gases. The composition of the grafted PTFE with that of pristine PTFE shows clearly the change in the topography of the PTFE surface. The virgin PTFE exhibits a smooth surface pattern whereas the grafted PTFE (PTFE-g-MMA) exhibits rough surface. The reason for the surface roughness is due to the grafting of MMA onto PTFE which opens up its matrix and shows considerable deposition of MMA on the surface of back bone polymer. Fig. 6.4(a) and Fig. 6.5(a) represents the SEM image of pure pristine. Fig. 6.4(b), (c) and (d) and Fig. 6.5(b), (c) and (d) represents the image of grafted PTFE at 50°C, 60°C and 70°C with resolution of 5 μm and 10 μm.

The maximum irregularity and non-uniformity without cracking is observed in Fig. 6.4(b) and 6.5(b). These are the images grafted at 50^{o}C with resolution of 5 μm and 10 μm.

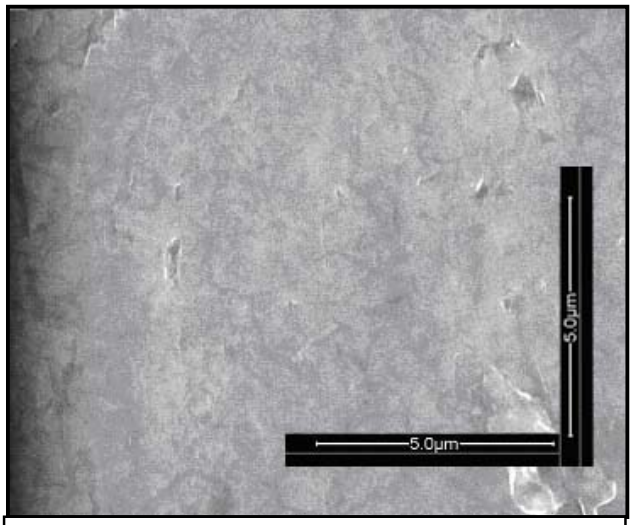

FE-SEM IMAGE PTFE (150 µm) Teflon

HV	Mag	WD	Det	HFW
12.kV	10000x	9.5mm	LFD	14.92µm

Grafting at : NA

Fig. 6.4 (a) FE-SEM image of ungrafted (Pristine) PTFE

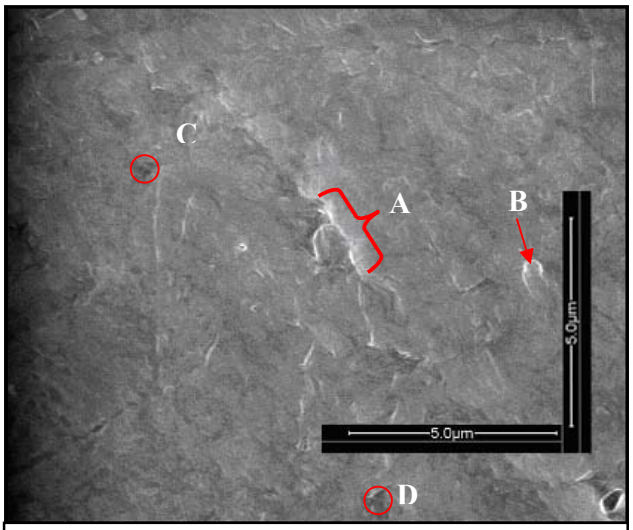

FE-SEM IMAGE PTFE (150 µm) Teflon

HV	Mag	WD	Det	HFW
12.5kV	10000x	9.7 mm	LFD	14.92µm

Grafting at : [Monomer]=10% V/V, [BPO] = 0.03M,
[Time] = 2hr, [Temperature] = 50°C

Fig. 6.4 (b): FE-SEM Image of grafted PTFE at 50°C (at 5µm)

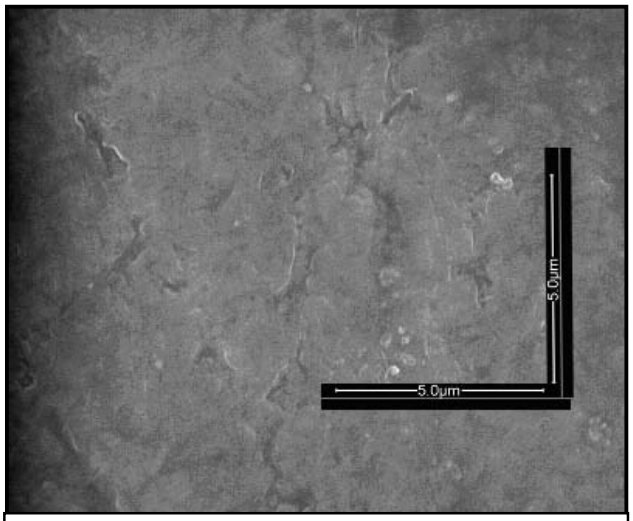

FE-SEM IMAGE PTFE (150 µm) Teflon

HV	Mag	WD	Det	HFW
12.5kV	10000x	9.7 mm	LFD	14.92µm

Grafting at : [Monomer]=10% V/V, [BPO] = 0.03M, [Time] = 2hr, [Temperature] = 60°C

Fig. 6.4 (c) : FE-SEM Image of grafted PTFE at 60°C (at 5µm)

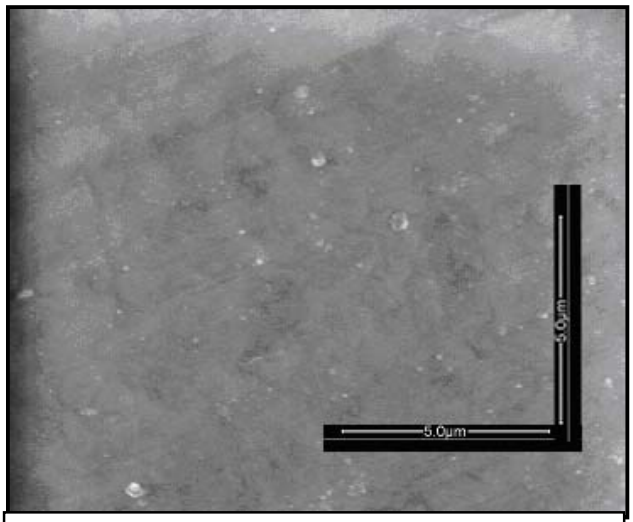

FE-SEM IMAGE PTFE (150 µm) Teflon

HV	Mag	WD	Det	HFW
12.5kV	10000x	9.6 mm	LFD	14.92µm

Grafting at : [Monomer]=10% V/V, [BPO] = 0.03M, [Time] = 2hr, [Temperature] = 70°C

Fig. 6.4 (d) : FE-SEM Image of grafted PTFE at 70°C (at 5µm)

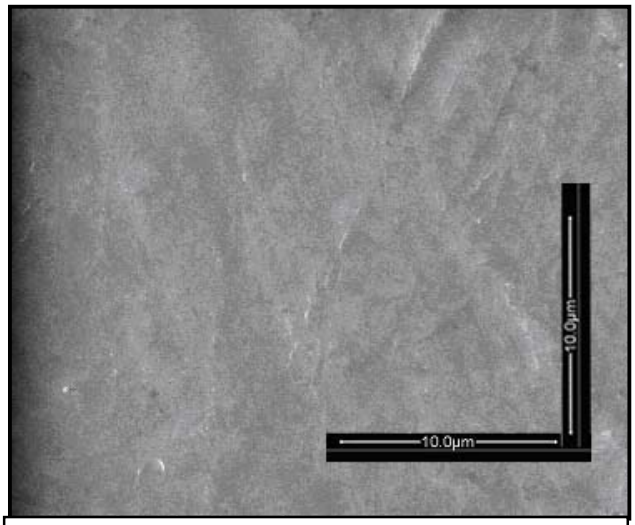

FE-SEM IMAGE PTFE (150 µm) Teflon

HV	Mag	WD	Det	HFW
12.5kV	5000x	9.5 mm	LFD	29.84µm

Grafting at : NA

Fig. 6.5 (a) : FE-SEM Image of Pristine (PTFE) (at 10µm)

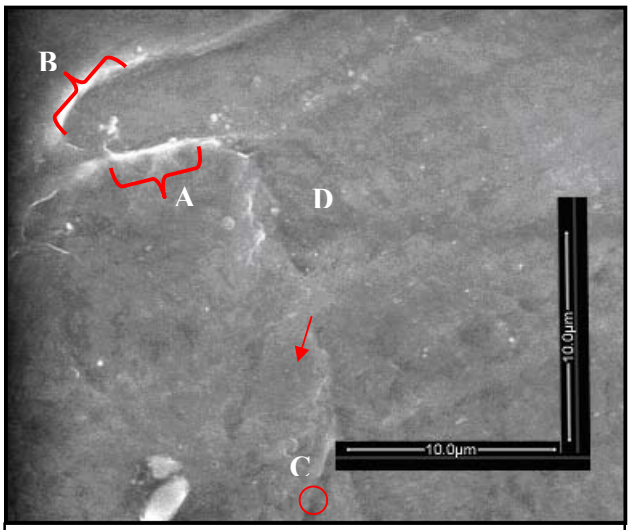

FE-SEM IMAGE PTFE (150 µm) Teflon

HV	Mag	WD	Det	HFW
12.5kV	5000x	9.6 mm	LFD	29.84 µm

Grafting at : [Monomer]=10% V/V, [BPO] = 0.03M, [Time] = 2hr, [Temperature] = 50°C

Fig. 6.5 (b) : FE-SEM Image of grafted PTFE at 50°C (at 10µm)

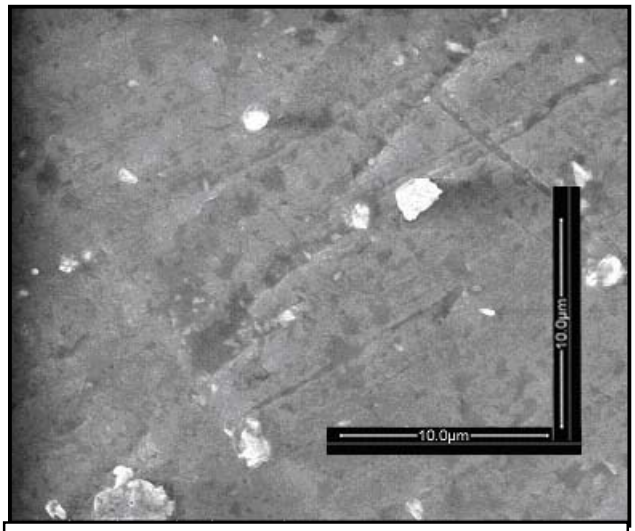

FE-SEM IMAGE PTFE (150 µm) Teflon

HV	Mag	WD	Det	HFW
12.5kV	5000x	9.7 mm	LFD	29.84 µm

Grafting at : [Monomer]=10% V/V, [BPO] = 0.03M, [Time] = 2hr, [Temperature] = 60°C

Fig. 6.5 (c) : FE-SEM Image of grafted PTFE at 60°C (at 10µm)

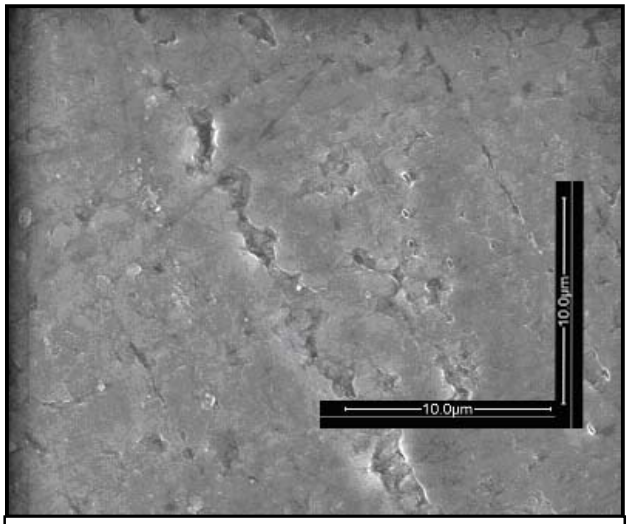

FE-SEM IMAGE PTFE (150 µm) Teflon

HV	Mag	WD	Det	HFW
12.5kV	5000x	9.7 mm	LFD	29.84 µm

Grafting at : [Monomer]=10% V/V, [BPO] = 0.03M, [Time] = 2hr, [Temperature] = 70°C

Fig. 6.5 (d) : FE-SEM Image of grafted PTFE at 70°C (at 10µm)

Following conclusion can be drawn from analysis

1) The result suggested that the surface initiated free radical polymerization has given rise to non-uniform molecular weight distribution and the dense coverage of MMA on PTFE surface.

2) Fig. 6.4(a) and Fig. 6.5(a) is the FE-SEM images of pure pristine at resolution of 5μm and 10μm respectively. The change in image is the impact of change in instrument resolution only. We studied the grafting impact on polymer PTFE surface with respect to FESEM images

3) The bumps in form of white patches is appear in FE-SEM image of grafted PTFE at 50°C depicted in Fig. 6.4(b). Points A and B in Fig. 6.4 (b) represent section of white patch. The height at this section of image is not similar to ungrafted surface. This white spot section in grafted image is nearly more than 30-40% of the total surface area clearly indicates the increase in the roughness of the surface. Approximately similar result is depicted in Fig. 6.5(b) which is taken at resolution of 10 μm.

4) In similar fashion, the deep dugs in the form of dark black spots also appear in images. Points C and D in Fig. 6.4(b) represents these duggy spots which are little dark in colour show the non uniform structure of surface and hence depict the increase in the roughness of the surface.

5) It is also clear from Fig. 6.4(c) and (d) that the uniformity in image is reduced at higher temperature with decrease in number of white patches indicate that the grafting % is less at higher temperature hence change in roughness parameter of surface is also less.Similar result is obtained when we consider the data at resolution of 10μm.

6.4 XRD ANALYSIS OF GRAFTED POLYMER

X-ray diffraction patterns were recorded using the Cu-Kα (1.54 A) radiation with 8.04 KeV energy from Burker D8 Advance X -ray spectrometer at Institute Instrumentation Centre,(IIT Roorkee, India). A rotating anode source and a Sodium Iodine scintillation detector have been used. The value of the diffraction angle (2θ) ranged from 3^0 to 90^0 with a step size 0.04 mm.The measurements were done at room temperature and ambient pressure conditions. Each experiment was repeated at least twice and with both faces of the specimens alternatively exposed to the incident X-rays to check the reproducibility [107]

The radiation (Cu-K_α) emanating from the X-ray tube is diffracted at the specimen and recorded by a detector. The specimen is rotated at constant angular speed in such a way so that angle of incidence of primary beam changes [108], while detector moves about the specimen at twice the angular speed. The diffraction angle (2θ) is thus always equal to double the glancing angle (θ).

Whenever the Bragg condition, $2d\sin\theta = n\lambda$, is satisfied, the incident X-ray beam is diffracted at the specimen and reaches the detector. The detector converts the X-ray quanta into electron pulses, which are recorded by recorder. Bruker D8 Advance diffractometer uses NaI scintillation counter as a detector. It can detect the diffracted radiations in the wavelength ranging from 0.5 to 3 Å.

Fig. 6.6 **(b)** shows the XRD data of 150 μm thick grafted polymer PTFE thin film with maximum number of counts .The un-grafted PTFE is shown in Fig 6.6(a) pristine (Grafted under optimum condition). The absence of crystalline peaks corresponding to PTFE indicates the change in amorphous nature of PTFE. The height of the peak in Fig. 6.6(c) and 6.6(d) reduces which indicate that minor change in orientation of the planes of PTFE when grafted at 60^0C and 70^0C grafting temperature.

Monochromator is used to suppress the undesired portions of radiation. To restrict the irradiated specimen area, aperture diaphragm is arranged between the tube and the specimen.

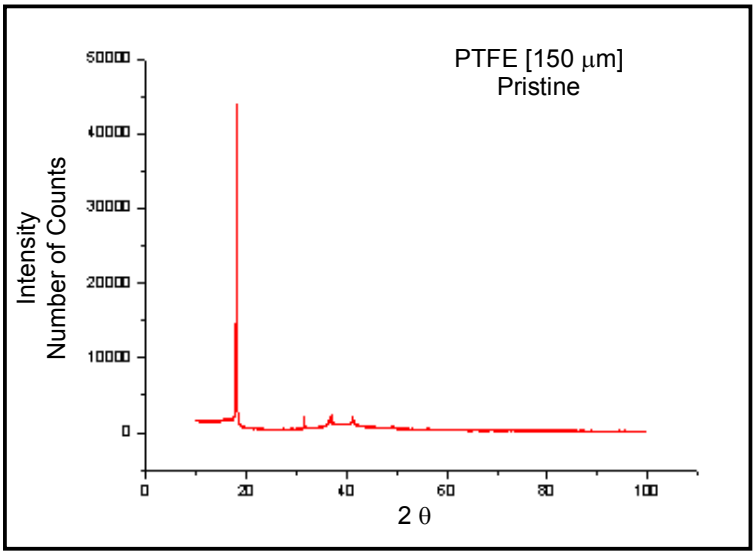

Fig. 6.6 (a) : XRD image of Pristine (ungrafted) PTFE

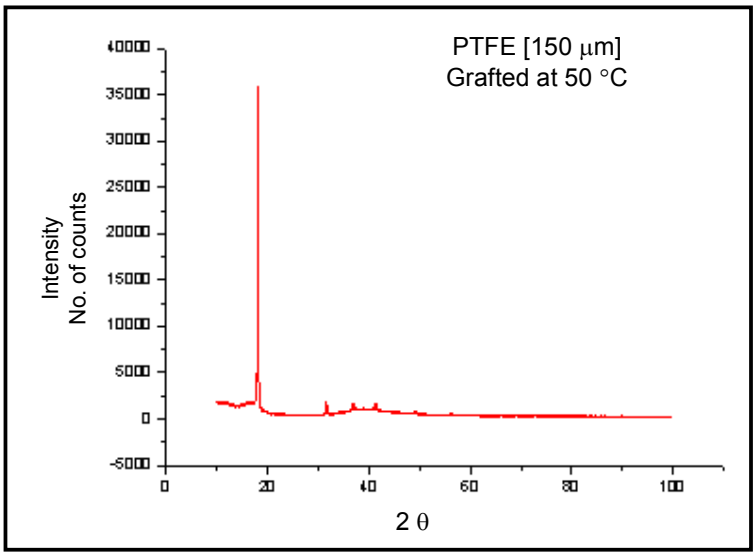

Fig. 6.6 (b) : XRD image of grafted PTFE (with grafting temperature 50^{o}C)

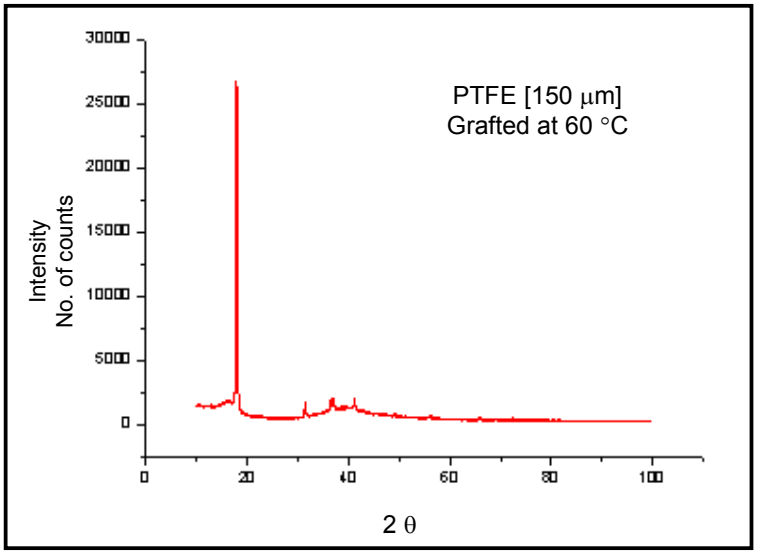

Fig. 6.6 (c) : XRD image of grafted PTFE (with grafting temperature 60°C)

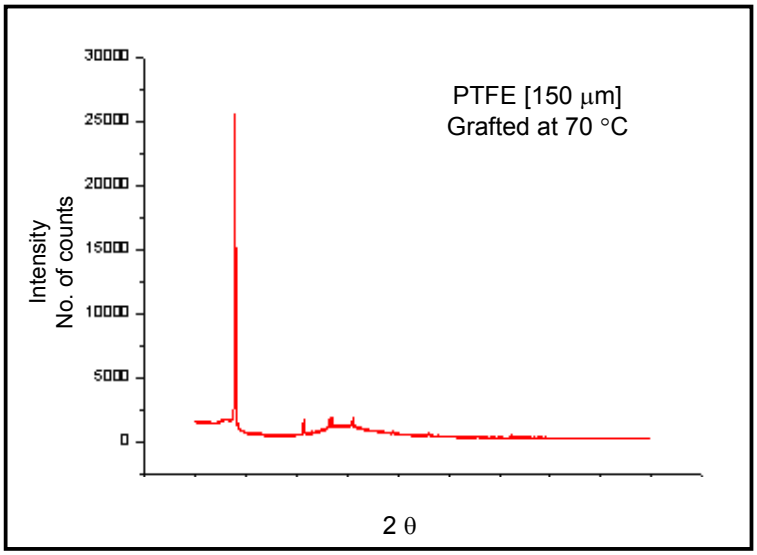

Fig. 6.6 (d) : XRD image of grafted PTFE (with grafting temperature 70°C)

6.5 CONTACT ANGLE GONIOMETRY

The contact angle system called Easy Drop-standard from KRUSS, Germany with pre-installed Drop Shape Analysis Software DSA-1 was used at Institute Instrumentation Centre, Indian Institute of Technology (IIT), Roorkee. The Pre-Installed DSA-1 Software is to determine static contact angles using sessile drop method, to control camera, illumination, temperature, dosing modules, table movements, to measure, store and report measured contact angle values. The manual sample table moves the sample to the right position. Single dosing system deposits the drop onto the grafted polymer surface by microsyring [109]. At equilibrium, the camera records the digital image and allows the perfect drop shape analysis The contact angle can be calculated and protocolled by Drop Shape Analysis Software i.e. DSA-1 Software

The liquid used in syringe to determine the contact angle for oleophobic properties of PTFE film is CH_3I. The syringe will handle drop volumes of 3µl of $CH_3I$with 0.1 µl resolution. Once the position of the syringe is adjusted according to the sample, the drop formed at the tip of the needle is lowered slowly and forms the contact angle when it strikes the surface of the sample. Drop images are acquired using a camera and in line incident illuminator software controlled optical halogen lamp. The action appears live on the computer screen and the salient images are captured to the computer's memory for later image analysis [110]. The camera can capture images at very fast rate of around 25-60 frames per second. The measurement location on the platform can be shifted to facilitate formation of another drop on the same surface. So the drop profile is photographed, the evaluation of the drop image takes place in the window of the software: the baseline is determined automatically for measuring the contact angle and the tangent of the sessile drop profile at the three-phase contact point drawn onto the image is used to determine the value of the contact angle of liquid CH_3I on PTFE surface by the DSA-1 software.

The data in Table 6.4 represent the measure of contact angle of grafted PTFE surface at various temperatures keeping other parameter like concentration of monomer , reaction time, initiator concentration remains constant. Fig. 6.7 is the plot of contact angle values with respect to various temperature .

Table 6.4 : Contact Angle of Grafted PTFE at Various Grafting Temperature

PTFE (Grafted)	Temperature(°C)	Pristine	40 °C	50°C	60°C	70°C
	Contact Angle(θ)°	90.4	92.8	95.55	93.3	93

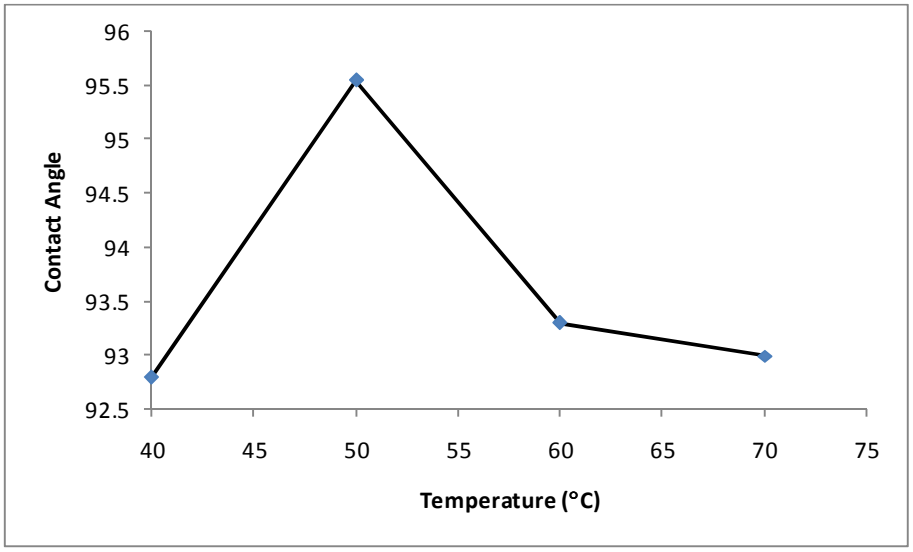

Fig. 6.7 : Variation of contact angle with grafting temperature

Following observation were drawn from the Fig. 6.7.

(1) The peak in the graph is existing at 50°C indicates that the value of the contact angle increases from 40°C to 50°C and its maximum value i.e. 95.5°C is existing when PTFE is grafted at 50°C.

(2) After and before of this grafted temperature50°C the value of contact angle decreases and minimum value exist at the 70°C.

(3) The Rate of increment of contact angle vale is approximately similar to the rate of decrement of contact angle value.

The contact angle goniometer is used to check wettability of liquid on solid surface. Lower the contact angle greater the wettability. It is used as a relative measure of surface energy. The primary parameter that characterize wetting is the static contact angle, which is defined as the measurable angle which the liquid makes with solid.

Grafting is not only responsible for increase the roughness of PTFE polymer sample but also responsible for decrease the wettability of surface. Maximum grafting is existing at 50°C .This result is in full compliance with FESEM and XRD data.

6.6 CONCLUSION

(1) The optimum conditions for grafting is achieved when polymerization was carried at the following condition.
[MMA] =10% V/V; [BPO] = 0.03M; [Temperature] = 50°C; [Time]=2 hr.

(2) The percentage of grafting is not only increasing with temperature but also depends upon monomer concentration, initiator and grafting time.

(3) Surface morphological analysis through FE-SEM suggested that the roughness of the grafted PTFE is changed.

(4) Contact angle goniometry concludes that contact angle is a function of grafted temperature hence % of monomer grafted.

Chapter 7

SURFACE ANALYSIS OF ION IRRADIATED GRAFTED TEFLON

7.1 INTRODUCTION

Oil-repellent surface has been explored due to its self cleaning character. The multi-functional coating on a grafted polymer surface is the current field of research. For obtaining oil-repellent surface, it is necessary to prepare the surface with very small surface tension. These surfaces can be obtained by uniformly applying fluoromethyl (–CF3) groups on them [110–114]. Thus, the fluorinated compounds usually remain the most common active ingredients for oil-repellent purpose. The basic effect of surface structure on super water repellency has been well known since the initial publications of Wenzel [115] and Cassie and Baxter [116] model. Both the models have laid emphasis on the geometrical structure of solid surfaces as an important factor in determining the wettability. Preparation of super water-repellent surface has been investigated by several publications in the past [117–119]. Starting from Onda *et al.* [120–121] have reported a serial achievement that demonstrated the contact angle of water droplets on low energy surface increases strongly with growing surface roughness and porosity.

The irradiation of grafted PTFE through low energy (approx. 3 KeV) Ar^+ ion beam is not only responsible to change the surface morphology but also increase the possibility of change in elemental composition. The roughness of the surface is the prime parameter to study the oleophobic nature of Teflon surface. The contact angle is quantifiable measurement of roughness of surfaces.

This chapter deals with change in surface morphology of polymer after the irradiation. The data related to the contact angle is also discussed in this chapter. The analysis of data related to the contact angle is also the core part of this chapter.

7.2. SURFACE MORPHOLOGY OF TREATED PTFE BY FE-SEM

Field Emission Electron Microscope (FEI Quanta 200F model) with resolution of 2nm and possible magnification 500000 X to study the surface morphology of the grafted PTFE film was used. FE-SEM analysis provide qualitative analysis of the surface morphology at various magnification FESEM uses field emission electron gun which provides improved special resolution down to 1.5 nm that is 3 to 6 times better than conventional SEM and minimizes sample charging and damage. The electron beam, which typically has an energy ranging from a few hundred eV to 50 KeV, is focused by two condenser lenses into a beam with a very fine focal spot size of (1 to 5 nm). The basic mechanism of field emission is that a high voltage applied between a pointed cathode and a plate anode causing the current to flow. The field emission tip is generally made of a single crystal tungsten wire sharpened by electrolytic etching. A tip diameter of 100 to 1000 Å is used, with the apparent source size much less than that. The field emission process itself depends on the work function of the metal, which can be affected by adsorbed gases and due to this very high vacuum is required [122]. The contrast in an SEM image reveals information about the surface morphology and composition of the material.

Comparative analysis and to study the optimum roughness condition, two sets of irradiated sample of PTFE was considered (i) irradiated with beam time of 10 sec (ii) irradiated with beam time of 100 sec. For each set, four images at various grafting temperature i.e. 40,50, 60 and 70°C are considered. Set of Fig. 7.1 shows the FE-SEM images of irradiated PTFE sample with beam time of 10 sec with various grafting temperature i.e. 50, 60 and 70°C (other conditions remain constant) Fig. 7.2 is for same set but beam time in these set of figure is 100 sec. Set of Fig. 7.1 and Fig. 7.2 is considered at 5μm resolution while set of Fig. 7.3 and 7.4 is considered at 10μm resolution.

Following conclusions are drawn from these sets of figures :

Fig. 7.1 (a) SEM observation showed that the surface of pristine PTFE has low but uniform roughness without sharp edges. The surface edges which rarely observe any non uniform valleys. The surface is more or less uniform and smooth. The dark spots indicate a little irregularity in the height of sample at that particular portion of pristine surface

Fig. 7.1(b) FE-SEM observation of PTFE sample irradiated for 10 Sec and grafted at 50°C. Mild bumps are observed with Shallow irregularities on the surface. The peak to valley height does not exceed 0.5mm. Approximately equal portion of dark and mild spots are present. It indicates that due to irradiation the surface roughness increases. Light crack is also observed at one portion of the image.

Fig. 7.1 (c) and (d)FE SEM observational image of PTFE sample irradiated for 10sec and grafted at 60^{o}C and 70^{o}C. Deep dark line observed at the surface indicates the possibility of surface cracking and irregularity. Dugs is also observed in the image shown with arrows .There is the possibility of surface distortion.

Approximately similar observation is observed in second set of figure. Fig. 7.2(b) shows the maximum roughness as portion of dark and mild spots is almost equal and at higher temperature the crack is developed hence it is of no use.

Optimum suitable surface is observed at 50^{0}C.Similarly in Fig. 7.3(a) and 7.4(a), the extremely mild irregularity in the surface is present. The surface is more or less uniform and smooth. These are the images of pure pristine teflon.

Fig. 7.3(b) and 7.4(b) show mild bumps with shallow irregularities on the surface. Maximum roughness is observed in these figures without cracks. These figures are treated PTFE surfaces grafted at 50^{o}C with ion irradiation beam time of 10 and 100 sec respectively at resolution of 10μm. Fig. 7.3(c) and 7.3(d) show irregularities but with cracks, hence, they are not suitable for our work.

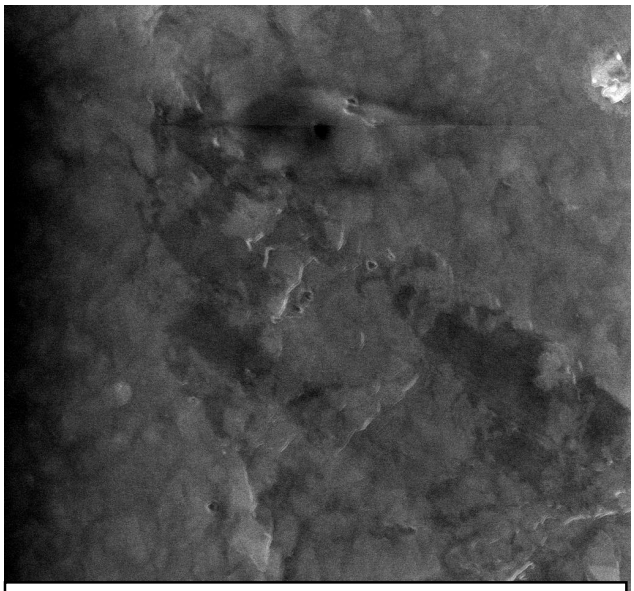

FE-SEM IMAGE PTFE (150 μm) Teflon

HV	Mag	WD	Det	HFW
10.kV	10000x	9.9mm	LFD	14.92μm

Grafting at : NA
Beam Time : NA

Fig. 7.1 (a) : FE-SEM image of pristine PTFE.

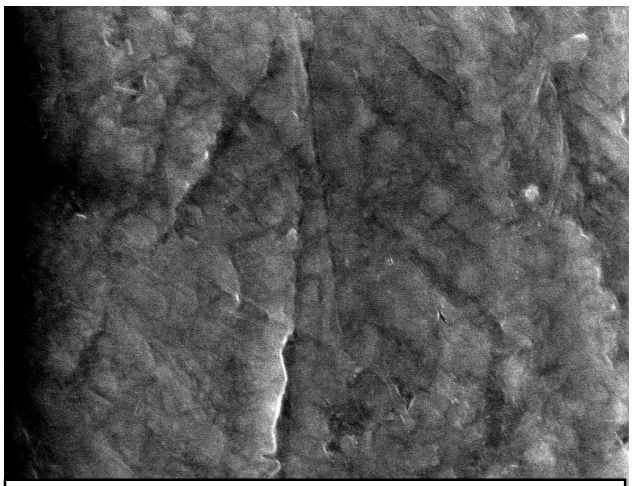

FE-SEM IMAGE PTFE (150 μm) Teflon

HV	Mag	WD	Det	HFW
10.kV	10000x	9.9mm	LFD	14.92μm

Grafting at :[Monomer]=10% V/V, [BPO] = 0.03M,
[Time] = 2hr, [Temperature] = 50°C
Beam Time : 10 sec

Fig. 7.1 (b) : FE-SEM image of treated PTFE (10 sec) with grafting temperature 50^{o}C

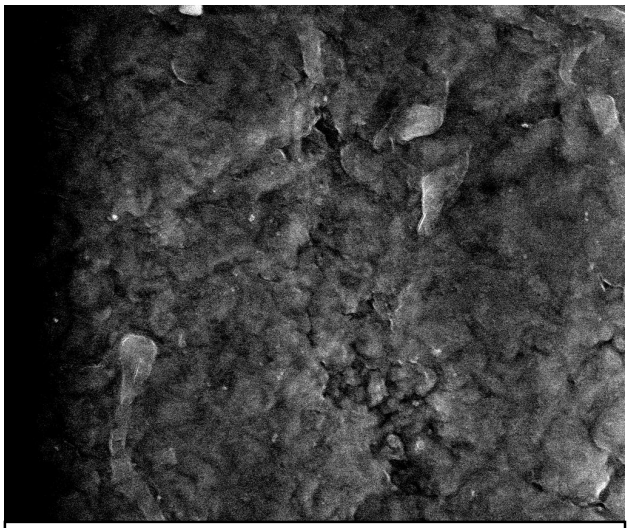

FE-SEM IMAGE PTFE (150 μm) Teflon

HV	Mag	WD	Det	HFW
10.kV	10000x	9.9mm	LFD	14.92μm

Grafting at :[Monomer]=10% V/V, [BPO] = 0.03M,
[Time] = 2hr, [Temperature] = 60°C
Beam Time : 10 sec

Fig. 7.1 (c) : FE-SEM image of treated PTFE (10 sec) with grafting temperature 60°C

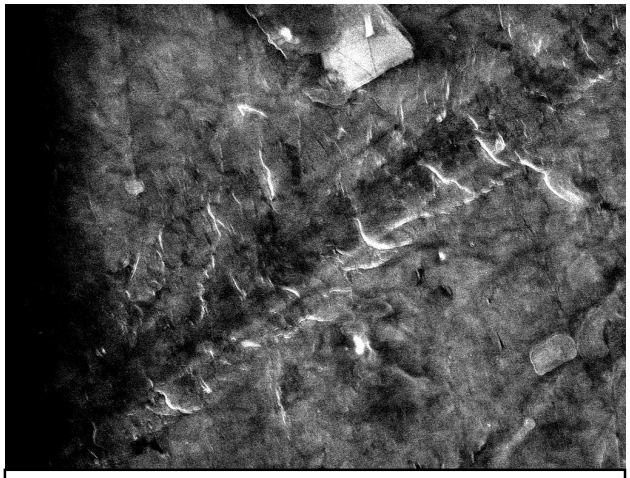

FE-SEM IMAGE PTFE (150 μm) Teflon

HV	Mag	WD	Det	HFW
10.kV	10000x	9.9mm	LFD	14.92μm

Grafting at :[Monomer]=10% V/V, [BPO] = 0.03M,
[Time] = 2hr, [Temperature] = 70°C
Beam Time : 10 sec

Fig. 7.1 (d) : FE-SEM image of treated PTFE (10 sec) with grafting temperature 70°C

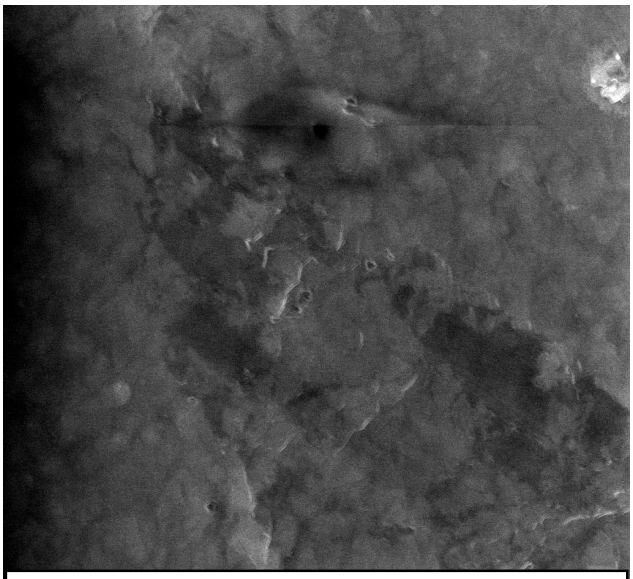

FE-SEM IMAGE PTFE (150 μm) Teflon

HV	Mag	WD	Det	HFW
10.kV	10000x	9.9mm	LFD	14.92μm

Grafting at : NA
Beam Time : NA

Fig. 7.2 (a) : FE-SEM image of Pristine PTFE

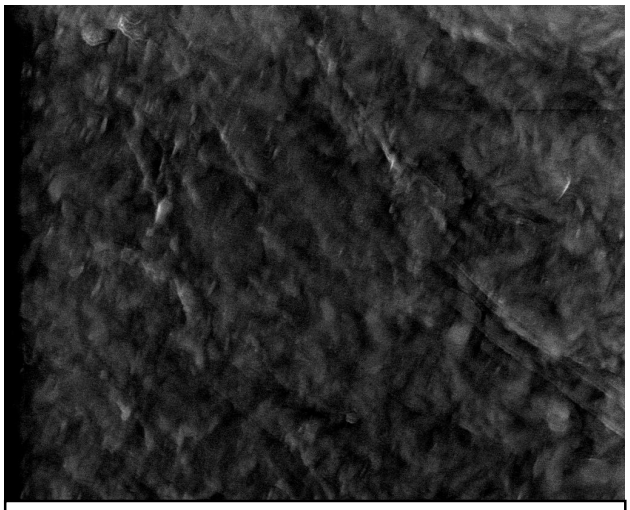

FE-SEM IMAGE PTFE (150 μm) Teflon

HV	Mag	WD	Det	HFW
10.kV	10000x	9.9mm	LFD	14.92μm

Grafting at :[Monomer]=10% V/V, [BPO] = 0.03M,
[Time] = 2hr, [Temperature] = 50°C
Beam Time : 100 sec

Fig. 7.2 (b) : FE-SEM image of treated PTFE (100 sec) with grafting temperature 50°C

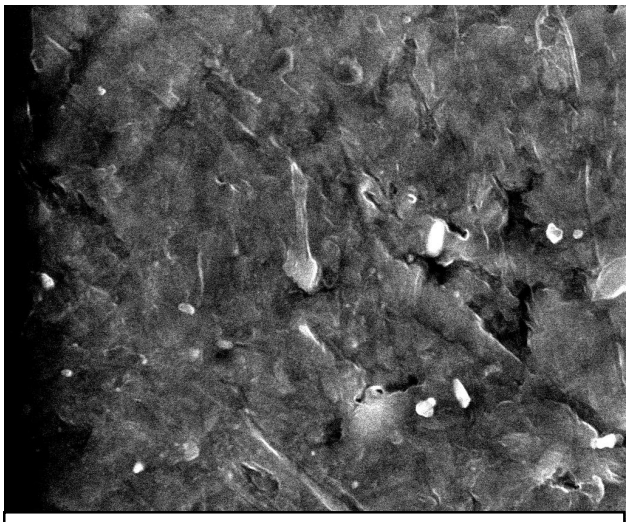

FE-SEM IMAGE PTFE (150 μm) Teflon

HV	Mag	WD	Det	HFW
10.kV	10000x	9.9mm	LFD	14.92μm

Grafting at :[Monomer]=10% V/V, [BPO] = 0.03M,
[Time] = 2hr, [Temperature] = 60°C
Beam Time : 100 sec

Fig. 7.2 (c) : FE-SEM image of treated PTFE (100 sec) with grafting temperature 60°C

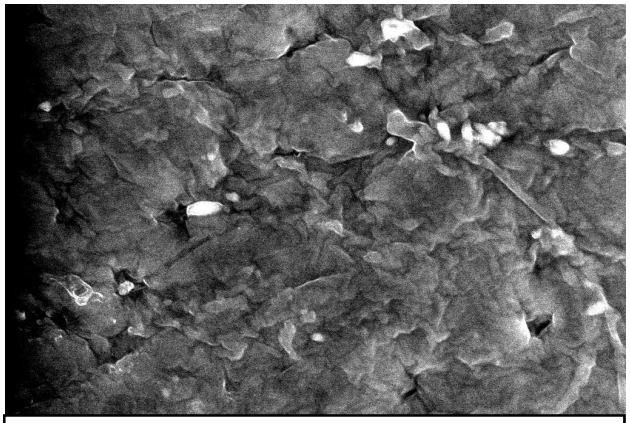

FE-SEM IMAGE PTFE (150 μm) Teflon

HV	Mag	WD	Det	HFW
10.kV	10000x	9.9mm	LFD	14.92μm

Grafting at :[Monomer]=10% V/V, [BPO] = 0.03M,
[Time] = 2hr, [Temperature] = 70°C
Beam Time : 100 sec

Fig. 7.2 (d) : FE-SEM image of treated PTFE (100 sec) with grafting temperature 70°C

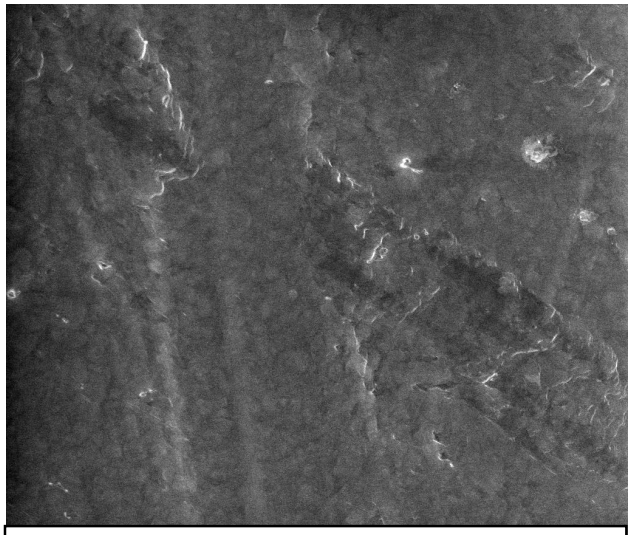

FE-SEM IMAGE PTFE (150 μm) Teflon

HV	Mag	WD	Det	HFW
10.kV	5000x	9.9mm	LFD	29.84μm

Grafting at : NA
Beam Time : NA

Fig. 7.3 (a) : FE-SEM image of Pristine PTFE with resolution 10μm

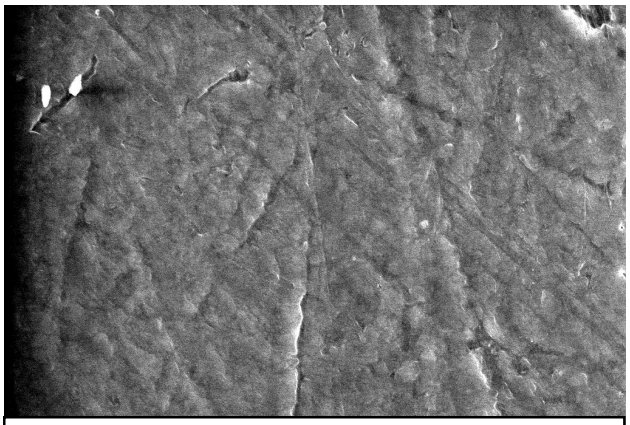

FE-SEM IMAGE PTFE (150 μm) Teflon

HV	Mag	WD	Det	HFW
10.kV	5000x	9.9mm	LFD	29.84μm

Grafting at :[Monomer]=10% V/V, [BPO] = 0.03M,
[Time] = 2hr, [Temperature] = 50°C
Beam Time : 10 sec

Fig. 7.3 (b) : FE-SEM image of treated PTFE (10 sec) with grafting temperature 50^{o}C (Resolution 10μm)

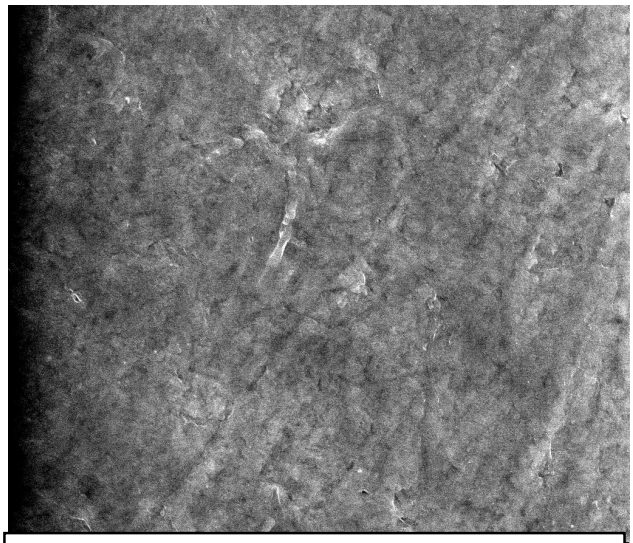

FE-SEM IMAGE PTFE (150 μm) Teflon

HV	Mag	WD	Det	HFW
10.kV	5000x	9.9mm	LFD	29.84μm

Grafting at :[Monomer]=10% V/V, [BPO] = 0.03M,
[Time] = 2hr, [Temperature] = 60°C
Beam Time : 10 sec

Fig. 7.3 (c) : FE-SEM image of treated PTFE (10 sec) with grafting temperature 60°C (at 10μm)

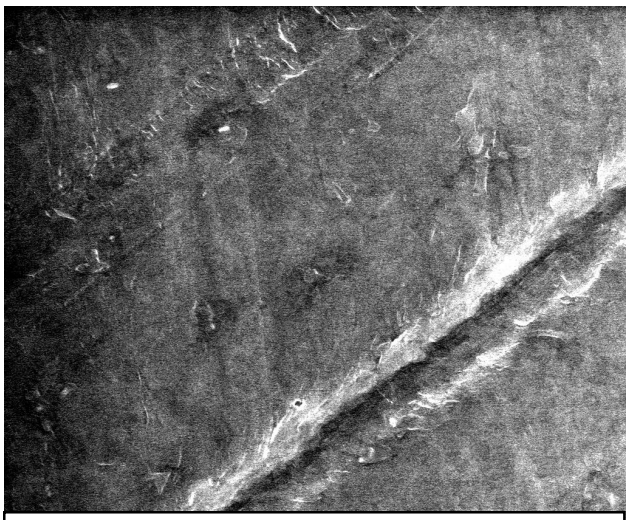

FE-SEM IMAGE PTFE (150 μm) Teflon

HV	Mag	WD	Det	HFW
10.kV	5000x	9.9mm	LFD	29.84μm

Grafting at :[Monomer]=10% V/V, [BPO] = 0.03M,
[Time] = 2hr, [Temperature] = 70°C
Beam Time : 10 sec

Fig. 7.3 (d) : FE-SEM image of treated PTFE (10 sec) with grafting temperature 70°C (at 10μm)

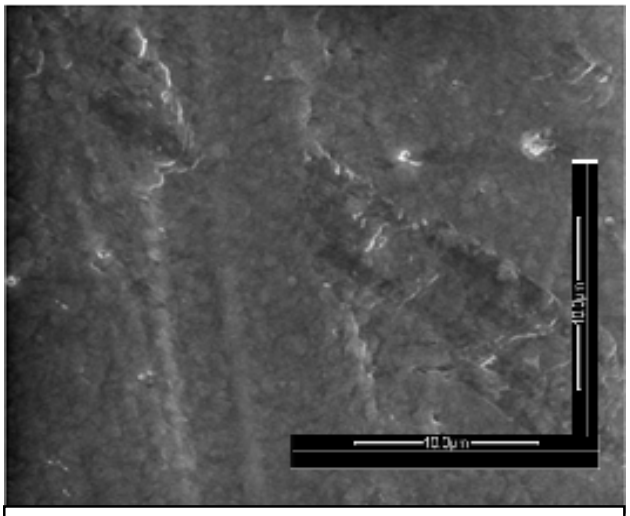

FE-SEM IMAGE PTFE (150 μm) Teflon

HV	Mag	WD	Det	HFW
10.kV	5000x	9.9mm	LFD	29.84μm

Grafting at :NA
Beam Time : NA

Fig. 7.4 (a) : FE-SEM image of Pristine PTFE

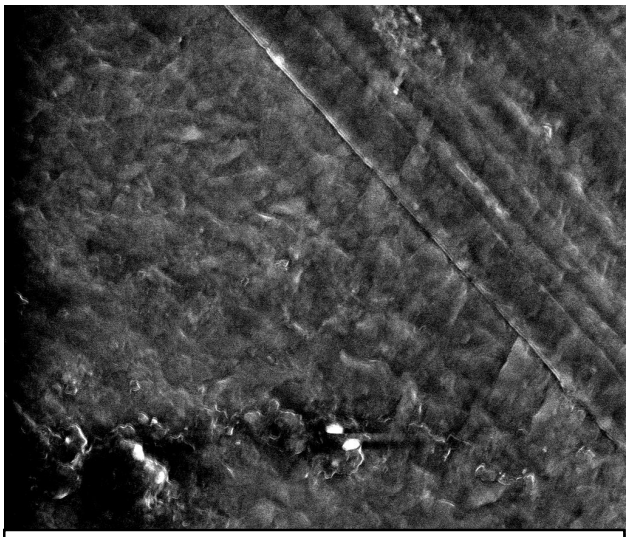

FE-SEM IMAGE PTFE (150 μm) Teflon

HV	Mag	WD	Det	HFW
10.kV	5000x	9.9mm	LFD	29.84μm

Grafting at :50^{O}C
Beam Time : 100 sec

Fig. 7.4 (b) : FE-SEM image of treated PTFE (100 sec) with grafting temperature 50^{o}C (at 10μm)

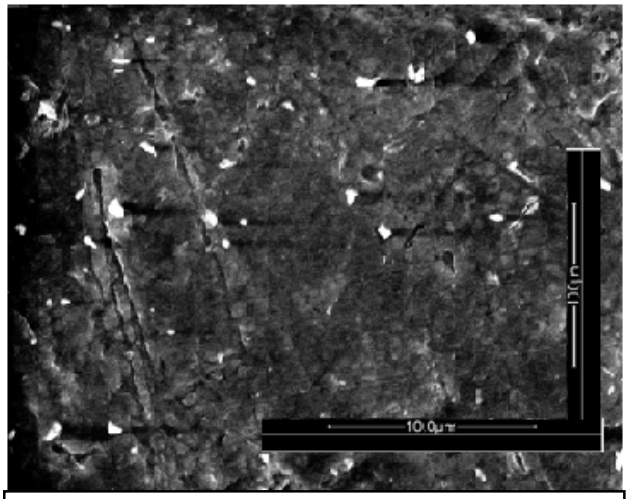

FE-SEM IMAGE PTFE (150 μm) Teflon

HV	Mag	WD	Det	HFW
10.kV	5000x	9.9mm	LFD	29.84μm

Grafting at : 60^{O}C
Beam Time : 100 sec

Fig. 7.4 (c) : FE-SEM image of treated PTFE (100 sec) with grafting temperature 60^{o}C (at 10μm)

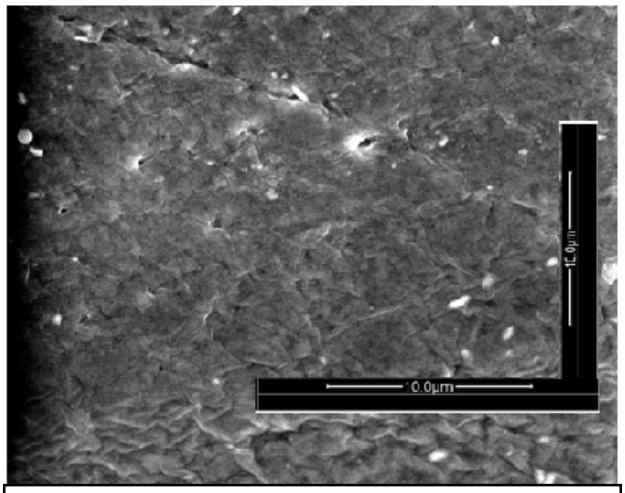

FE-SEM IMAGE PTFE (150 μm) Teflon

HV	Mag	WD	Det	HFW
10.kV	5000x	9.9mm	LFD	29.84μm

Grafting at :70^{O}C
Beam Time : 100 sec

Fig. 7.4 (d) : FE-SEM image of treated PTFE (100 sec) with grafting temperature 70^{o}C

FE-SEM analysis of the irradiated (for 10 sec.) shows that smoothness of the samples decreases when compared with that of the pristine . With increase in grafting temperature, it was observed that as temperature goes beyond 50^0C the sample surface is deformed which is evident from the micro –size cracks in the samples. No such kind of micro cracks were observed in the samples grafted at 50^0C except the decrease in smoothness. As increasing the irradiation time by 100 seconds, several micro-sized pits were observed on the sample surface for all grafting temperature.

7.3 ELEMENTAL ANALYSIS OF LOW ENERGY Ar+ ION TREATED PTFE

Using the energy dispersive x-ray analysis (EDS) attachment with the SEM, elemental composition analysis can be done. An EDS spectrum displays peaks corresponding to the energy levels for which the most X-rays had been received. Each of these peaks is unique to an atom, and therefore corresponds to a single element. The higher a peak in a spectrum, the more concentrated the element is in the specimen. Interaction of an electron beam with a sample target produces a variety of emissions, including X-rays. An Energy-Dispersive X-Ray Spectroscopy (EDS) detector is used to separate the characteristic X-rays of different elements into an energy spectrum. EDS system software is used to analyze the energy spectrum in order to determine the abundance of specific elements.

X-ray spectrometers with X-ray tube generators as sources and Si(Li) detectors have been used for X-ray diffraction (XRD).With a radioactive source, an EDS system is easily portable and can be used in the field more easily than most other spectroscopy techniques. With a minimum detection limit (MDL) of 100-200 ppm for most elements, an EDS system is capable of detecting less than a monolayer of metal film on a substrate using Kα lines at moderate accelerating voltages of 5-15KeV.

The experimental set up of EDS is attached to FE-SEM (Model: FEI Quanta 200F) procured from FEI Company Oregon USA at IIC (IIT, Roorkee). The height of the amplifier output pulse is proportional to the input preamplifier pulse, and hence is proportional to the X-ray energy.

Detectors are maintained under vacuum at liquid nitrogen temperature to reduce electronic noise and to inhibit diffusion of the lithium when the bias voltage is applied. The gold-coated outer surface is usually further protected by a thin window of beryllium or a polymer. Fig. 7.5 and 7.6 represents the output of EDS system. The peaks C(K) F(K) and O(K) are almost same in each figure. The individual weight % is also depicted in each diagram.

There was no change in the composition of the element found via EDS analysis. This clearly shows that the ion beam which is used to increase the oleophobicity of the grafted Teflon has only imparted the energy to decrease the smoothness of the sample. The ion has not got embedded in the sample.

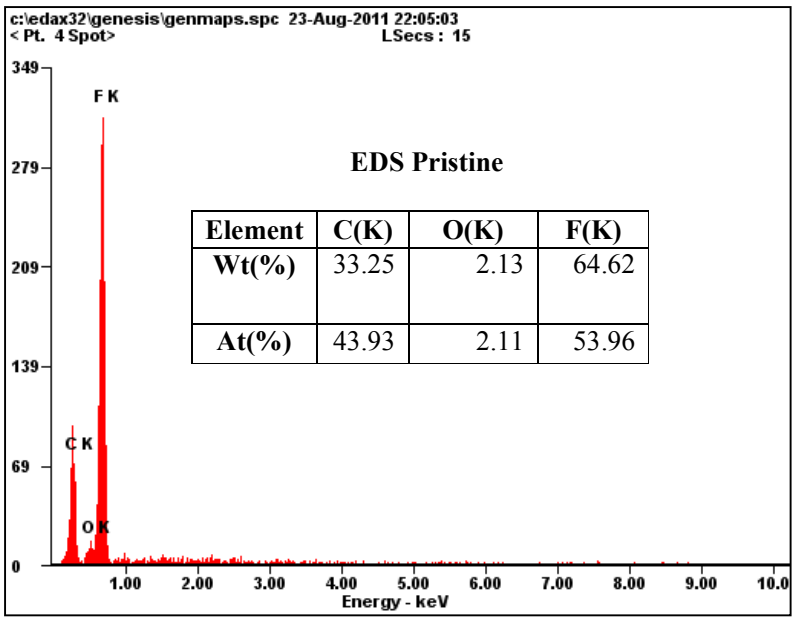

Fig. 7.5 (a) : Energy Dispersive Spectrum of Pristine PTFE

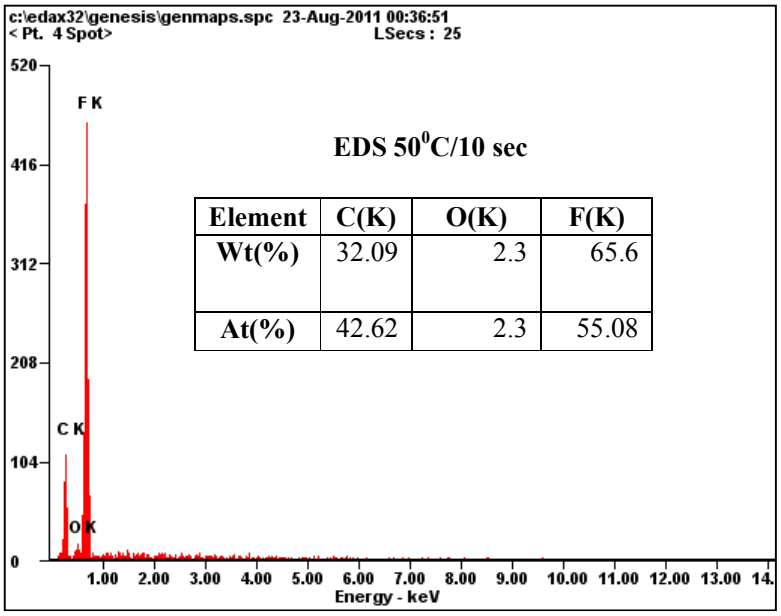

Fig. 7.5 (b) : Energy Dispersive Spectrum of treated PTFE (Beam Time= 10 sec) with grafting temperature 50°C

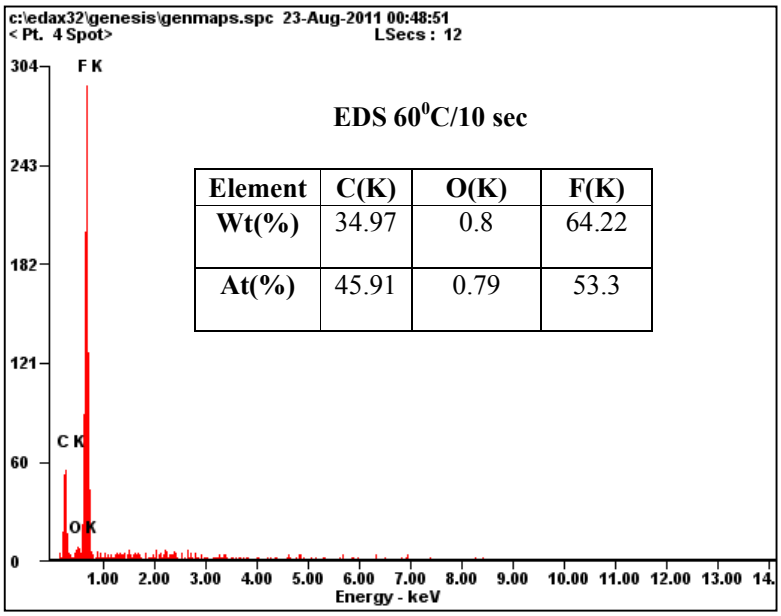

Fig. 7.5 (c) : Energy Dispersive Spectrum of treated PTFE (Beam Time 10 sec) with grafting temperature 60°C

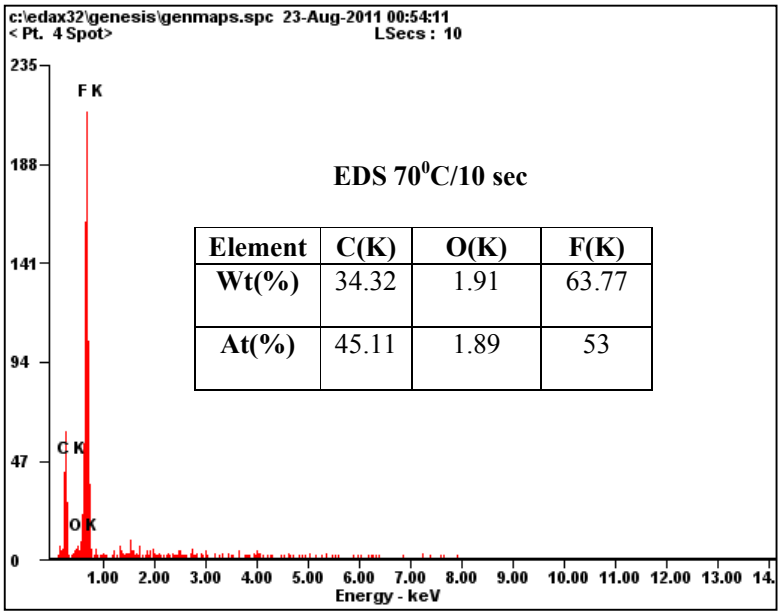

EDS 70^{0}C/10 sec

Element	C(K)	O(K)	F(K)
Wt(%)	34.32	1.91	63.77
At(%)	45.11	1.89	53

Fig. 7.5 (d) : Energy Dispersive Spectrum of treated PTFE (Beam Time =10 sec) with grafting temperature 70^{o}C

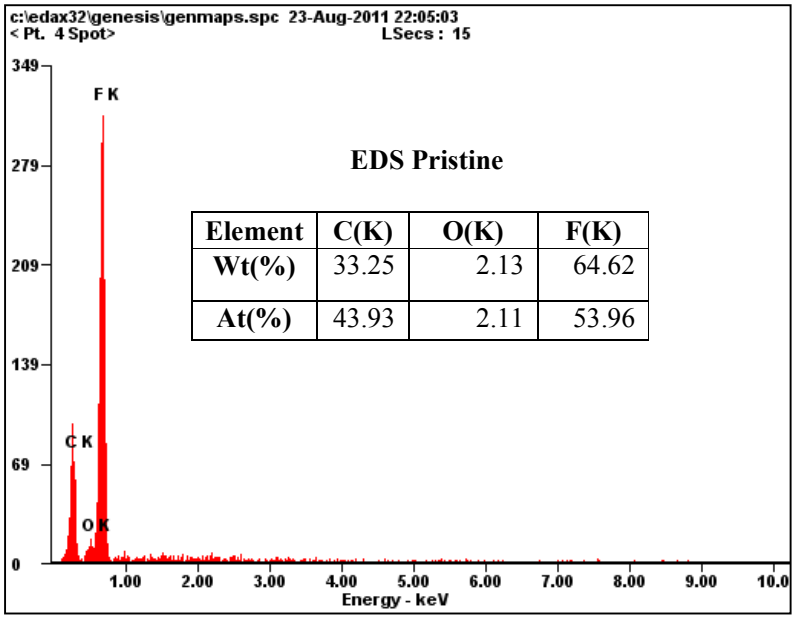

EDS Pristine

Element	C(K)	O(K)	F(K)
Wt(%)	33.25	2.13	64.62
At(%)	43.93	2.11	53.96

Fig. 7.6 (a) : Energy Dispersive Spectrum of Pristine PTFE

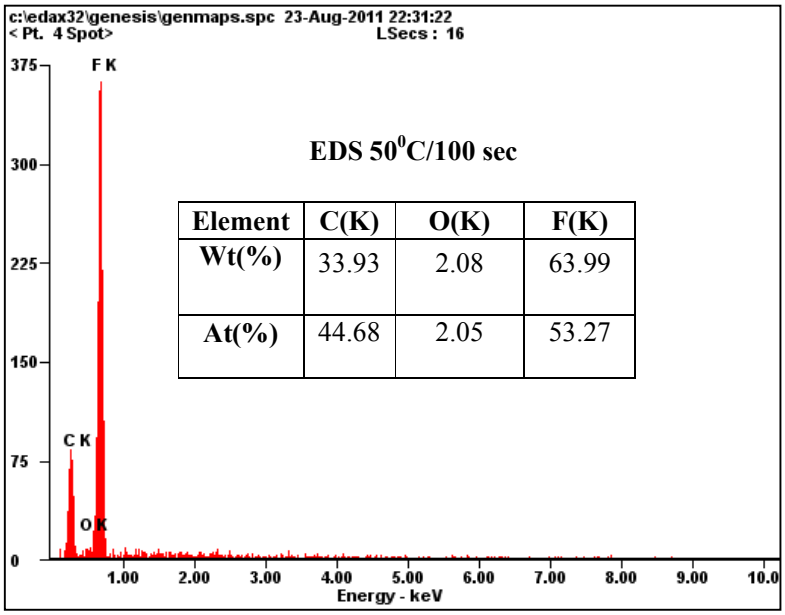

Fig. 7.6 (b) : Energy Dispersive Spectrum of treated PTFE (Beam Time=100 sec) with grafting temperature 50°C

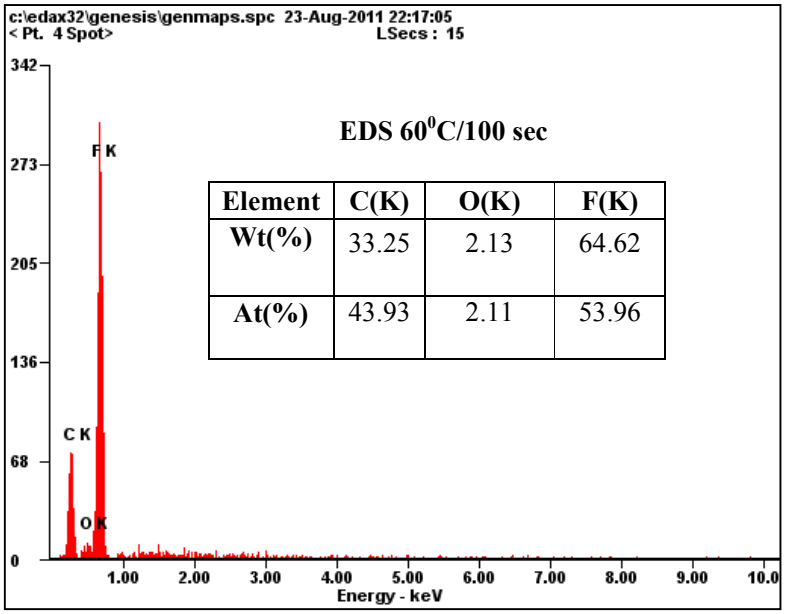

Fig. 7.6 (c) : Energy Dispersive Spectrum of treated PTFE (Beam Time=100 sec) with grafting temperature 60°C

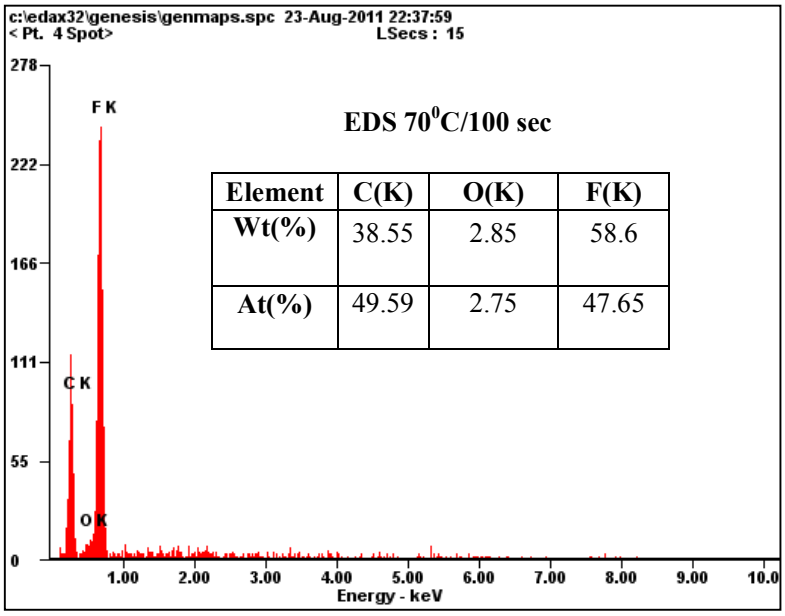

Fig. 7.6 (d) : Energy Dispersive Spectrum of treated PTFE (Beam Time=100 sec) with grafting temperature 70°C

7.4 IRRADIATED PTFE SURFACE ANALYSIS THROUGH CONTACT ANGLE GONIOMETRY

Grafted Polymer treatment was performed with the ISE 10 ion gun using 3 KeV Ar+ ions and a defocused ion beam with ion fluence of 10^{16} cm^{-2}. After treatment, the samples had to be removed from the vacuum chamber as the contact angle measurements were performed in air. The two sets of four samples of PTFE with different grafting temperatures (i.e. 50°C, 60°C, 70°C and Pristine) were prepared for ion fluence (≈ $10^{16}cm^{-2}$) For first of sample beam time is 10 sec while for other set of samples beam time is 100 sec. The average contact angle was taken as an angle for particular ion fluence. The contact angles θ were calculated by the program using the Young-Laplace function . The software allows to take photographic images of the drop which will be shown in Images.

Static contact angle of methylene iodide CH_3I with treated polymer surface in order to analyze the changes generate in 2 cm x 2 cm (150 μm) grafted PTFE after irradiated through low energy (3 MeV) Ar+ ion beam is determined by

contact angle goniometry**.** The sets of Fig. 7.4 and Fig. 7.5 show images of oil drops on untreated and Ar+ treated PTFE. Dotted lines in the images indicate the interface between liquid and the polymer surface. The Lubricant CH_3I is used to measure contact angle on treated and untreated PTFE. The Oil drop on untreated PTFE is of the form of a bead with the angle $\theta < 90°$ i.e. $\theta \approx 86.4°$ Fig. 7.4 (a). With increasing temperature, the liquid spreads on the treated surface, showing that the oliophilic PTFE surface becomes oliophobic, when the polymer is irradiated with ions. For the contact angle measurements, the contact angle system called " Easy Drop Standard" from KRUSS, Germany with pre-installed Drop Shape Analysis Software DSA-1 was used at Institute Instrumentation Centre, Indian Institute of Technology (IIT), Roorkee. The Pre-Installed DSA-1 Software is to determine static contact angles using sessile drop method, to control camera, illumination, temperature, dosing modules, table movements, to measure, store and report measured contact angle values. The manual sample table moves the sample to the right position. Single dosing system deposits the drop onto the treated polymer surface by microsyring.

Contact angle measurements were done using air as medium. The treated polymers were removed from vacuum and reacted with atmospheric O_2. During these reactions oxygen containing functional groups were formed thatinfluenced the experimental measurements.

Table 7.1 : Variation of contact angle with % monomer grafted for beam time 10 sec and 100 sec.

Grafted PTFE(150μm) (Ar+ Treated)	Degree of grafting(%) at various Temperature		9.77 (50^0C)	8.39 (60^0C)	5.3 (70^0C)
Contact Angle(θ)	Pristine	90.4^o	–	–	–
	Grafted	–	95.5^o	93.3^o	93^0
	Grafted + Irradiated Beam Time=10 Sec	92.3^0	104.4^0	98^0	90.2^0
	Grafted + Irradiated Beam Time = 100Sec	90.9^0	103.2^0	96^0	90.4°

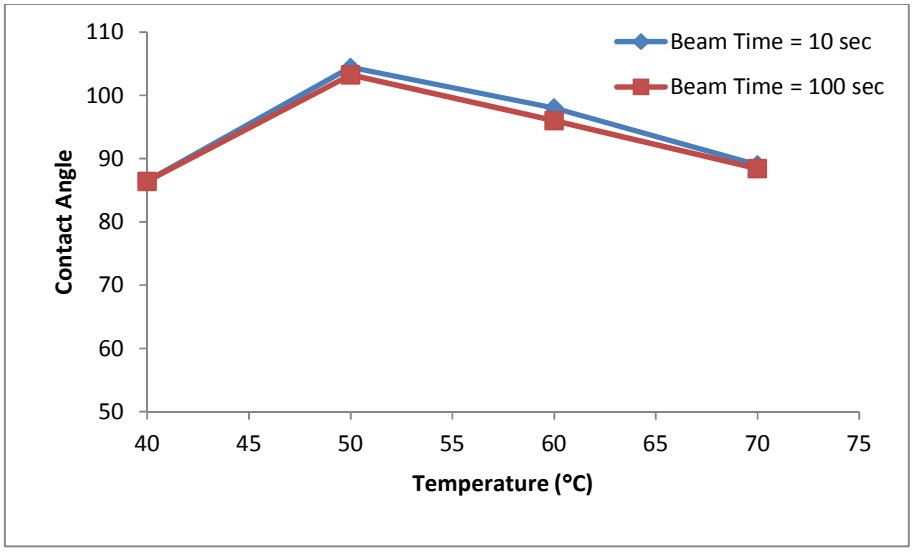

Fig. 7.7 : Variation of contact angle with grafted temperature of PTFE with beam time of 10 sec and 100 sec.

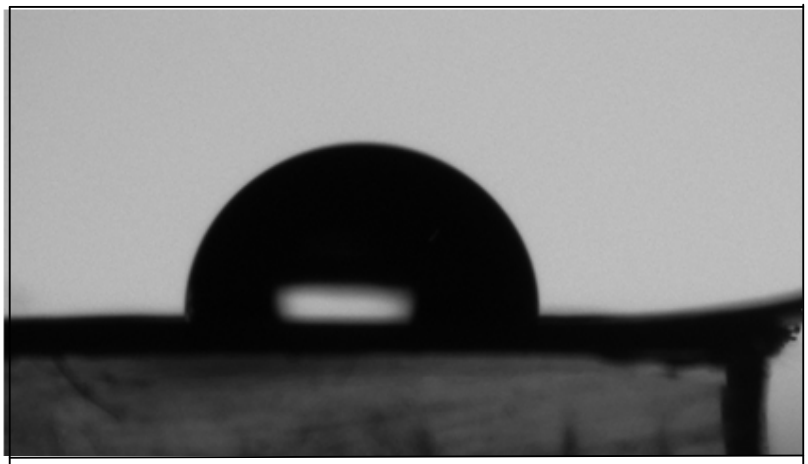

PTFE(Teflon) 150µm
[Grafted -NA ; Beam Time-NA] [Pristine]
Contact Angle [Measured] = 90.4°

6 –Fold Zoom Camera Resolution = ±1°
Model : Easy Drop Standard from KRUSS, Germany
Drop Shape Analysis Software DSA-1

Fig. 7.8 (a) : DSA-1 Output of Pristine PTFE

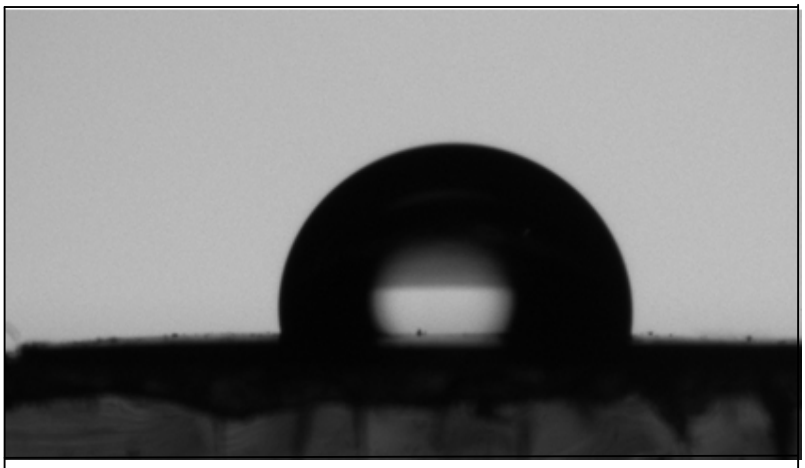

PTFE(Teflon) 150µm
[Grafted At 50°C ; Beam Time-10 Sec]
Contact Angle [Measured] = 104.4°

6 –Fold Zoom Camera Resolution = ±1°
Model : Easy Drop Standard from KRUSS, Germany
Drop Shape Analysis Software DSA-1

Fig. 7.8 (b) : DSA-1 Output of treated PTFE (10 sec) with grafting temperature 50°C (Contact Angle = 104.4°)

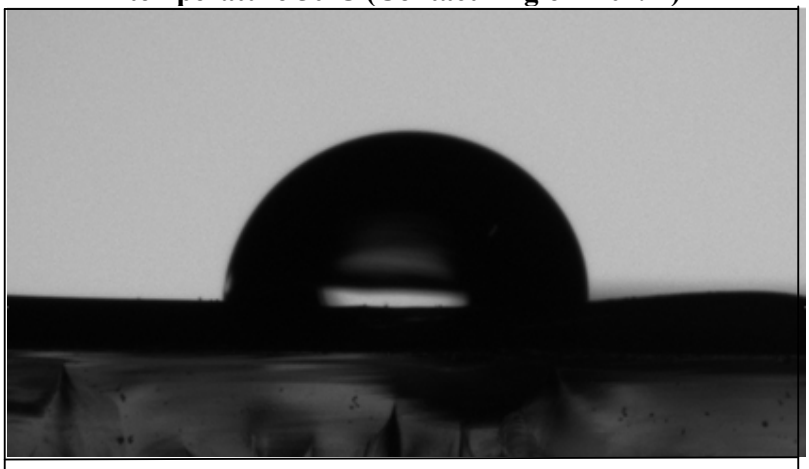

PTFE(Teflon) 150µm
[Grafted At 60°C ; Beam Time-10Sec]
Contact Angle [Measured] = 98°

6 –Fold Zoom Camera Resolution = ±1°
Model : Easy Drop Standard from KRUSS, Germany
Drop Shape Analysis Software DSA-1

Fig. 7.8 (c) : DSA-1 Output of treated PTFE (10 sec) with grafting temperature 60°C (Contact Angle = 98°)

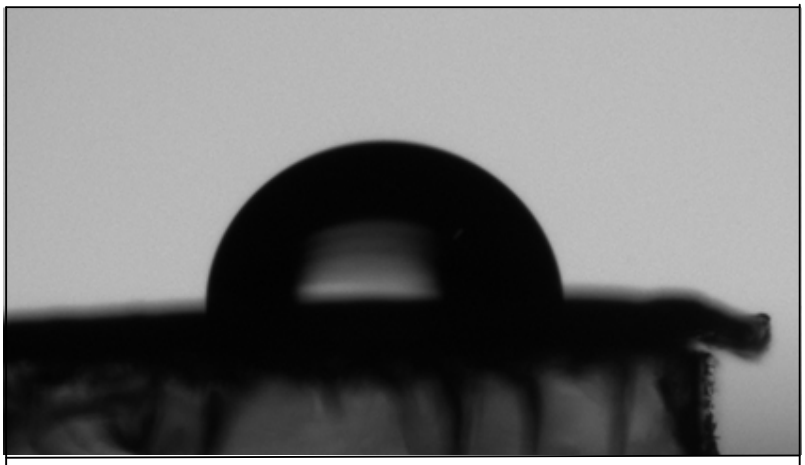

PTFE(Teflon) 150µm
[Grafted At 70°C ; Beam Time-10 Sec]
Contact Angle [Measured] = 89°

6 –Fold Zoom Camera Resolution = ±1°
Model : Easy Drop Standard from KRUSS, Germany
Drop Shape Analysis Software DSA-1

Fig. 7.8 (d) : DSA-1 Output of treated PTFE (10 sec) with grafting temperature 70°C (Contact Angle = 89°)

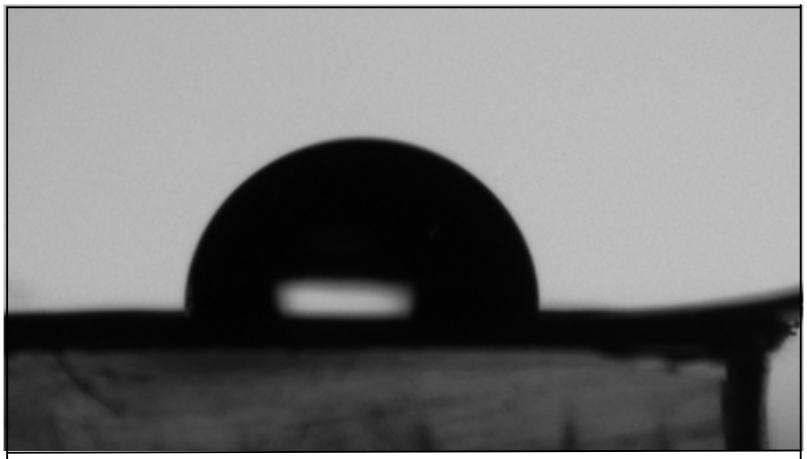

PTFE(Teflon) 150µm
[Grafted -NA ; Beam Time-NA] [Pristine]
Contact Angle [Measured] = 90.4°

6 –Fold Zoom Camera Resolution = ±1°
Model : Easy Drop Standard from KRUSS, Germany
Drop Shape Analysis Software DSA-1

Fig. 7.9 (a) : DSA-1 Output of Pristine PTFE

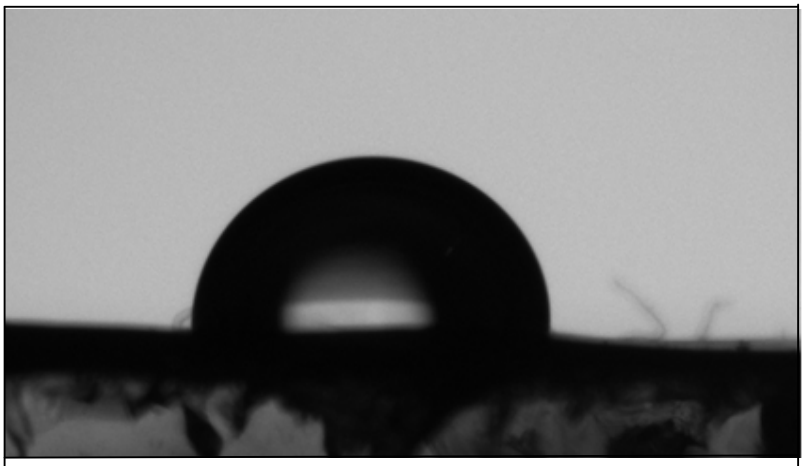

PTFE(Teflon) 150µm
[Grafted At 50°C ; Beam Time-100 Sec]
Contact Angle [Measured] = 103.2°

6 –Fold Zoom Camera Resolution = ±1°
Model : Easy Drop Standard from KRUSS, Germany
Drop Shape Analysis Software DSA-1

Fig. 7.9 (b) : DSA-1 Output of treated PTFE (100 sec) with grafting temperature 50°C (Contact Angle = 103.2°)

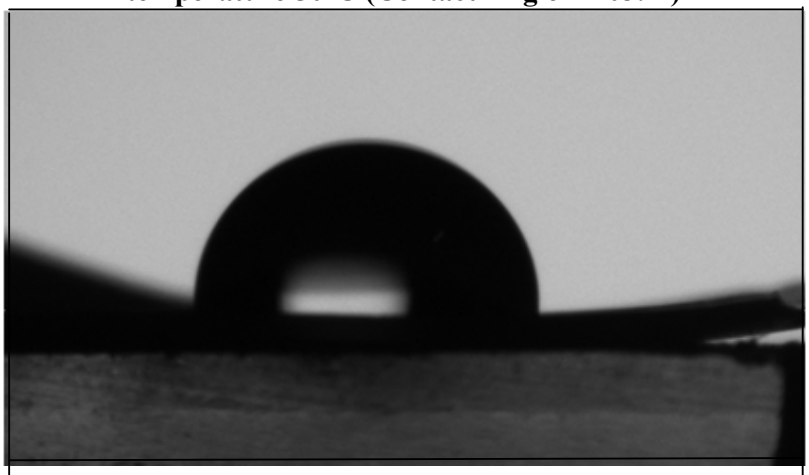

PTFE(Teflon) 150µm
[Grafted At 60°C ; Beam Time-100 Sec]
Contact Angle [Measured] = 96°

6 –Fold Zoom Camera Resolution = ±1°
Model : Easy Drop Standard from KRUSS, Germany
Drop Shape Analysis Software DSA-1

Fig. 7.9 (c) : DSA-1 Output of treated PTFE (100 sec) with grafting temperature 60°C (Contact Angle = 96°)

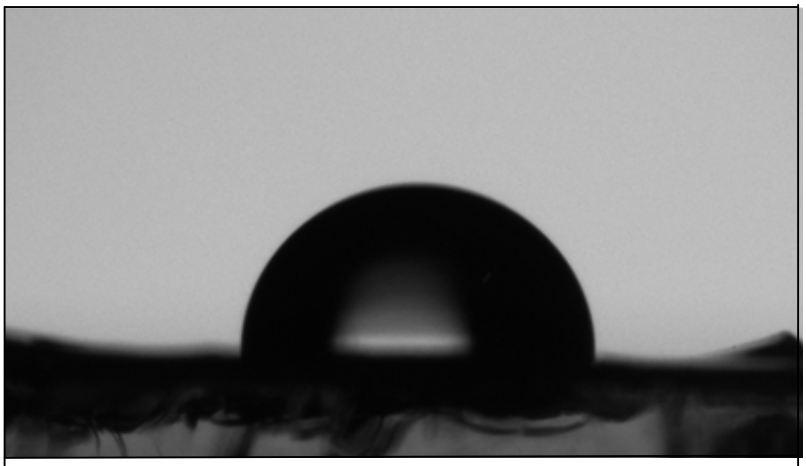

Fig. 7.9 (d) : DSA-1 Output of treated PTFE (100 sec) with grafting temperature 70^{o}C (Contact Angle = 88.4°)

7.5 VARIATION OF CONTACT ANGLE (θ) WITH ROUGHNESS FACTOR (r)

The Wenzel model (Robert N. Wenzel 1936) describes the homogeneous wetting regime and is defined by the following equation for the contact angle on a rough surface

where is the apparent contact angle which corresponds to the stable equilibrium state (i.e. minimum free energy state for the system). The roughness ratio is defined as the ratio of true area of the solid surface to the apparent area.

—

Where A_T = Total Surface Area, A_P= Projected Surface Area

The roughness ratio, r, is a measure of how surface roughness affects a homogeneous surface.

From Eqn. (7.1)

$$r = \frac{\cos\theta_w}{\cos\theta} \qquad \text{Eqn. (7.3)}$$

Since, the total surface area, $A_{T,}$ is always greater than or equal to projected surface area, $A_{P,}$ hence

$$r \geq 1 \qquad \text{Eqn. (7.4)}$$

By using Eqn.(7.3),we calculate the roughness factor 'r'

The mean value of contact angle of lubricant oil Methyl Iodide (CH_3I) on pristine is given in Table 7.2. The value of contact angle on grafted PTFE at various temperature is given in Table 7.3. The roughness factor after grafting is shown in Table 7.4.

Table 7.2 : Contact angle of Pristine Sample

S. No.	**i**	**Ii**	**iii**	**iv**	**Mean**
Contact Angle	90.14^0	91.13^0	89.4^0	90.93^0	90.4^0

Table 7.3 : Contact Angle of Grafted PTFE Polymer at various temperature

Temprature (°C)	**40°C**	**50°C**	**60°C**	**70°C**
Grafting (%)	3.75	9.77	8.39	5.3
Contact Angle (θ)	92.0	95.55	93.3	93

Table 7.4 : Determination of Roughness Factor After Grafting

Grafting Temprature (°C)	**40°C**	**50°C**	**60°C**	**70°C**
Contact Angle (Degree)	92.0	95.5	93.3	93
Roughness Factor (r)	7	13.73	8.29	7.49

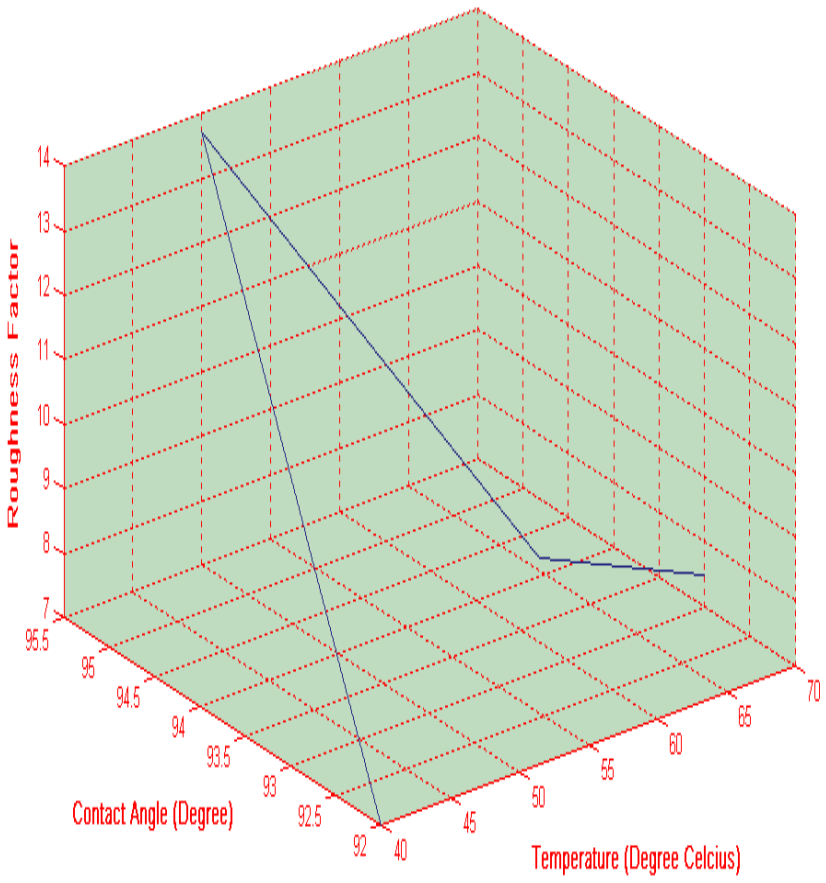

Fig 7.10 (a) Variation of Roughness Factor (r) with contact angle (θ) at various grafting temperature.

The variation of roughness factor (r) with contact angle (θ) at various grafting temperature is shown in Fig. 7.10(a). The maximum roughness factor 13.73 is existing with contact angle of 95.5° at grafting temperature of 50°C.

The value of roughness factor after ion beam treatment with beam time of 10 Sec. and 100 Sec. is given in Table 7.5. The variation of 'r' with contact angle at various grafting temperature is shown in Fig. 7.10 (b) and Fig. 7.10(c)

Table 7.5 : Contact Angle and Roughness Factor of treated PTFE (Irradiated PTFE) (After Grafting)

Grafting Temperature		**40°C**	**50°C**	**60°C**	**70°C**
Contact angle (After Grafting + Irradiation)	10 Sec	92.6	104.4	98	90.2
	100 Sec	92.4	103.2	96	90.4
Roughness Factor (r)	10 Sec	3.99	35.62	19.93	1.2
	100 Sec	1.5	32.71	15.2	1.3

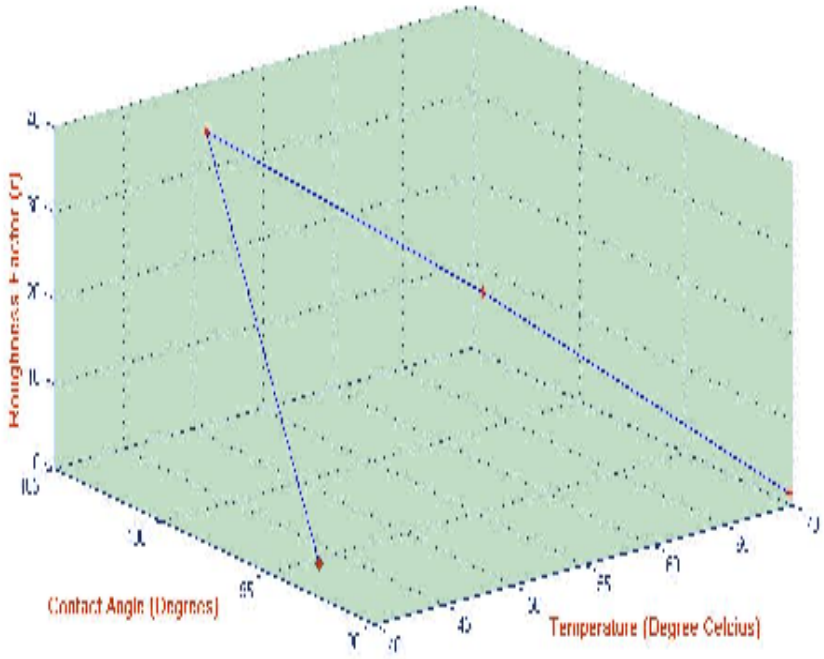

Fig 7.10 (b) : Variation of Roughness Factor (r) with contact angle (θ) at various grafting temperature after ion beam treatment with beam time 10 Sec

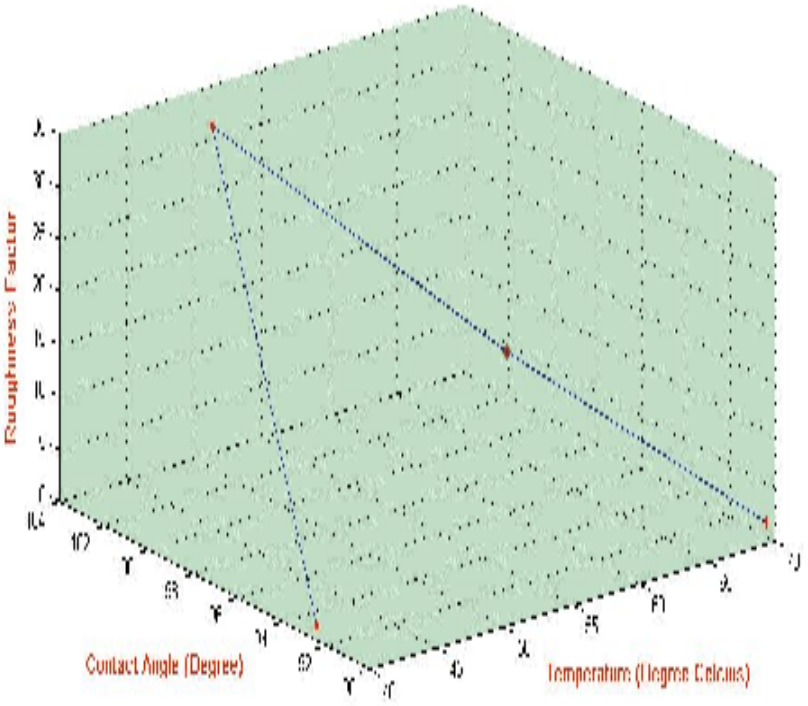

Fig 7.10 (c) : Variation of Roughness Factor (r) with contact angle (θ) at various grafting temperature after ion beam treatment with beam time 100 Sec

7.6 CRYSTALLOGRAPHIC ANALYSIS OF IRRADIATED TEFLON THROUGH XRD

XRD was direct evidence for the periodic atomic structure of the polymers and is the most powerful tool for determining the structure and orientation of polymers. XRD is a non-destructive technique and is based on Bragg's Law. Bruker D8 Advanced Diffractometer uses Nal scintillation counter as a detector at Institute Instrumentation Center (Indian Institute of Technology, Roorkee) is used for the materialic characterization of PTFE polymer surface. Fig. 7.10 (a, b) represents the output of XRD for pure pristine and PTFE grafted at 50^{o}C and 60^{o}C with irradiated ion beam time of 10 sec. The peak is existing at approx. 21^{o} indicating that crystallographic planes of PTFE with grafting temperature 50^{o}C shows maximum orientation at this glancing angle.

The height of the peak in Fig. 7.11 (a) is maximum in comparison to the height of the peak in Fig. 7.11 (b) and 7.12 (a) indicates that the crystallographic behavior of PTFE grafted at 50^{o}C is maximum in comparison to PTFE sample grafted at 60^{o} and 70^{o}C.With the help of comparative analysis Fig. 7.12 (b) in context of their peaks with the pristine, we reached to a conclusion that the crystallographical changes in PTFE sample grafted at 50^{o}C with 10 sec beam time is maximum.

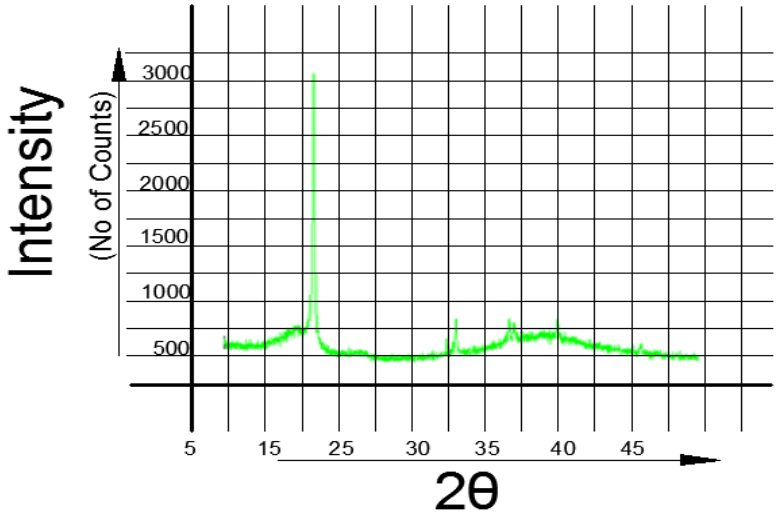

Fig. 7.11(a) : XRD Image PTFE (Teflon) ; Irradiated for 10 sec grafted at 50° C

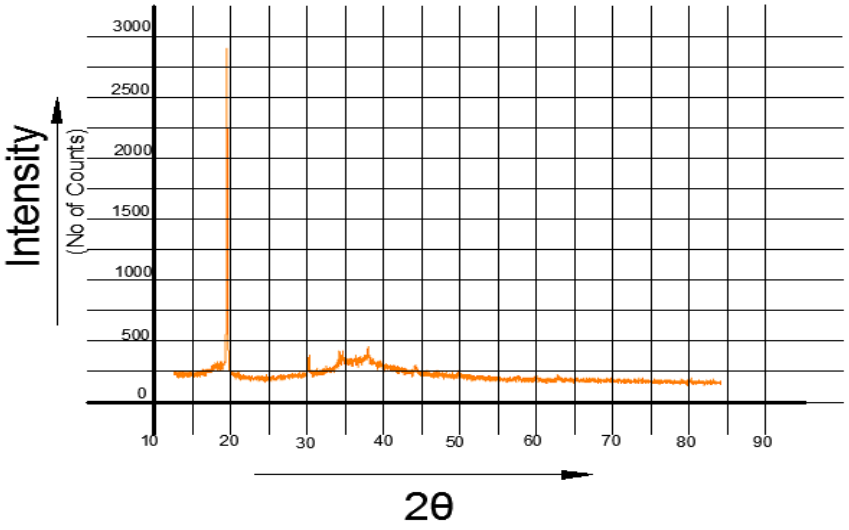

Fig. 7.11(b) : XRD Image PTFE (Teflon) ; Irradiated for 10 sec grafted at 60°C

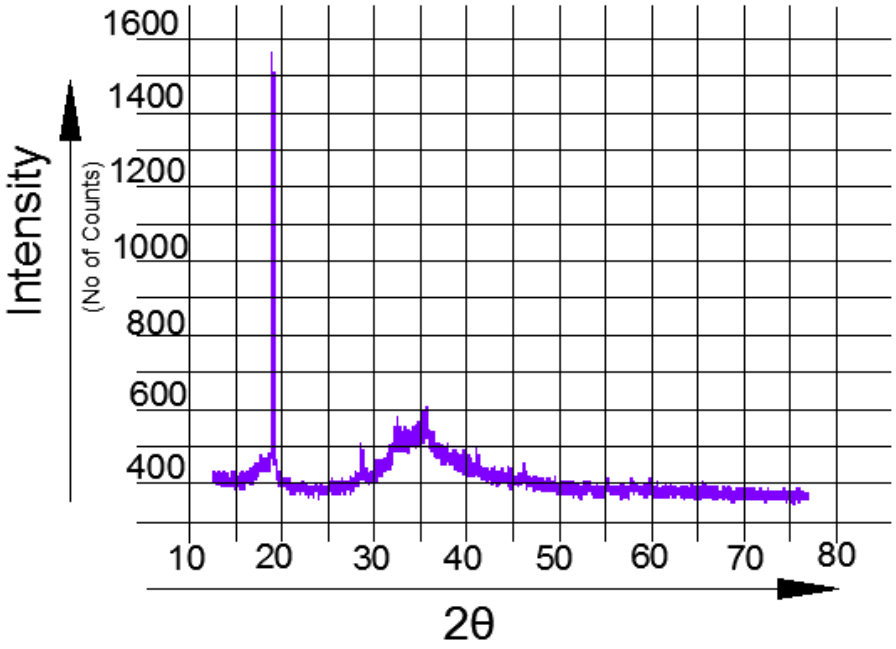

Fig. 7.12(a) : XRD Image PTFE (Teflon) ; Irradiated for 10 sec grafted at 70°C

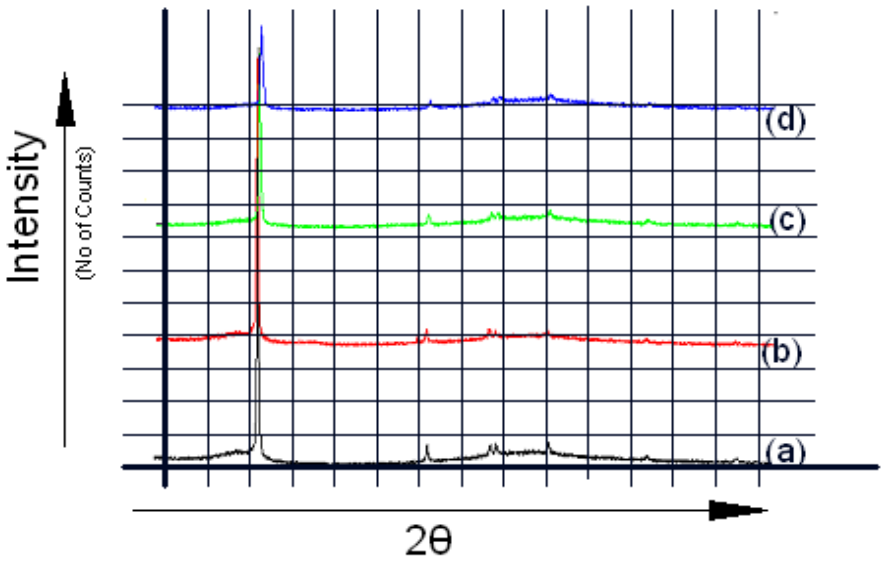

Fig. 7.12(b) : Comparative analysis of XRD images of pristine with treated PTFE grafted at 50°C, 60°C and 70°C temperature

Chapter 8

CONCLUSION AND RECOMMENDATION

8.1 RESEARCH SUMMARY

The two step experimental work was performed to change the surface morphology of PTFE polymeric surface. Firstly, we increase the surface roughness to reduce the wettability of oil on solid surface via chemical grafting process under robust condition. Second step was to enhance the surface roughness of the grafted polymeric surface through low energy Ar^+ ion beam with interaction time of 10 and 100 sec.

We did grafting of MMA on PTFE surface at different temperature, reaction time, monomer concentration and initiator concentration. The maximum yield was achieved at 50^oC whose value is 9.47%. Monomer concentration of 10% V/V and BPO concentration of 0.03 M with reaction time of 2 hrs gives the optimum condition.

The increase in degree of grafting at optimum condition is due to increase in decomposition of initiator leading to the formation of more free radicals and generation of the active cites on the polymeric backbone resulting maximum grafting of MMA on polymeric backbone, effect of grafting was studied by surface morphology through FE-SEM, EDS, CAG and XRD analysis.

To further increase in roughness grafted polymer was irradiated using 3KeV Ar^+ ions and defocused ion beam for beam time of 10 and 100 sec. respectively and again the effect of this treatment is analsis by surface morphology through FE-SEM, EDS, CAG and XRD analysis.

8.2 CONCLUSION DRAWN AFTER GRAFTING

FE-SEM images (Fig. 8.1) of grafted PTFE at 50°C depicted that uniformity in the image was maximum reduced with deep dugs in the form of dark black spots which was responsible for high roughness resulting increase in contact angle observed by goniometer. The value of contact angle at maximum grafting with Methyl Iodide CH_3I liquid on PTFE surface under robust condition was observed through contact angle goniometer and it is 95.5° (Fig. 8.2). The highest peak hence maximum number of counts in XRD analysis of grafted sample was also observed at 50°C , which conclude that maximum change in crystallographic structure of sample.

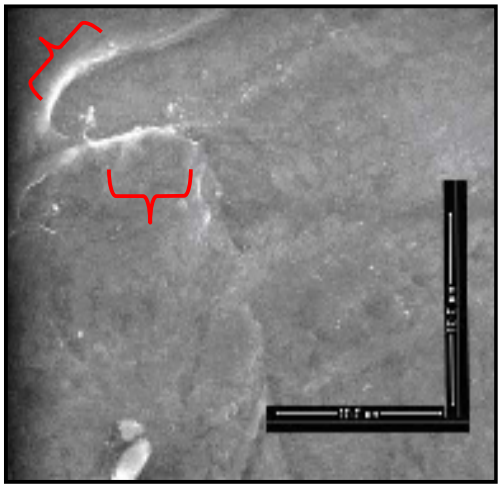

Fig. 8.1 FE SEM Image of Grafted PTFE at 50°C

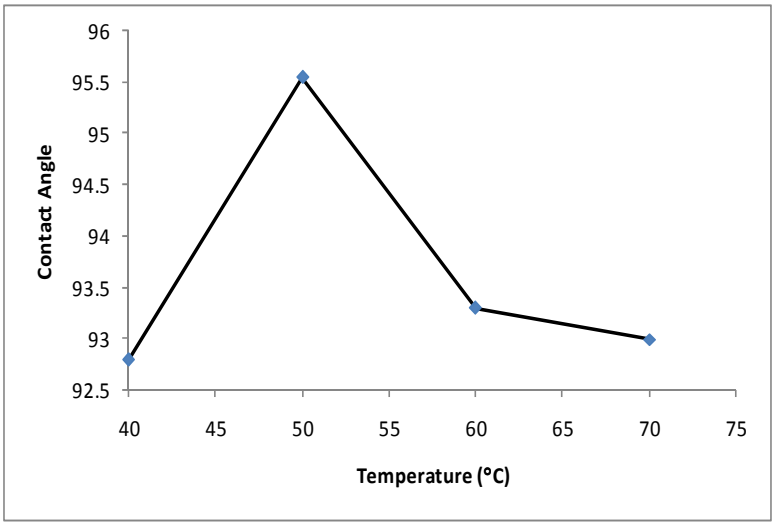

Fig. 8.2 Contact Angle with Grafting Temperature

8.3 CONCLUSION AFTER TREATMENT

FE-SEM image of treated PTFE surface (after grafting) revealed that maximum change in surface morphology in context of change in surface roughness was achieved on 50^{o}C grafted PTFE with 3Mev Ar+ ion beam treatment for 10 sec (Fig.8.3). The maximum bumps and white patches appeared in PTFE surfaces is maximum at 50^{o}C sample. Irregularity and non-uniformity without cracking is the evidence of maximum roughness on grafted PTFE after irradiation

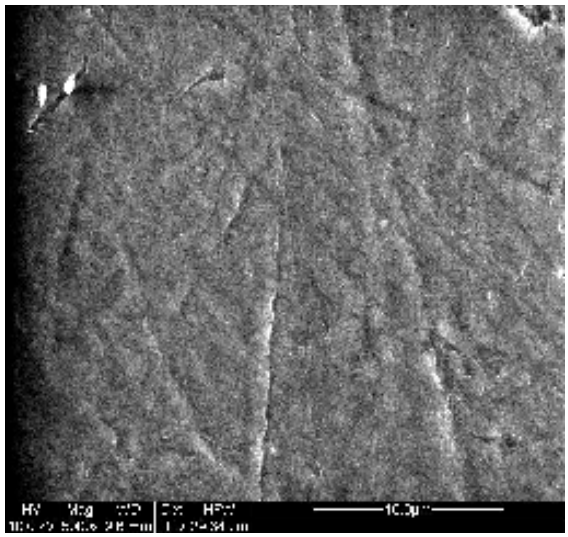

Fig. 8.3 FE SEM Image of irradiated PTFE (After grafting at temperature 50^{o}C)

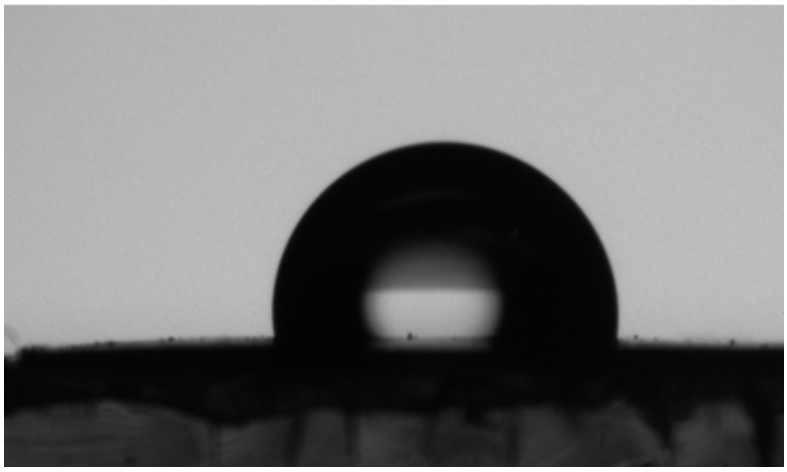

Fig. 8.4 DSA-1 Output of treated PTFE (10 sec) with grafting temperature 50^{o}C (Contact Angle = 104.4^{o})

The contact angle goniometry also revealed that maximum contact angle of 104.4^{o} was achieved on PTFE surfaces which was grafted at 50^{o}C (Fig. 8.4).

The roughness factor (r) is also calculated using this value of contact angle The maximum r value of roughness factor is 34.4 Similarly, the XRD analysis output is also in full compliance with the results i.e maximum number of counts was observed for treated PTFE with grafting temperature of 50^{o}C.

Monomer grafted PTFE sample showed slight increase in contact angle. However, after irradiation further increase of 8-10^{o} was observed. This definite change in contact angle corroborated well with increase in the surface roughness as seen in FE-SEM images.

8.4 RECOMMENDATIONS

In our research, oleophobic polymeric surfaces have been developed by chemical grafting followed by low ion beam radiation and the surface roughness of the film have been improved. Ofcourse, there are many challenges ahead of oleophobic characteristics of the surfaces of various engineering applications.

With commercial applicability of this result generates effective solutions of many engineering and industrial problems like for example its coating in pipeline for crude transportation may be responsible for reduction in wax deposition . To remove adhesion and stiction is still a challenging problem for various engineering applications.

References

1. Drumond C. J., Vasic Z. R., Geddes N., Jurich M. C., Chatelier R.C., Gengenbach T.R., Griesser H.J., (1997), *Colloids Surf., : Physicochem. Eng. Aspects*, **117**, 129.
2. Carlsson C.M.G., Strom G., (1991), *Langmuir*, **7**, 2492.
3. Denes F., Hua Z.Q., Barrios E., Young R.A., Evans J., (1995), *J. Macromol. Sci., Pure Appl. Chem.*, **32**, 1405.
4. Sahin H.T., Manolache S., Young R.A., Denes F., (2002), *Cellulose*, **9**, 171.
5. Chien-Te Hsieh,Yu-Shun Cheng,Shu-Min Hsu,Jia-Yi Lin, (2010), *Applied Surface Science,* **256**, 4867-4872.
6. Lee, H.J.. Owens, J.R.M (2010), *J Mater Sci.,* **45**, 3247-3253.
7. Lee, H.J.. Owens, J.R.M (2011), *J Mater Sci.,* **46**, 4669-76
8. Chien-Te Hsieh, Bi-Sheng Chang, Jia-Yi Lin, (2011), *Applied Surface Science,* **257**, 4867-4872.
9. Prabhu, K.N., Fernades P., Kumar, G., (2009), *Material and Design,* **30**, 297-305.
10. MRS Bulletin, (2008), *Materials Research Society*, **33** (08), 752-758.
11. Hoefnagels, H. F., Wu, D., de With, G. and Ming, W. (2007), *Langmuir*, ***23*** (26), pp 13158–13163.
12. **Bigelow, W.C. Pickett, D.L., Zisman, W.A. (1946),** *Naval Research Laboratory*, Washington, D.C., USA.
13. Jung, Y.C. and Bhushan, B. (2009), *Langmuir*, ***25*** (24), 14165–14173
14. Liu, Y., Xiu, Y., Hess, D.W. and Wong, C.P. (2010), *Langmuir*, ***26***(11). 8908–8913.
15. Segal, L., Philips, F.J., Loeb, F.J., Clayton , R.L., Jr. (1958), *Textile Research Journal,* **28** (3), **233-241.**

16. Torchinsky, I. Rosenman, Æ G., (2009), *NanoscaleResLett,* **4**,1209-1217.

17. Cao L. and Gao D., (2010), *Faraday Discuss*, **146**, 57-65

18. Lee, H.J., Owens, J.R. (2010), *Journal of Materials Science,* **46**, 69-76.

19. Ohkubo, Y., Tsuji, I., Onishi, S., Ogawa, K. (2010), *Journal of Materials Science,* **45**(18), 4963-4969.

20. Bhushan B., (2003), *J. Vac. Sci. Technol.*, **1321**, 2262-96.

21. Bhushan B. and Jung. Y.C., (2007), *Ultramicroscopy*, 107, 1033-41.

22. Wenzel R.N., (1936), *Ind. Eng. Chem.,* **53**, 1466-70.

23. Cassie A.B.D., Baxter S., (1944), *Tarns. Faraday Soc.,* **40**, 546.

24. Israelachvili J.N., (1992), 2nd edn. (London : Academic).

25. Johnson R.E., Dettre R.H., (1964), *Advancements in Chemistry Series,,* **43,** 12-135.

26. Bardley, R.S. (1932). *Philos. Mag.,* **13**, 853.

27. Bailey, A.I., (1961), *J. Appl. Phys.,* **32**, 1407.

28. McFarlane J.S., Tabor D., (1950), *Proc. R. Soc. London, Ser. A,* **202**, 224.

29. Extrand C.W., (2002), *Langmuir,* 18, 1991-9.

30. Nosonovsky M., Bhushan B., (2006), *Microsyst. Technol.,* 12, 231-7.

31. Israelachvili J.N., (1989), *Langmuir,* 5, 288-9.

32. Nosonovsky M., Bhushan B. (2009), *Phil. Trans. R. Soc.,* **367**, 1511-1539.

33. Liu M., Wang S., Wei Z., Song Y., Jiang L., (2009), *Adv. Mater.,* **21**, 665-669.

34. Genzer, J., Efirnenko, K., (2006), *Biofouling,* **22**, 339-360.

35. Koch, K., Bhushan, B, BMW, W., (2009a), *Prog. Mater. Sci*., **54,** 137-178.

36. Xie, Q., Xu, J., Feng, L., Jiang, L., Tang, W., Luo, X., Han, C. C., (2004), Adv. Mater., 302-305

37. Nicolas M., Guittard, F., Geribaldi, S., (2006), *Angew.* Chem. Int. *Ed.* **45**, 2251-2254

38. Geil P.H., (1963), Polymer Single crystals (Inter Science, New York).

39. Keller A., (1968), Report. Prog. Phys., **31**, 623.

40. Winderlich B., (1973), "Macromolecular Physics", Vol. 1 Crystal structure, Morophology, Defect and Vol. 2 Crystal Nucleation, Growth, Annealing" (Academic Press, New York).

41. Grubb D.T., (1976), *J. Microsc. Spectrosc., Electron,* 671.

42. Grubb D.T., (1982), In "Development in crystalline Polymer-1 (Applied science, London), p.1.

43. Uhlmann D.R., Kolbeck A.G., (1975), *Sci. Am.,* 233, 96.

44. Bassett D.C., (1981), Principles of Polymer morphology (Cambridge University Press, Cambridge)

45. Bassett D.C., (1984), *CRC Crit. Rev Solid State Matter. Sci* ,**12**(2), 97.

46. Flory P.J., (1953), "Principle of Polymer Chemistry" (Cornel University Press).

47. Lebedev S.V., Shikavronskaly N.A., (1911), *J. Russ. Phys. Chem. Soc.,* **43**, 1124.

48. Lebedev S.V., (1915), *Chem Abs.,* **9**, 798.

49. Staudinger H., (1929), *Augew Chem*. **42**, 67.

50. Bunn C.W., (1936), *Trans Faraday Soc*., **35**, 428

51. Fisher F.W., (1957), *Z. Naturforsch,* **12**, 753.

52. Keller A., (1957), *Phil. Mag.,* **2,** 1171.

53. Till P.H., (1957) *J. Polymer Science,* **24,** 301

54. Geil P.H., (1963), Polymer Single Crystals (Interscience, N.Y.).

55. Basssett D.C., Godge A.M., Olley R.H., (1980), *Faraday Soc.,* **68,** 10.

56. Keller A., (1962), *Polymer*, **3**, 393.

57. Lindemyer P.H., (1962) , *Science,* **147**,12566.

58. Garbassi F., Morra M., Occhiello E., (1998), "Polymer Surfaces: from Physics to technology", John Wiley& Sons, Chichester.

59. Sun T., Xu P., Liu Q., Xue, J., Xie W., *(200***3),** *Eur. Polym.* J., **3**9, 189-192.

60. Yao Z.P., Randy B., (1990), *J. Appl. Polym. Sc*i., **4**1, 1459-1467.

61. Somanathan N., Balasubramaniam B., Subramaniam V., *Macromo J.,* (1995), *Sci. Pure Appl. Che*m., **32(5),** 1025-1036.

62. Sanli O., Aytemiz S., Unal H.L., *Macromol J.,* (1997), *Sci. Pure Appl. Che*m., **34A (6),** 1003.

63. Inagaki N., Tasaka S., Masumoto M., (1996), *Macromolecules, **29***, 164.

64. Ion Solid Interaction : Status and Perspectives (2005), *Brazilian Journal of Physics*, **35**(3),

65. Farhataziz A., Rodgers M.A.J., (1987), Radiation Chemistry : Principles & Applications, VCH Publishers Inc., NewYork, , pp-1.

66. Chmielewski A.G., Haji-Saeid M. and Ahmed S., (2005), *Nucl. Instr. And Meth.*, **236**, 44.

67. Nastasi, M., Mayer J.W. and Hirvonen J.K. (1996), Ion solid interactions, Cambridge University Press.

68. Eckstein W., (1991), Computer Simulation of Ion-solid interactions, Springer Verlag, p. 63

69. Ryssel, H. and Ruge I., (1986), Ion implantation, Wiely-Interscience, New York.

70. Biersack J.P., and Haggmark L.G. (1980), *Nucl. Instr. and Meth.,* **174**, 257.

71. Fink D., (2004), "Fundamentals of Ion-Irradiated Polymers", Springer, Berlin.

72. Chapman, B., (1980). "Glow Discharge Processes: Sputtering and Plasma Etching", John Willey & Sons, New York.

73. Behrisch R., Wittmaack K., (1991), ”Sputtering by Particle Bombardment III”, Springer-Verlag, Berlin.

74. Sigmund P., (1981), In: ”Sputtering by Particle Bombardment I”, R. Behrisch (ed.), Springer-Verlag, Berlin, p. 9.

75. Jackson J.D., (1975), ”Classic Electrodynamics”, 2nd Edition, John Wiley, New York, 492.

76. Chatterjee A. and Schafer J.J., (1973), *Radiat. Environ. Biophys*.13, 479.

77. Magee, J.L. and Chatterjee, A., (1987). Chapter1, 5and 6 “Radiation Chemistry, Principles and Application” Farhataziz and MA Rodgers, eds. VCH publisher, New York.

78. Butts, J.J. and Katz R., (1967), *Radiation Research*, **30**, 855.

79. Waligorski M.P.R., Hamm R.N. and Katz R.N., (1986), *Nucl.Tracks Radiat. Meas*., 11, 309.

80. Lee E.H., (1999), “Invited talk” Delivered in the 3rd International Conference on ionizing radiation and polymer (irap-98), Held at Dresden, Germany(19-24Sep., 98), *Nucl. Instr. And Meth.B.*

81. Magee J.L. and Chatterjee A., (1980), *J Phys.Chem.*, **84**, 3529.

82. Magee J.L. and Chatterjee A., (1987), Chapter 4 in non-homogeneous process “G R Freeman willy & Sons, New York.

83. Nosonovsky M., Bhushan, B., (2008), *J. Phys. Condens Matter* 20, 225009(30pp.)

84. Khudhayer W.J., Sharma R., Karabacak T., (2009), *Nanotechnology* **20**(27), 2 275302(9pp.).

85. Tretinnikov O.N., (2000), Wettability and Microstructure of Polymer Surfaces, Stereochemical and conformational aspects Apparent and Microscopic Contact Angle, ed J Drelich, JS Laskowski and K L Mittal (Utrecht:VSP) pp 111-28

86. Alvarez, A., Amirfazli, A.W., Neumann, J.M. (1999), *A Physicochemical and Engineering Aspects*, **156** (1-3), 15, 163-176.

87. Aurélien F., Stalder, Tobias Melchior, Michael Müller, Daniel Sage, Thierry Blu, Michael Unser, (2010), *A Physicochemical and Engineering Aspects*, **364** (1-3), 72-81.

88. Kwok D.Y., Neumann A.W., (1999), *Advances in Colloid and Interface Science*, **81**(3), 167-249.

89. Palmer, E.W., (1988), *Original Research Article Precision Engineering*, **10** (3), 147-152.

90. Zebin Wang, Ganesan Narsimhan, Dennis Kim, (2008), *Original Research Article LWT - Food Science and Technology*, **41** (7), 1232-1238.

91. Kwok, D.Y., Neumann, A.W., (2000), *Physicochemical and Engineering Aspects*, **161** (1), 49-62.

92. Cullity B.D., (1978), Elements of X-ray Diffraction, Seconded, Addisonesley, London, 102.

93. Reynier Y., Yazami R., Fultz B., (2007), *Journal of Power Sources*, **165** (2), 616-619.

94. Oueslati, H., Rhaiem B., Ben A., Amara, H. (2011), *Original Research Article Desalination*, **271**(1-3), 139-149.

95. Schmidt, W. (2009), *Original Research Article*. *Microporous and Mesoporous Materials*, **117** (1-2), 372-379.

96. Geoffrey D., Jindrich Volc, Marja-Leena, Niku-Paavola (2004), *Original Research Article Comptes Rendus Biologies*, **327**(9-10), 861-871.

97. Oguz A., Temelli, F. (2011), *Original Research Article Desalination*, **278** (1-3), 387-396

98. Toshihiko O. (2009), *Biochemical and Biophysical Research Communications*, **380** (2), 254-259.

99. Ares J.R., Pascual A., Ferrer I.J., Sánchez C. (2004), *Original Research Article Thin Solid Films*, **450** (1), 207-210.

100. Francois-Xavier Le Bourdonnec, Gérard Poupeau, Carlo Lugli (2006), *Original Research Article Comptes Rendus Geoscience*, **338** (16), 1150-1157

101. Kour I., Misra B.N., Barsola R., (1996), *Angew. Makromol. Chem.,* **1,** 234.

102. Chen M ., Xia Q., Hea S., Lib Y., Z., Song L., Dai X ., Yang G., Han B ., Xu *Academy of Science, Polymer* , **43,** 1183-1188.

103. Chen J., Yang L., Wua M ., Xia Q., Hea S., Lib Y., Chang Nho Y., *Chem.* **59,** 313-316.

104. Sun T., Xu P., Liu Q., Xue, J., Xie W., *(200***3),** *Eur. Polym.* J., **3**9, 189-192.

105. Yao Z.P., Randy B., (1990), *J. Appl. Polym. Sc*i., **4**1, 1459-1467.

106. Akin O., Temelli F., (2011), *Original Research Article Desalination*, **278**(1-3), 387-396.

107. Reynier Y., Yazami R., Fultz B., (2007), *Journal of Power Sources*, **165**(2), 616-619.

108. Oueslati, H., Ben Rhaiem, A. Ben Haj Amara, (2011), *Original Research Article Desalination*, **271**(1-3), 139-149.

109. Nosonovsky M., Bhushan B., (2008), *J. Phys. Condens Matter,* **20**.

110. Khudhayer W.J., Sharma R., Karabacak T., (2009), *Nanotechnology,* **20**(27).

111. Li K., Wu P., Han Z., (2002), *Polymer,* **43,** 4079.

112. Johnson R.E., Dettre R.H., (1964), *Am. Chem. Soc. Washington,* **112**.

113. Kobayashi H., Owen M.J., (1990), *Marcomolecules* **23,** 4929.

114. Hong B.S., Han J.H., Kim S.T., Cho Y.J., Park M.S., Dolukhhanyan T., Sung C., (1999), *Thin Solid Films,* **351**, 274.

115. Wenzel R.N., (1936), *Ind. Eng. Chem.,* **28**, 988.

116. Cassie A.B.D., Baxter S., (1944), *Tarns. Faraday Soc.,* **40**, 546.

117. Bartell F.E., Shepard J.W., (1953), *J. Phys. Chem.,* **57**, 211.

118. Dettre R.H., Johnson R.E., (1964), *Am. Chem. Soc. Washington,* **136**.

119. Nakajima A., Fujishuma A., Hashimoto K., Wanabe T., (1999), *Adv. Mater.,* **11**, 220.

120. Onda T., Shibuichi S., Satoh N., Tsujii K., (1966), *Langmuir,* **12**, 2125.

121. Shibuichi S., Onda T., Satoh N., Tsujii K., (1966) *J. Phys. Chem.,* **100**, 19512.

122. Bhushan B. (1999), Handbook of Micro/Nanotribology, second ed. CRC Press, Boca Raton, Florida.